POLITECNICO DI TORINO
&
THE MOLECULAR FOUNDRY
LAWRENCE BERKELEY NATIONAL LABORATORY

PhD IN MATERIALS SCIENCE AND TECHNOLOGY

Sponsored by aBeam Technologies Inc. and the Molecular Foundry (LBNL)

NANOIMPRINTING OF PLANAR PHOTONIC DEVICES FOR VISIBLE LIGHT APPLICATIONS

PhD Advisors

Dr. Stefano Cabrini
Facility Director, Nanofabrication
The Molecular Foundry (LBNL)
67 Cyclotron Rd, Berkeley, CA, 94720
scabrini.lbl.gov

Dr. Christophe Peroz
Director of Nanofabrication and Optical devices
aBeam Technologies Inc.
22290 Foothill Blvd. Hayward, CA, 94541
cperoz@lbl.gov

Prof. Fabrizio Pirri
Full Professor
Department of Physics, Politecnico di Torino
Corso Duca degli Abruzzi 24, Torino, 10129, Italy
fabrizio.pirri@polito.it

PhD candidate

Giuseppe Calafiore
Nanofabrication Scientist
aBeam Technologies Inc.
gcalafiore@lbl.gov

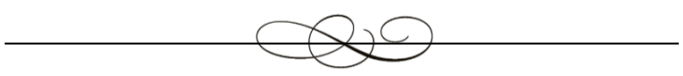

PhD, XXVIII CYCLE
YEAR 2013/2016

Table of Contents

Acknowledgments

"Such a lovely place,
Such a lovely face."
Hotel California, Eagles (1977)

I have spent in Berkeley the past four years of my life. This has been the longest I ever lived abroad, besides the two years in Australia during my master degree studies. Berkeley is the only place after Sicily that I became to call 'home'. I cannot begin to tell how many things have changed in my life during these four years in California. How many things I learned, discovered, understood, enjoyed, and forgot. How many people I met, friends and collaborators who had a strong impact in both my professional and personal life. Most of them have gone back to their lives, almost like if California was a great parenthesis in their twenties and thirties, a dream that momentarily interrupted the regular course of time and that had to fade away after a little while. Looking back at what it has been, everything feels like driving to the Grand Canyon or Yosemite at sunset, usually after work on Friday night, with a song of the Eagles playing in the background and the amazing view of the Californian nature sliding out there. This is how I lived and loved this piece of existence in California and this is how it still feels.

There are really so many people that accompanied me in this journey and there isn't just enough time to list the multitude of reasons that bring me to thank each one of them. Therefore, I will simply acknowledge everyone by listing their names below, except for a very few of them, who deserve a little special gratitude.

The friends, students, collaborators and staff of the Molecular Foundry who made incredibly pleasant and fun the daily work and life outside the lab. In random order, Stefano Dallorto, Melanie West, Jiye Lee, Thomas Darlington, Nicholas Borys, Alexander Weber-Bargioni, Alexander Polyakov, Takuya Uehara, Tonatiuh Rangel Gordillo, Wei Bao, Simone Sassolini, Michael Elowson, Daniel Staaks, Paul Ashby, Deirdre Olynick, Adam Shwazberg, Bruce Hartneck, Erin Wood, Jim Schuck, Frank Ogletree, Weilun Chao, Virginia Altoe, Dominik Ziegler, Maki Nishizaka, Ed Wong, Lauren Otto, Carleton Falzone, Perry Lao, Eric Meshot, Ambika Bumb, Dmitriy Voronov, William Martinez, Nerea Alayo, Irene Fernandez-Cuesta, Benoît Desbiolles, Claudio Shawawreh, Eleonora De Luca, Éric Vire, Quentin Fillot, Angelica Testini, Davide Tierno, Filippo Salvadori, Valeria Rossi, Jacopo Pedrini, Luca Moretti, Raffaele Pugliese, Michela Sainato, Valentino Zegna Baruffa, Lorenzo Maserati, Agathe Machecourt, Karol Miszta, Alessandro Alabastri, Eleonora Bartoli, Stefano Stassi, Margherita Tardivo, Mauro Melli, Francesca Maria Toma, Erika Penzo, Nick Petrone, Antonio Biondi, Cinzia Strano, Annalisa Andaloro, Donata Passarello, Valeria Rustichelli, Lucas Digiannantonio, Giuseppe Cantarella, Anna Bonfante, Maria Chiara Simonelli, Alessia Battigelli, Tomas Marangoni, Valeria Lacatena, Francesco Forleo, Céline Ricci, Berk Celebisoy. A particular thanks goes to my friend and colleague Scott Dhuey for his great work. Many of our technology accomplishments would have been just impossible without his help. I

should also mention all of the collaborators from other institutions and companies who contributed to this work. Frances Allen and Paul Lum from the University of California, Berkeley. Alexander Goltsov and Vladimir Yankov from Nano-optic Devices. Marko Vogler, Arne Schleunitz, Manuel Thesen, Gabi Grützner from micro resist technology GmbH. I am particularly grateful to Prof. Fabrizio Pirri, who designed this collaboration such as to allow me to conduct my research abroad and obtain the PhD at the Polytechnic University of Turin. Many thanks to Sergey Babin, founder and president of aBeam Technologies for wanting me to join the company and having contributed to sponsoring this PhD. He is a successful business man and a wise, honest person that taught me a lot along the way. I cannot begin to tell how thankful I am to my team, the manager Keiko Munechika, Alexander Koshelev and Carlos Piña-Hernandez, who have been reckless gladiators and strongly contributed to the sensational work of this thesis.

Christophe Peroz, advisor, boss and friend, who has mentored me vigorously for so long and helped me build a vision of my future profession and career. He has always been on my side, corrected, promoted and encouraged me to acquire greater awareness and maturity. I value his hateful, lovely French touch.

All my gratitude goes to Stefano Cabrini. His leadership and personality, so friendly, affable, outspoken, sensitive, thoughtful and so Italian generated an ideal environment for research, where everyone could feel part of the same great team. Stefano has been a mentor, a brother and a dad not just for me but for my wife too. His lovely wife Lisa, and wonderful kids Mahela and Antonio have been for us like a family.

Finally, I could not have done all this without my wife Francesca, my parents and grandparents, who stayed on my side all the time and supported all of my efforts. I promise that I will share the results of these fruitful years with you, because you made all this possible.

Partners, affiliations, and sponsors

Contributions to the thesis

The work of this thesis is the result of my and other people's research efforts, who worked in concert to produce the wide spectrum of achievements presented here. Although all of the members' tasks are fundamentally entangled and often overlapping in a multidisciplinary research team like ours, the contributions to this thesis can be simplified as follows.

I developed the imprint process by SR-NIL of all of the integrated DPH devices and full fabrication of the chips (Chapter III). The design and measurements of the DPH devices were performed by NOD, particularly Dr. Alexander Koshelev, Dr. Alexander Goltsov and Dr. Vladimir Yankov. I conducted all of the imaging characterizations on the DPH chips (SEM, AFM, etc...). The development of the sol-gel, high-refractive index material was performed by Dr. Carlos Pina-Hernandez, from our aBeam's team, who also developed the imprint processes that are mentioned in Chapter IV. I designed, simulated and optically characterized all the PhCs (Chapter IV). I also conducted the thorough statistical characterization on the fabrication results in both SR-NIL of DPHs and R-NIL of PhCs. The ongoing research on the active sol-gel material is being carried mainly by Dr. Pina-Hernandez, while the imprint of 3D near-field probes on the facet of an optical fiber is part of Dr. Koshelev's and my current research.

Papers published during the PhD

1. G. Calafiore, A. Koshelev, S. Dhuey, A. Goltsov, P. Sasorov, S. Babin, V. Yankov, S. Cabrini, and C. Peroz, "Holographic planar lightwave circuit for on-chip spectroscopy," *Light: Science & Applications,* vol. 3, p. e203, 2014.

2. G. Calafiore, S. Dhuey, S. Sassolini, N. Alayo, D. Gosselin, M. Vogler, D. Olynick, C. Peroz, and S. Cabrini, "Multilayer lift-off process for sub-15-nm patterning by step-and-repeat ultraviolet nanoimprint lithography," *Journal of Micro/ Nanolithography, MEMS, and MOEMS,* vol. 13, pp. 033013-033013, 2014.

3. G. Calafiore, A. Koshelev, S. Dhuey, S. Sassolini, M. Messerschmidt, A. Schleunitz, A. Goltsov, C. Piña-Hernandez, F. C. Pirri, V. Yankov, S. Cabrini, and C. Peroz, "Step-and-repeat nanoimprint on pre-spin coated film for the fabrication of integrated optical devices," *Journal of Micro/Nanolithography, MEMS, and MOEMS,* vol. 14, pp. 033506-033506, 2015.

4. G. Calafiore, Q. Fillot, S. Dhuey, S. Sassolini, F. Salvadori, C. A. Mejia, K. Munechika, C. Peroz, S. Cabrini, and C. Piña-Hernandez, "Printable photonic crystals with high refractive index for applications in visible light," *Nanotechnology,* vol. 27, p. 115303, 2016.

5. A. Koshelev, G. Calafiore, C. Peroz, S. Dhuey, S. Cabrini, P. Sasorov, A. Goltsov, and V. Yankov, "Combination of a spectrometer-on-chip and an array of Young's interferometers for laser spectrum monitoring," *Optics letters,* vol. 39, pp. 5645-5648, 2014.

6. S. Babin, G. Calafiore, C. Peroz, R. Conley, N. Bouet, S. Cabrini, E. Chan, I. Lacey, W. R. McKinney, and V. V. Yashchuk, "1.5 nm fabrication of test patterns for characterization of metrological systems," *Journal of Vacuum Science & Technology B,* vol. 33, p. 06FL01, 2015.

7. C. Pina-Hernandez, V. Lacatena, G. Calafiore, S. Dhuey, K. Kravtsov, A. Goltsov, D. Olynick, V. Yankov, S. Cabrini, and C. Peroz, "A route for fabricating printable photonic devices with sub-10 nm resolution," *Nanotechnology,* vol. 24, p. 065301, 2013.

8. S. Dhuey, C. Peroz, D. Olynick, G. Calafiore, and S. Cabrini, "Obtaining nanoimprint template gratings with 10 nm half-pitch by atomic layer deposition enabled spacer double patterning", Nanotechnology, vol. 24, pp. 105303-105303, 2013.

9. C. Pina-Hernandez, A. Koshelev, L. Digianantonio, S. Dhuey, A. Polyakov, G. Calafiore, A. Goltsov, V. Yankov, S. Babin, and S. Cabrini, "Printable planar lightwave circuits with a high refractive index," *Nanotechnology,* vol. 25, p. 325302, 2014.

10. V. V. Yashchuk, P. J. Fischer, E. R. Chan, R. Conley, W. R. McKinney, N. A. Artemiev, N. Bouet, S. Cabrini, G. Calafiore, I. Lacey, C. Peroz, and S. Babin, "Binary pseudo-random patterned structures for modulation transfer function calibration and resolution characterization of a full-field transmission soft x-ray microscope," *Review of Scientific Instruments,* vol. 86, p. 123702, 2015.

Papers currently in preparation

1. G. Calafiore & A. Koshelev, T. P. Darlington, N. J. Boris, S. Dhuey, E. Wong, S. Sassolini, S. Babin, A. Weber-Bargioni, P. J. Schuck, K. Munechika, S. Cabrini, "Campanile near-field optical probe fabricated on a fiber by Nanoimprint Lithography", to submit to Nanotechnology.

2. G. Calafiore, É. Vire, A. Alabastri, L. Chen, A. Montazeri, S. Dhuey, S. Sassolini, A. Koshelev, K. Munechika, H.-Y. Holman, S. Cabrini, "Fabrication of a three-dimensional plamonic grid for Infrared Spectroscopy", to submit to Nano Letters.

3. A. Koshelev & G. Calafiore, F. Allen, P. Lum, K. Munechica, S. Cabrini, "Fiber-coupled diffractive optical elements fabricated using nanoimprint lithography", to submit to Nano Letters.

Papers presented in international conferences

1. Oral Presentation: "Variable three-dimensional plasmonic structures fabricated by hyperbaric nanoimprint lithography", Nanoimprint & Nanoprint Technology, Napa, CA, October 2015.

2. Poster presentation: "Near-field Campanile probe fabricated by Nanoimprint Technology", Annual User Meeting, The Molecular Foundry, LBNL, Berkeley CA, 20 August 2015

3. Oral presentation: "Printable Integrated Photonic Devices with a high refractive index", EIPBN, San Diego, May 27, 2015.

4. Invited talk: "Use of Nanoimprint Lithography to fabricate nano-optical devices", NIMSA & OSUM Seminar series, University of Michigan, Ann Arbor, MI, November 2014.

5. Oral presentation: “Step-and-repeat nanoimprinting on pre-spi n coated film: from sub-15nm metal patterning to the fabrication of a spectrometer-on-chip”, EIPBN, Washington DC, May 30, 2014.

6. Poster presentation: “Photonic integrated spectrometer-on-chip based on digital planar holograms” EIPBN, Washington DC, May 28, 2014.

7. Oral presentation: “Step-and-repeat nanoimprinting on pre-spin coated film: from sub-15nm metal patterning to the fabrication of a spectrometer-on-chip”, Alternative Lithographic Technologies, SPIE Advanced Lithography, San Jose, 02/26/14.

8. Oral presentation: “Photonic integrated spectrometer-on-chip based on digital planar holograms”, Photonics West, SPIE OPTO, San Francisco, 02/03/14.

Funding Sources

The work reported in this PhD thesis has been supported by different US funding agencies under different contracts.
Work at the Molecular Foundry supported by the Office of Science, Office of Basic Energy Sciences, of the US Department of Energy under Contract No. DE-AC02-05CH11231.
Work on the holographic on-chip spectrometer (Chapter III) was sponsored by the US Air Force Office of Scientific Research under grant/contract number FA9550-12-C-0077
Work on the development of the hybrid organic-inorganic sol-gel material based on TiO_2 (Chapter IV) was sponsored by the US Air Force Office of Scientific Research under grant/contract number FA9550-12-C-0055.
Work on the printable photonic devices with a high-refractive index material (Chapter IV) was supported by the US Air Force under grant/contract number FA9550-14-C-0020.
Work on the imprint of three dimensional structures onto a fiber for SNOM applications (Conclusion and perspectives) was funded by the US Department of Energy under Contract No. DE-SC0013109

This PhD was sponsored by aBeam Technologies Inc. and the Molecular Foundry (LBNL).

I. Introduction

I.1 Motivation and overview of the thesis

In the 2013, the 68th session of the United Nation (UN) General Assembly proclaimed 2015 as the international year of light and light-based technologies (IYL2015). In doing so, "the UN has recognized the importance of raising global awareness about how light-based technologies promote sustainable development and provide solutions to global challenges in energy, education, agriculture and health".[1] Many aspects of our daily life have been profoundly revolutionized by the 'science of light' and advent of technologies once considered impossible: lasers, ultrafast internet, optical data storage, material processing tools, powerful sensors, diagnostic tools for biomedicine, efficient light generating devices, and many others. The science that is fueling this new revolution goes by the name of photonics, in analogy to electronics, because it deals with the flow, control and manipulation of quanta of light, called photons. Just like any other newborn discipline, over the last five decades photonics went from discovery and fast evolution to the search for technology implementations and actual applications. Emerged as an enabling discipline to support existing technologies, photonics has combined with a variety of other fields – i.e. semiconductor, computing, telecommunication, biology, medicine, etc. As of today, photonics greatly participates to almost all technologies that are shaping the future, such as virtual and augmented reality, quantum computing, and robotics.

The advancements in nanotechnology and nanofabrication techniques are supporting the success of this field. However, while many photonic devices for optical communication in the near infrared have been fabricated for decades, many other photonic applications in the visible range are still constrained to the research field. Higher resolution lithography and very controllable fabrication processes are required as photonic functionalities become more complex and the working range approaches the visible regime. State-of-the-art tools and conspicuous investments on the development of new fabrication processes are required to make future visible light applications a reality. Other than a handful of research facilities and companies, semiconductor plants that potentially would be capable of supporting nanofabrication of such devices are tightly engaged with the manufacturing of integrated circuits. This is one of the reasons why photonics today still suffers from fragmentation and the lack of device standards. The need for different technologies that depend on the field of integration, whether this is electronics or biomedicine, created further differentiation of the fabrication processes. Materials that are used

in the fabrication of photonic devices also change based on the wavelength of light and target application. Most of these materials and processes are not fully compatible with the current manufacturing equipment that are used in the semiconductor industry. Therefore, more suitable technology solutions must be searched elsewhere. We believe that Nanoimprint Lithography (NIL) can offer the capabilities to support the research, prototyping and manufacturing of photonic devices for visible light applications.

NIL is a mechanical lithography process that provides superior resolution capabilities and a high-throughput at a low cost. This technique has been researched for over two decades and a great technology advancement has been achieved. However, NIL is not yet ready for the implementation in the semiconductor industry due to the "high" density of defects, which is a common drawback of all mechanical lithography techniques. Conversely, photonics presents a much more relaxed requirement on defectivity that makes NIL a perfect candidate lithography. Not only NIL meets all of the requirements for the fabrication of most of the photonics devices, it also provides unique advantages in terms of versatility, low cost, resolution and capability for three-dimensional patterning in one lithography step. In fact, photonic and plasmonic devices, biomimetic surfaces and biosensors, opto-electronic chips and other devices have been already demonstrated by NIL.

The goal of this work is to propose and experimentally evaluate new nanofabrication techniques, functional materials and novel device concepts in the field of printable photonics, in order to facilitate the development of new applications in the visible light spectrum. This will be achieved by exploring two aspects of printable photonics in parallel. One concerns the development and testing of nanoimprint *technologies and processes* to pursue the fabrication of progressively more challenging device concepts. Within this research course, we will start with planar optical components and gradually move towards off-the-plane light coupling. We will conclude with an overview about the ongoing research on the imprint of three-dimensional photonic structures. The second aspect of the research focuses on the improvement of *materials* that are used in NIL. Within this theme, we will put forward the idea to couple top-down nano-patterning approaches (NIL) with bottom-up functionalities that emerge from engineering material proprieties at the chemistry level. Thus, purely organic NIL resists that require post-lithography processing are replaced by a high-refractive index functional material that allows the single-step imprint of photonic devices.

These parallel research courses are explored through the theoretical study and experimental fabrication of two photonic devices: an integrated holographic planar circuit for on-chip spectroscopy, and a photonic crystal (PhC) slab printed out of a functional, high-refractive index material. Both these devices present resonances across the full visible spectrum. The amount of integration, complexity and variety of the printed optical components presented here allow us to extend the validity of the work to an even broader range of photonic devices. With appropriate changes in the material choice, the results reported here can be stretched to include devices that work almost over any wavelength range, from X-ray (using metal) to deep infrared and beyond (using silicon first, then other materials).

To give a clear overview of the study, the structure of the dissertation is now presented. In the next paragraphs of this chapter, a historical perspective of optics from the fundamentals to the modern integrated photonics is provided. Current and future applications of photonics are reviewed in paragraph I.3. Chapter II discusses the principles of NIL, the process and material requirements. This chapter introduces fundamentals and notions about NIL that will be recalled frequently over the course of the thesis. The analytical study of Step and Repeat NIL (SR-NIL) on pre-spin coated film is presented in paragraph II.3. The study will be applied to the fabrication of an on-chip spectrometer and will provide insights about pattern filling at the nanoscale during imprint. The state of the art of NIL and motivations to support printable photonics are reported in paragraphs II.4 and II.5 respectively.
Chapter III presents the fabrication by SR-NIL of a photonic device based on a powerful technology for integrated optics called Digital Planar Holography (DPH). This technique can be used to manipulate light in the spatial and spectral domain over a planar waveguide in order to produce on-chip optical transfer functions. DPH technology is studied theoretically (paragraph III.2) and used here to fabricate a novel, miniaturized spectrometer. The photonic device comprises several optical components. Due to its complexity, it can be considered as an ideal testbed to evaluate NIL for integrated optics. Multiple replicas of the chip are fabricated by SR-NIL and etching (paragraph III.4). The fabrication process and optical performance of the imprinted devices are characterized and discussed in paragraphs III.5 and 6.
Following along the parallel research courses described above, an even more powerful approach in presented in Chapter IV and consists of imprinting a functional material to achieve the single-step fabrication of photonic devices. A high-refractive index sol-gel polymer is formulated based on titanium dioxide (TiO_2) and imprinted to create guided light modes on a planar waveguide structure. Direct NIL is used to fabricate linear waveguides and a DPH wavelength demultiplexer (paragraph IV.2). At this point we leave the field of integrated photonics and move towards devices that can be used with off-the-plane light coupling. A new reverse NIL process is reported for the fabrication of transmission PhCs for visible light using the TiO_2 sol-gel material (paragraph IV.3).
The last chapter summarizes all presented results. A brief overview of the ongoing research is finally provided, which gives continuity and extra purpose to the work of this thesis. Preliminary results are reported on the imprint of three dimensional photonic structures and incorporation of a gain medium into our high-refractive index sol-gel material, for applications in light emitting devices. These perspectives fulfill the two aforementioned research courses: developing technologies for printable photonics that can handle increasing device complexity, from two- to three-dimensional structures; coupling more bottom-up material functionalities to top-down technologies as a powerful route for the single-step patterning of active photonic devices.

I.2 Brief history of optics: from philosophy to modern photonics

Optics is the branch of physics which studies the generation of light, its propagation and interaction with matter[2]. Throughout history, our understanding of optics has followed a meandering path, which is nonetheless very interesting to introduce, in order to appreciate how we evolved in almost three millennia from abstract beliefs to the modern science of integrated photonics.

Early studies of the simpler optical phenomena date back to the ancient Greeks and Romans, but the scientific understanding of the nature of light started progressing at a fast pace only around the seventeenth century[3]. Around the year 400 BC, the Greek philosopher Democritus believed that light rays consisted of particles (atoms) traveling through empty space. Together with other prominent philosophers of his time, Democritus contributed to shape the "atomist" thinking. In clear contrast to this vision, Aristotle (384-322 BC) in his treatments "De Anima" and "De Sensu" explained that light is not an object, like an atom of any sort, but rather a quality. According to Aristotle's theory, light is the actuality of being transparent, as a potential that opposes to absence of this quality, darkness. Objects manifest the quality of being transparent through their colors, which participate to the transparency only to a certain degree. Light instead fully embeds this quality and is defined by Aristotle as the "color of the transparent". The far-reaching influence of Aristotle inspired the view about optical phenomena in Europe for many centuries. The atomistic thinking was literally put aside. It was not until 1,800 years later that the idea of light as made of particles became again available, when Poggio Bracciolini in 1417 recovered a manuscript of Lucretius. The reinstatement of the atomistic view by Bracciolini resulted in the formation of two schools of thought in the seventeenth century among the theorists of the corpuscular nature of light. Philosophers and physicists like the eminent Robert Boyle (1627-1691) aligned with the ancient atomistic view and related the nature of colors to the different speed of the light particles travelling through empty space. Whereas Renè Descartes (1596-1650) formulates his plenistic theory of light as the interaction between different types of corpuscular matter that flow in a constantly whirling and wavy ether. Descartes' philosophy greatly influences the thinking of the seventeenth century and generates the current of "plenists". The ancient Aristotelian philosophy opposed to this view and remained mainstream in Europe during the seventeenth century – for instance, Kepler was one of the more distinguished Aristotelians of that period. These three schools of thought contrasted during the seventeenth century. Even so, this made it a particularly fruitful period for the development of optics.

The century begins with the invention of the microscope by Zacharias Janssen in 1600, which allowed a glimpse into a world that was totally unknown before and stimulated advancements in many other fields of science. Some years later, Hans Lippershey first (1608) and Galileo Galilei later (1609) built their first telescope, while Willebrord Snell in 1621 discovered the correct law of refraction. Snell solved the enigma of refraction, a fundamental problem of geometrical optics that had been

investigated since the time of the ancient Greeks. The mathematics of geometrical optics initiated by Snell will be enriched with important discoveries by above all Gauss, Hamilton and Abbe in the centuries to come. It was Robert Hooke in the 1665 who formulated the first real wave theory of light in his *Micrographia*, envisioning light as the propagation of a longitudinal wave in an ether. In the same year, Francesco Maria Grimaldi discovers the phenomenon of diffraction. In 1676, Olaus Rømer determined the speed of light from the delayed eclipses of the moons of Jupiter. Following the wave theory, Christian Huygens in 1678 developed his well-known principle about wavelets. In tepid opposition to the view of light as a wave, Isaac Newton is considered to be the main representative for the corpuscular theory of light in the seventeenth century. In the article "*New Theory about Light and Colors*", Newton describes his famous experiment on the decomposition of white light with a prism and concludes that white light is nothing but the sum of different colors and refractivities. He also states that the colors of objects derive from the varying reflection and absorption of the colors contained in white light, which we now know being the correct explanation. The most important contribution of Newton to the study of light concerns the description of the Newton's rings, as they are called today, which allowed Thomas Young, about 150 years later, to determine the wavelengths of light (1801). Young also formulated the principle of interference and mathematically explained the diffraction of light. The discovery of polarizations by Etienne Louis Malus in 1809 led to a crisis among the theorists of light as a wave. In fact, Malus' observations implied that light, if really wave-like, must be transverse, contradicting the prevailing opinion according to which light propagation as a wave in free-space could only be longitudinal. This period of uncertainty lasted just over 50 years until James Clerk Maxwell derived the fundamental equations of electrodynamics, based on a preliminary work of Michael Faraday. Maxwell's equations tilted everything back in favor of wave-theory. The experimental detection of light waves by Heinrich Rudolf Hertz in 1888 finally made "optics" a branch of electrodynamics. The concept of ether was ultimately shelved in 1905 when Einstein formulated his theory of special relativity.

The solid mathematical model laid by Maxwell that described light as a wave was again questioned when the conservative German theorist Max Plank discovered that a blackbody emitted thermal radiation with a quantized spectrum[4]. Einstein later generalized the idea of these "quanta" and proposed that light itself was quantized. He also explained the photoelectric phenomenon and introduced the idea of stimulated emission that will be useful later for the invention of the maser and laser. These were the seeds of the forthcoming quantum revolution. The extension of the new born theory of quantum mechanics to light and its dualism wave-particle resolved at last the ancient debate about the nature of light that afflicted philosophers and physicists for millennia. Ironically, both atomists and wave-theorists had been correct and wrong for all that time. In 1926, Gilbert Lewis, referring to these quanta of light, coined the term "photon".

The development of photon statistics and counting started in 1950, following Brown and Twiss' experiments on intensity correlations for stellar interferometry. The field of quantum optics is introduced in this period and it is as today the most precise

and complete model of optics available (Figure 1). Optical pumping probes of light interaction with atoms began to be developed in the 1950s by Kastler, Brossel, Series, Dodd and others. In the same decade, Townes and his group developed the maser (microwave amplification by stimulated emission of radiation), based on precise initial state preparation, population inversion and stimulated emission[5].
Thanks to these impressive developments, the 1950s are years of spectacular renaissance for optics. But the real breakthrough that radically transformed this field did not come until the 1960, when Maiman at Hughes Research Laboratories in Malibu invented the laser[6]. Lasers allowed for the first time the availability of light source with high spatial and temporal coherence and very high brightness. Nevertheless, the invention of the laser was not welcomed as a revolutionary and enabling technology at first. Like Townes himself said in an articled of 2003[7]:

> When the first laser appeared, scientists and engineers were not really prepared for it. Many people said to me—partly as a joke but also as a challenge—that the laser was "a solution looking for a problem".

In spite of the initial skepticism, lasers paved the way for the modern photonics and are now the cornerstone of this field. Two other technological advancements must be added to the invention of lasers to understand the transition between classical optics and photonics. First, the development of microfabrication techniques and semiconductor-optical devices for the generation and detection of light, which permitted efficient and compact optoelectronic devices. Secondly, the introduction of methodologies for the fabrication of cheap optical fibers with very low propagation losses. These scientific and technological advancements brought together seemingly separated scientific disciplines and fields of engineering. Optics is forced to describe a new family of electro-optics, optoelectronics and quantum electronic devices. This gives birth to the field of photonics as the discipline that studies the “flow of photons” in analogy with electronics, which instead studies the “flow of electrons”.

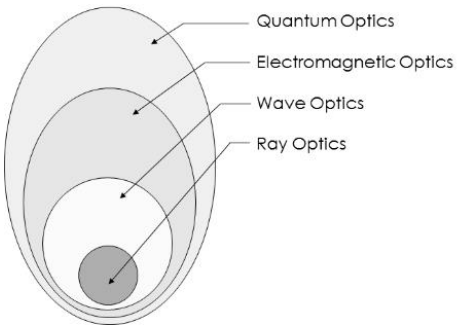

Figure 1 – Each set represents a model of optics. The extent of each subset indicates the range of validity of the model. Under certain hypothesis, simpler models can be implemented. The most exact model of optics as of today is Quantum Optics.

The development of waveguide technology at the end of the 1960s was the key step toward the integration of multiple devices on a chip and gave specificity to the field of photonics, enabling what is today called "integrated photonics" or "integrated optics" (Figure 2). The term was first proposed by Miller in 1969 as a similitude to put in relation planar optical circuit technology with the well-established integrated micro-electronics[8]. The boundary between what is defined as photonics and integrated photonics is blurred. Strictly speaking, integrated photonics and photonic integrated circuits (PICs) can be considered as a subset of photonics. A PIC is more specifically defined as the confluences of various passive and active optical devices on a single chip, which are interconnected by transmission lines, or waveguides. Waveguides are the fundamental component of a PIC that interconnects basic building blocks such as lasers, detectors, switches, splitters, gratings, resonators, photonics crystals, couplers, polarizers, modulators, junctions, filters, and focusing components among others. The main motivation for the integration is lowering the cost of advanced optical systems, which justified the investments for research and development (R&D) of PIC applications since the beginning. The fabrication of the first three-dimensional (3D) integrated lithium niobate ($LiNbO_3$) waveguide was demonstrated at the AT&T Bell Laboratory in the mid-1970s[9]. This gave rise to the development of waveguides with low losses and by mid-1980s devices based on $LiNbO_3$ waveguides reached a modulation speed of 40 GHz. However, market entry requires that a technology meets certain standards and the evolution of PICs was not dissimilar to that of many other technologies: discovery, fast evolution, and the wait for applications[10]. Some years after the demonstration at the AT&T Bell Labs, the packaging requirements for the telecommunication systems were met and the first PICs entered the market following and backing up the boom of optical fiber systems. The call for more bandwidth pushed the development of wavelength division multiplexers, which were integrated with modulators and switches on a chip. A variety of new devices were invented in those years, thanks to the development of other materials such as glasses, polymers, silicon, and semiconductors like indium phosphide (InP) and gallium arsenide (GaAs).

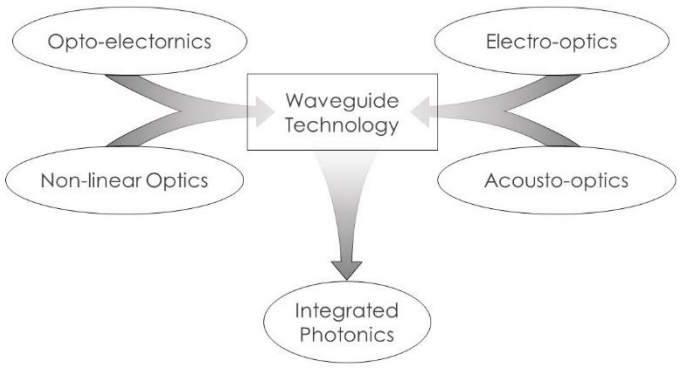

Figure 2 – Confluences of the different fields of optics into Integrated Photonics, by means of waveguide technology. The blurred line between integrated photonics and photonics is more clearly marked by whether or not waveguides are present in a photonic circuit.

Silicon photonics takes hold officially in the late 1980 and mid-1990 when the first silicon-on-insulator (SOI) wafer is fabricated[11]. The reason for the introduction of this new wafer was to reduce parasitic capacitances for electronics. As an indirect consequence of the material choice, the wafer also exhibited interesting photonic properties due to the excellent near infrared (NIR) light confinement inside the silicon layer. The pioneering work of Soref and Lorenzo[12,13] inspired development in silicon photonics with the microfabrication of passive components as waveguides and active devices such as switches and modulators.
During the last three decades the demand for PICs spiked. The amount of data transferred on fiber optics is exponentially growing and photonic circuits capable of an astonishing 1.05 Peta-bit/sec have been already demonstrated[14]. Scientists at the University of California, Berkeley, Massachusetts Institute of Technology and Colorado University have demonstrated very recently the full functioning of an integrated electro-photonic circuit that employs optical interconnects send/receive data between microprocessor and memory. This huge achievement solves the issue of band cutoff in metal wires and was obtained with standard semiconductor processes[15]. Other than integrated photonics for information transfer at all scales – within the same chip and for long range telecommunication – there is also a variety of applications where photonics is increasingly taking hold. These applications describe photonics as a seamlessly evolving science that could potentially become an even bigger driver of economic growth. The following paragraph offers a review of the most enabling PIC technologies as per today and a future outlook.

I.3 The present and future of photonics

Advances in photonics have enabled the development of novel technologies that address significant scientific challenges and that have transformed our life. There is not a single review article in the scientific literature deemed to be inclusive of all of the applications in such a vast topic. Photonics is everywhere around us: medical and health sciences, energy efficiency and renewable energy, material processing in production, homeland security and defense, environmental and sustainable living, lightening and photovoltaics to everyday products like mobile phones and DVD players. The discovery of new materials, device concepts, and nanofabrication techniques have enabled the fabrication of complex PICs, such as nano-optomechanical structures[16,17] (Figure 3a), sub-wavelength gratings[18,19], and 3D photonics[20] (Figure 3b). One of the most successful achievement of modern photonics is the possibility to engineer a dielectric material to function as a crystal for photons very much like a semiconductor does for electrons[21]. Photonic crystals (PhCs) and PhC cavities are used today in many cutting edge technologies[22], such as ultra-low threshold lasers[23], solar cell technology[24], and lab-on-a-chip (LOC) biomedical devices[25,26]. In particular, biomedical sensors and early-diagnostic devices have enjoyed a significant leap forward due to capabilities such as high-sensitivity and low level of detection provided by photonic sensors. The most famous application of photonics in the medical field is probably optical coherence tomography, an

inexpensive, non-invasive and practical tool for imaging tissue and pathology diagnosys.[27] The monolithic integration of photonic components with micro-nanofluidic devices has also yielded a great variety of photonic sensors for biology and medicine. A photonic biosensor functions by reading a variation of the refractive index (RI) caused by a biomolecular event, such as binding of a target antigen to an antibody. Several PICs can be engineered to exhibit a detectable change in wavelength or light intensity upon a tiny change in RI, yielding a high sensitivity. Photonic biosensors commonly integrate Mach-Zehnder, Young, and Hartman interferometers, as well as grating-coupled, slot waveguides, ring resonator and opto-nanomechanical devices, which have proved a detection limit down to $\Delta n/n=10^{-8}$.[25] Companies like Farfield, SRU Biosensing, Corning, Axela, Microvacuum, and Genalyte among others have already commercialized photonic biosensors.

The use of quantum dots (QDs) and colloidal QDs as an active media has also contributed to add functionalities to solar cells[28], light emitting devices[29,30] (Figure 3c), displays[31,32], biomedical imaging, sensing and labelling devices[33]. QDs are also being used in research for the future solid-state based quantum computers[34,35]. Spectral imaging is another branch of optics that emerged from the implementation of the most advanced nanofabrication techniques. The simple integration of optic filters and photonic nanostructures onto cameras can transform them into powerful multispectral and hyperspectral sensors, which are essential tools applied today in medicine, astronomy, remote sensing, airborne taxonomy and food quality control[36-39]. Non-linear optics[40] and ultrafast optics[41] are other exciting areas of research in photonics. Non-linear optics has already enabled the generation of visible light out of infrared sources by frequency doubling in commonly used laser pointers[42]. Some of the applications permitted by ultrafast optics include micromachining transparent materials by femtosecond lasers[43], precise intra-tissue surgery[44], and 3D optical storage[45]. Another staggering application of ultrafast photonics is computational photography. Scientists have already demonstrated the capability of recovering 3D shapes from around a corner using ultrafast time-of-flight imaging[46] (Figure 3d). Finally, a fast growing field of research in photonics is 3D vision, virtual reality (VR) and augmented reality (AR)[47,48]. Multiview 3D[49] (Figure 3e) and stereoscopic[50] displays, holographic devices[51-53], nanophotonic phased array[54] and AR apparatus based on fiber optics[55] are some of the main technologies deployed to tackle the challenge of 3D vision. Commercial applications of AR would be endless and would span military, surveillance, navigation systems, situational awareness, geo-located information retrieval, in-situ/real-time augmentation of CAD design, disability aids, gaming, products for the entertainment industry and so forth[56]. As our understating of all the aforementioned fields of optics matures and our nanofabrication capabilities advance, the sphere of influence of photonics is meant to grow. Faster internet, more sensitive biosensors, point-of-care devices, more efficient light-emitting sources and solar cells, quantum computers, cheaper, faster and bigger data storage and even new capabilities such as "seeing around the corner" and AR vision are some of the innovations that will be available in the close future. A reduction of the networks' carbon footprint and overall cost per bit will result from the increase in data capacity, while smart power grid, buildings and industrial process control

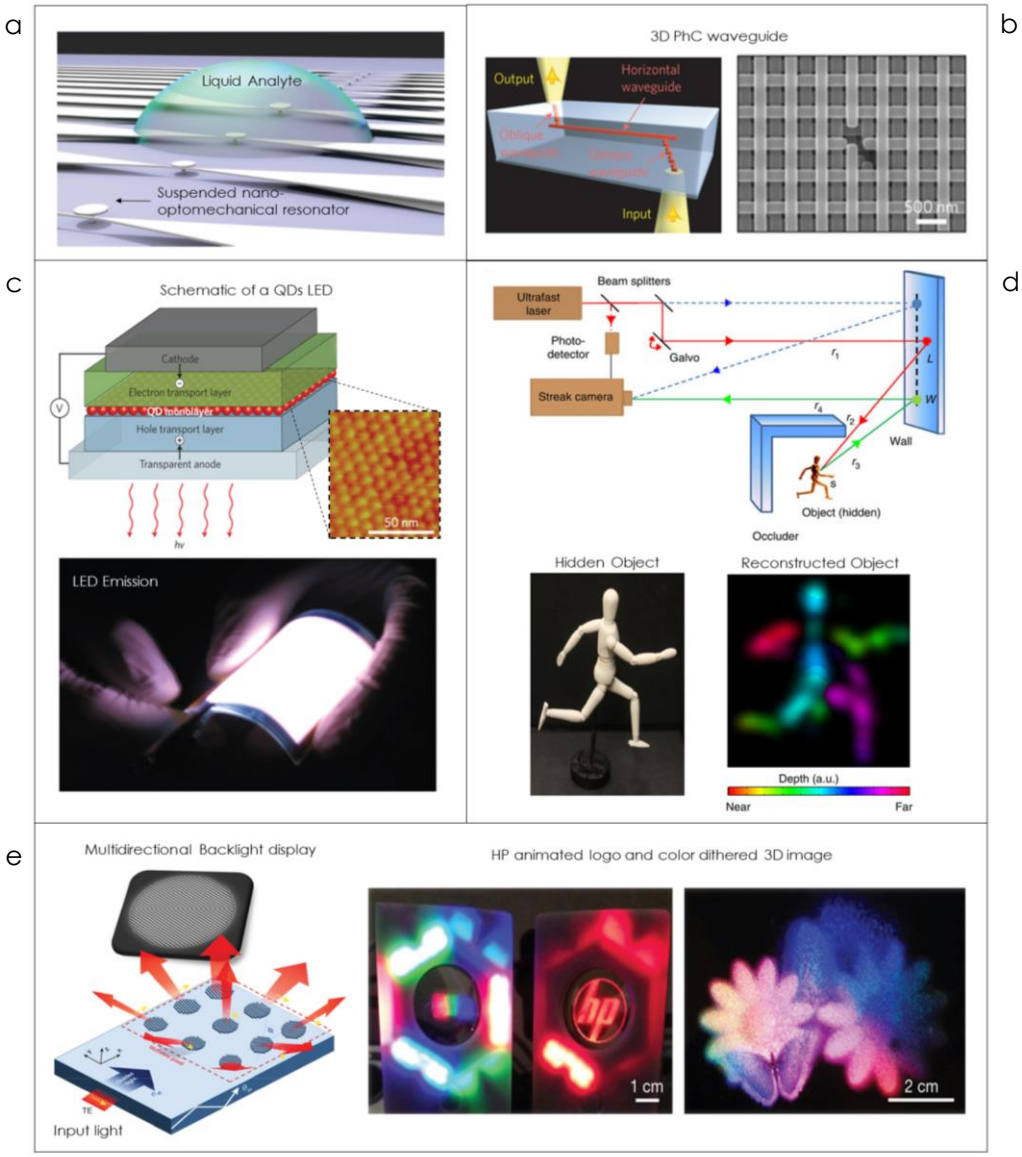

Figure 3 – Cutting edge applications of photonics. a. Schematic of a high-frequency nano-optomechanical disk resonators in liquids for biological spectroscopy.[17] **b.** Infrared light guiding in a 3D PhCs through an oblique-horizontal-oblique waveguide. Working principle of the 3D PhC waveguide (left) and SEM top-view image of the device.[20] **c.** Colloidal quantum-dot light-emitting device. Layer stack of the emitting device (top) and an actual picture of the LED (bottom).[29] **d.** Recovering 3D shape around a corner using ultrafast photonics. Schematic of the experiment (top), actual and reconstructed object around a corner (bottom).[46] **e.** Multi-directional backlight for a glasses-free, wide-angle three-dimensional display. Display working principle (left) and 3D reconstructed images from the display.[49]

will significantly contribute to meeting environmental challenges.

A photonic revolution has started and we are right in the middle of it. According to the Photonics Industry Report 2013, the world market photonics has grown by 53.5% from 2005 to 2011 (Figure 4a), and it is expected to reach 615 billion euros

by 2020.[57] This corresponds to a growth of +76% compared to 2011. The same report shows that all subfields of photonics have grown faster than the world gross domestic product (GDP) over the last 6 years and they are expected to keep on this trend until at least 2020 (Figure 4b). The photovoltaic industry ranks first for annual growth, while projections show that the market of displays will be the predominant in volume. Leverage factor of photonics on other industries is 40% in average, with the industry of media and broadcasting receiving the biggest support.[57] Other industries like food and beverage production, manufacturing of chemicals and pharmaceuticals, textiles and clothing, vehicles and large machinery, oil and gas exploration among others are strongly supported by advancements in photonics. This data describe photonics as an essential component of today's progress that encompasses all industries and fuels economic growth. For this reason, photonics is also defined as an "enabling technology". Nations and industries worldwide are aware of the role of photonics and committed to more investments for future developments. A Photonic Public Private Partnership (PPP) was proposed in the *Horizon2020* framework through a long-term commitment of the European industries and governments, which will lead to a more competitive photonics sector in Europe.[58] With the PPP, a total investment of €7 billion in photonics was agreed between the private sector and the European Commission.

The United States of America is also leading a program to drive the US competitiveness in the field of photonics through investment in public-private partnerships and workforce development. The comprehensive work of several US optical societies and organizations lead to the formation of a National Photonics Initiative (NPI) in 2012[59]. One big round of investments of $200 million for the creation of an Integrated Photonics Manufacturing Institute was announces by the White House in October 2014.[60] The lead in research of integrated photonic technologies for the US was assigned by the Obama administration to the American Institute for Manufacturing of Photonics, located in the University of California, Santa Barbara. These decisions are expected to boost photonics manufacturing, bring more skilled, high-tech jobs and establish the global leadership of US in photonics.

In spite of the remarkable potential of this field, photonics – especially in the visible regime – requires using cutting edge technologies. This problem is amplified by the difficulty to converge on standard protocols and materials due to the sheer number of applications (see paragraph II.5). While conventional computer logics is about to hit its physical limits and photonics could bridge this technological gap, profitability of ICs is still much higher than PICs. In many cases, the advantages provided by integrated optics are neutralized by the expensive fabrication processes. The established ICs integration technologies make certain electronic functionalities very hard to replace by their photonic counterpart – i.e. optical interconnects. To make many applications actually viable and profitable, photonics must gain a strong competitive advantage. A technology must be coupled to photonics that can mold to all of the different applications and enable them at a low cost.

We believe that economy-to-scale benefits can be achieved in integrated photonics by means of NIL, yielding a new field called 'printable photonics'.

Figure 4 – Study on the growth of the world market of photonics (source: Photonics21, Industry report 2013).[57] **a**. Market size as function of the technology area. **b**. Volume and GDP associated to each area of photonics (CAGR stands for Compound Annual Growth Rate).

NIL is one of the most versatile fabrication techniques and suits the required cost-effectiveness and technological specifications of numerous photonic devices. Printable photonics is researched here as a solution that can provide the necessary competitive advantage to many photonic applications to more easily reach the market. The next chapter goes over the fundamental notions of NIL and its applications, which are important to understand the work that is reported in the following chapters and the significance of this study.

II. Nanoimprint Lithography

II.1 Introduction to Nanoimprint

Nanoimprint Lithography (NIL) is a mechanical method of replication where nano and micro reliefs from a template – also called mold or stamp – are casted into a thin polymer coating, called NIL resist. As a result of the imprint, a thickness contrast is formed in the polymer, which allows for pattern transfer into an underneath layer. In NIL, pattern transfer consists of two etching steps: one to remove the residual polymeric layer and another to etch the imprinted features into the substrate. NIL is conceptually very simple, capable of sub-10 nm resolution, relatively inexpensive, and potentially a high throughput technique.

Stephen Chou is regarded by many as the pioneer of NIL.[61] In 1995, as scientists were struggling to engineer a lithography system that would bring the gate of transistors from 350 to 250 nm, Chou demonstrates that features down to 25 nm can be achieved by NIL. The one order of magnitude improvement in the resolution enabled by NIL struck people's attention at the time and quickly resulted in a widespread interest around NIL. After all, the main driver for the development of NIL at the time was the necessity to have a reliable and inexpensive technology capable of high resolution and throughput for the integrated circuit (IC) industry.[62] In spite of the initial reluctance of the industry, for many others NIL seemed to be the key to unlock this issue. Lithography in the IC industry accounts for up to 35% of the total chip cost. This is why considerable efforts were, and still are, devoted to the research of the so-called next generation lithography (NGL) techniques, such as extreme UV, multi-beam, dip-pen, and deep UV lithography.[62] Unfortunately, some of these techniques are still in their embryonic stage. Others, while more advanced, are very expensive or have a low throughput. The issues associated with all the other NGL systems, reinforced the belief that NIL could be potentially the innovative technology that would allow another acceleration of Moore's law and dramatically cut the cost of production. In 2003 MIT's Technology Review defines NIL as one of the 10 technologies that are likely to change the world.[63] New companies and established tool manufacturers such as EV Group[64], Obducat[65], Nanonex[66], Suss MicroTec[67], Smart Equipment Technology[68], NIL Technology[69], and Molecular Imprints Inc.[70] (MII) begin to produce NIL machines and offer imprint services.

However, some argue that NIL was not a completely innovative lithography method. Embossing techniques had been around for at least 15 years for making compact disk and other data storage devices.[71] Independently from the work of Chou, J.

Haisma *et al*, at Philips Research Labs in The Netherlands, had also developed a technique called mold-assisted nanolithography for pattern replication.[72] Their results were not as impressive, but their technique was basically identical to NIL, it involved a residual layer etch and was capable of pattern transfer just like Chou's NIL. A paper of 2009 describes a molded mask lithography method implemented at the NNT laboratories (Japan) as early as in the 1970s.[73] Surprisingly, the molded mask method is essentially a lower-resolution NIL, with a residual layer and pattern transfer etch steps.

Regardless of how far back in the past the advent of NIL should be placed, it is only after Chou's paper of 1995 that the exploration of this technology really began. In the past 20 years, scientists have demonstrated the unique capabilities of this technology with a variety of applications. NIL has an extraordinary flexibility and can adapt to pattern a huge variety of devices on the most diverse substrates. Organic electronics[74], nanoelectronic devices in both silicon[75] and gallium arsenide[76], organic lasers[76], organic LEDs[77], memristors[78], high density magnetic data storage[78,79], biology substrates[80,81], biosensors[82-84], and biomimetic devices[85,86] and others have been achieved by NIL. Photonics is also one of the most suitable fields of application of NIL and many photonic devices have already been demonstrated (see paragraph II.5).

Over the last few years, NIL branched off into several categories, but it primarily subdivides into thermal NIL (T-NIL) and ultraviolet NIL (UV-NIL). T-NIL is the first version of NIL and functions by pressing a pre-heated stamp against a thermoplastic polymer that was previously spin-coated on a substrate. If the mold is heated above the glass transition temperature of the polymer, this melts and fills the mold reliefs (Figure 5a). UV-NIL is reported for the first time in the paper of Haisma *et al* in 1996,[72] but three year later Prof. Grant Willson's group invents Step and Flash Imprint Lithography (S-FIL) which historically changed the prospect of UV-NIL.[87] In S-FIL, a low-viscosity UV-curable polymer is used instead of thermoplastics and the filling mechanism is dominated by capillary forces. The resist is crosslinked under the action of UV radiation, then the mold is released leaving a patterned resist on the substrate. This technique enables an imprint at a low pressure and temperature, and offers several advantages such as increased throughput, process reliability, and versatility. In its original version, S-FIL required the UV-resist to be spin-coated on the substrate (Fig. 5b) and was also defined as Step and Repeat NIL (SR-NIL). In SR-NIL, a stepping process is carried to pattern the full wafer, since the template is smaller than the overall substrate. In a successive version of S-FIL the resist is dispensed via ink-jets or similar systems (Fig. 5c). This version of S-FIL was called Jet and Flash Imprint lithography (J-FIL). To date, when referring to a UV-NIL technique where the resist is dispensed by ink-jets, people use equally the terms S-FIL and J-FIL. The original version of S-FIL, with spin-coated resist, is called SR-NIL on pre-spincoated film,[88] or spun-on NIL,[89] to distinguish it from the droplet-dispensed version. J-FIL is more expensive than SR-NIL on pre-spincoated film, but it is perhaps the most viable NIL technique to meet the manufacturing requirements in the IC industry (see paragraph II.4). Another implementation of NIL was introduced by Guo's group in 2002 and it is called

reverse NIL (R-NIL).[90] In R-NIL a polymer is spin coated directly onto a template, cured and then transferred to a substrate. The release of the film is a critical aspect of this technique and is achieved by properly tuning the surface energies of both mold and substrate. This unconventional technique is very useful particularly to make 3D nanostructures.[91,92] R-NIL will be more thoroughly discussed in the last chapter of this thesis when the fabrication of PhCs with a TiO_2-based functional material is reported. Other popular types of NIL are roll to roll (R2R-NIL), roll to plate (R2P-NIL), combined NIL and photolithography (CNP), resist-free direct NIL, electrochemical NIL, laser-assisted direct imprint, and ultrafast NIL. In this work, ultraviolet SR-NIL on pre-spincoated film is used to fabricate the holographic spectrometer and other integrated photonic devices with the TiO_2-based functional material. From now on, we will refer to this technique as SR-NIL, omitting the "on pre-spincoated film" for the sake of conciseness. Considerations on mold and resist requirements for UV-NIL are reported next, and paragraph II.3 shows a detailed study on the pattern filling mechanism in SR-NIL.

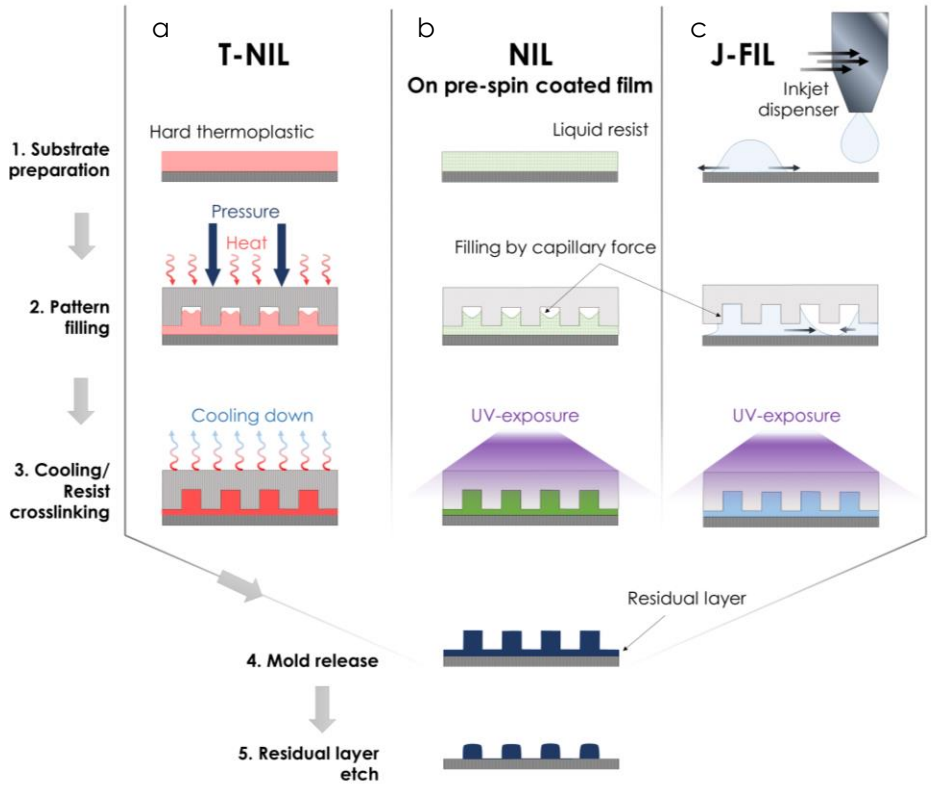

Figure 5 – **Process flow of the most common NIL technologies**: **a**. Thermal NIL. **b**. NIL on pre-spin coated film. **c**. Jet and Flash NIL.

II.2 UV-NIL mold and resist

Molds in NIL are usually fabricated by electron beam lithography (EBL), thus their cost can be very high, especially in case of narrow, dense patterns.[93] The only method to circumvent high costs in large templates is to use SR-NIL and stitch multiple replicas to cover a large area. Due to the high cost of mastering and the risk of wearing during imprint, a master-template is commonly replicated into soft or hard stamps, called daughter molds, which are then used hundreds to thousands of times in the actual NIL process. In case of UV-NIL, either the mold, the substrate, or both of them must be transparent to allow resist cross-linking by UV light. When soft stamps are used, such as polydimethylsiloxane (PDMS), the master template is fabricated in SOI wafers,[93] or patterned hydrogen silsesquioxane (HSQ) on silicon.[94] Soft-stamps are very inexpensive and can locally deform, for example when a particle is present between stamp and wafer. This improves the imprint quality and yield, since the mold wraps around the particle, minimizing the area that is not imprinted. For the same reason, soft molds conform to the wafer waviness and can produce very uniform imprints, even on flexible or highly curved substrates.[95,96] On the other hand, soft stamps generally cannot be used for high fidelity replication of complicated patterns. They also offer limited spatial resolution, and can cause harmful bending under locally irregular load.[93] To mitigate these problems, the softness of the stamp can be tuned by using hard PDMS (h-PDMS) or Ormostamp.[97] Hard molds are usually made out of quartz or fused silica and can replicate patterns with resolution down to 4 nm half pitch.[98] Other than providing high-resolution capabilities, hard molds are more durable than soft molds and cause less line paring during demolding. Line pairing consists of collapse of adjacent lines onto each other and can be an issue when using soft-molds. It is caused by surface charge generation due to friction during demolding.[93] Hard molds can be fabricated by additive or subtractive processes. C. Peroz *et al* demonstrated that high-resolution additive fabrication of UV-NIL stamps is possible by EBL on a layer of HSQ that is spin coated on a quartz template.[99] HSQ is usually coated with Aquasave,[100] a conductive polymer that helps discharging the substrate and prevents pattern distortion during EBL writing. Atomic layer deposition (ALD) of oxides can also be performed onto patterned HSQ to reduce the trench size.[99] Using a similar additive approach, we demonstrated a double patterning technique and halved the pitch of lines writte by EBL.[101] Subtractive methods for the fabrication of hard molds require an etch step of the bulk quartz or silica template. In case of direct EBL writing onto a mold, a layer of chrome (Cr) is deposited beneath the EBL resist, which can function as both a discharging layer and hard-mask for pattern transfer.[102] After development of the EBL-resist, patterns are etched into Cr, then into the bulk template. If the mold is replicated from a master-template, the process comprises an extra etching step for the residual layer prior to pattern transfer. Subtractive techniques offer high robustness of the patterns compared to additive methods, but they require very difficult etching processes and a time-consuming calibrations in case of high resolution patterns. Fabrication of complex 3D molds has also been demonstrated

by helium ion beam and focused ion beam.[103,104] Another course of work is the fabrication of templates by self-assembly techniques for bit-patterned magnetic media data storage, which has been pursued by laboratories and large manufacturers, such as Hitachi Global Storage Technology and Seagate.[105,106]
Mold preservation is also a very important aspect of NIL and several studies have been conducted on this topic. By choosing the proper polymer resist and thickness, the mold can be prevented from contacting the hard substrate during imprint and rather land on a 'soft-cushion' formed by the residual resist.[62] Another crucial issue of NIL is the control of the adhesion forces that act on the mold and substrate during demolding. Adhesion of the mold to the substrate, through the resist, is highly undesirable in NIL, since it can cause pattern tearing that can ruin both imprinted dies and mold (see next paragraph). Soft molds are typically fabricated using plastics, fluoropolymers, and silicones that have a low surface tension, thus do not require any surface treatment to decrease the adhesion proprieties. Conversely, hard molds suffer from a higher surface tension. Denser patterns also lead to an increase in the total surface area and adhesion effect. For this reason, surface treatments are necessary for hard molds to ensure that the resist preferably holds to the substrate and does not adhere to the mold. Surfactant molecules like 1H,1H,2H,2H-perfluorodecyl-trichlorosilane can be deposited as a liquid or vapor phase. Molds treated with vapor phase coating have shown better performance in the imprint of high-resolution patterns since vapor can infiltrate through narrow features more easily than liquid.[107] A common strategy to test the durability of a hydrophobic coating is to use the stamp multiple times, compare the sequentially imprinted patterns and monitor the wearing of the surfactant layer.[62]
Resists are also a fundamental constituent of a successful imprint and need to be tailored to the specific type of process. In case of UV-NIL, a resist must have a low viscosity, low shrinkage, high resolution, fast curing, and a high etching selectivity to allow pattern transfer. The time required for pattern filling is directly proportional to the viscosity of the resist (see paragraph II.3). So, a low viscosity is necessary to reduce the imprint time. Nevertheless, defect-free, uniform films are very hard to achieve with a low viscosity material by spin coating, therefore a fine tuning of the resist formulation is needed. The photo-polymerization reaction that occurs in the resist during curing is also known to generate volumetric shrinkage in the resist. This can be minimized by choosing a suitable type and concentration of photoinitiatior, in order to attain imprints with a high pattern fidelity. Finally, a good selectivity to plasma etch with fluorine-based recipes – usually employed for silicon, silica, and quartz etch – can be tuned by selecting components that contain particular cyclic or aromatic moieties.[108] The two classes of polymers that are usually considered for application in UV-NIL are acrylates and epoxy compounds, which present a free-radical and cationic polymerization processes, respectively. The resist that we use here for the fabrication of the nano-spectrometer in Chapter III by SR-NIL is called mr-NIL200 and it is produced by micro resist technology GmbH[97]. For a more detailed description of these resists, refer to paragraph III.4

II.3 Resist flow dynamics at the nanoscale

A complete model of the pattern filling during casting is not straightforward due to the great number of parameters to consider. However, an understanding of the flow dynamics in NIL is essential to prevent filling issues, such as bubble trapping. There have been some attempts to analytically predict the behavior of viscoelastic resist at the nanoscale for some specific NIL scenarios. The most common studies are about J-FIL and T-NIL. The squeeze-flow theory describes the dynamics of a drop spread between two parallel plates and is at the foundation of J-FIL.[15] Interesting results were obtained from basics models and simulations by X. Liang and S. Chou about air bubble formation and trapping in J-FIL.[109] They showed the dependence of the bubble formation from mold pattern distribution and droplet dispense geometry. The authors also simulated the dependence of the bubble dissolution time from the imprint pressure, resist viscosity, solubility of air in the resist, and residual layer thickness. K.-D. Kim *et al* later showed how a fine tuning of the resist contact angles with both substrate and mold can greatly decrease the probability of bubble formation.[110] Investigations of the confinement and dynamics of the resist spread, flow behavior, and polymer deformation were performed for T-NIL and hot embossing.[111-115] As for SR-NIL, in spite of its popularity in research labs and universities, there is not a complete model for pattern filling in the literature, neither analytical nor experimental. Fluid dynamics in case of SR-NIL is ruled by capillary like in J-FIL, however the filling mechanism of these two techniques is very different. In J-FIL the mold touches the dispended resist drop when it is still hundreds of nanometers thick. This leads to transverse pattern filling, where air is pushed along the mold trenches and it is finally absorbed by diffusion into the resist. In SR-NIL the mold has to sink through a uniform resist film. So there is no immediate transverse filling, unlike in J-FIL. Models for T-NIL also cannot be used for SR-NIL because in T-NIL the imprint occurs at high pressures, with very high resist viscosity (~MPa·s), in a regime where capillary is relatively low. K. Y. Suh *et al* have formulated a model of capillary kinetics in case of capillary force lithography (CFL).[116] This study comes closer to modelling the resist flow for SR-NIL as well, but it fails to consider the time evolution of the air pressure inside the protrusions in case of impenetrable mold.[117] To understand the phenomena occurring at the nanoscale during SR-NIL, a new model must be found.

Here, an analytical model of the resist dynamics at the nanoscale for SR-NIL is derived from simple considerations and some restrictive assumptions. Let us consider a cylindrical tube with sizes such that the Reynolds number returns a uniform, laminar flow. If one extremity of the tube is immersed in liquid, this will experience a differential Laplace pressure pointing upward given by the following formula:

$$P = \frac{2\gamma \cos\theta}{r} \tag{1}$$

where γ is the surface tension of the liquid, θ is the contact angle at the three-phase contact line and r is the radius of the tube. The Laplace pressure will push the liquid upward with a volumetric flow rate given by the Poiseuille equation:

$$\frac{dV}{dt} = \frac{\pi r^4}{8\eta z} P \tag{2}$$

where η is the viscosity of the liquid and z is the length of the tube. If we substitute (1) in (2) we get:

$$\frac{dz}{dt} \propto \frac{\gamma \cos\theta}{\eta z} r \tag{3}$$

Formula (3) shows that the velocity of the capillary rise is inversely proportional to the length the fluid has already travelled and to the viscosity. While this simple equation provides some insights about the flow rate in elementary configurations, it fails to predict the behavior of the resist in the real case scenario of SR-NIL. In fact, the equation predicts an increase in filling velocity for larger features (larger r), which is the opposite of what experimentally observed. More importantly, equation (3) does not account for the effect of the resist flowing in the narrow gap between the mold and the substrate.

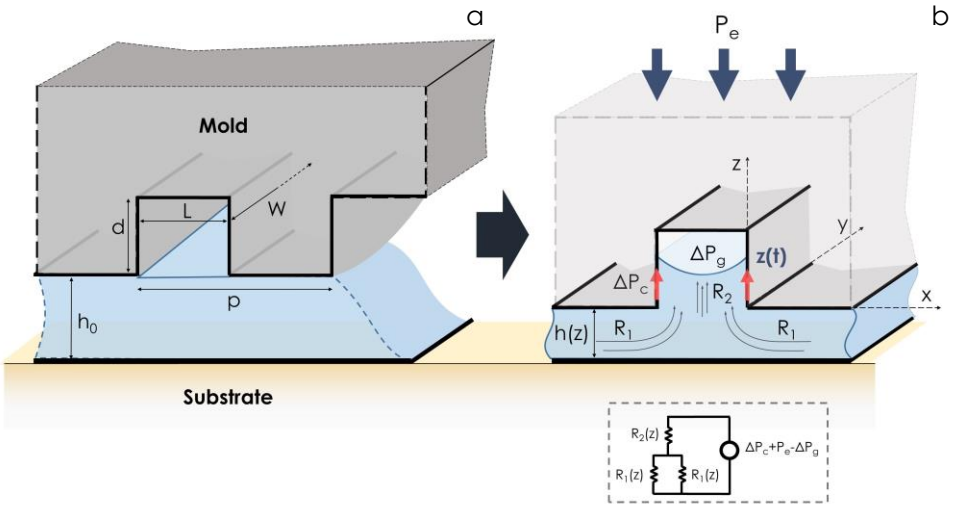

Figure 6 – **Detailed view of the mold/resist contact during SR-NIL on pre spin-coated film. a.** Nomenclature of geometrical sizes is provided in this sketch. Note that the mold is not yet in contact with the resist at this point. **b.** The mold is in contact with the resist film and the polymer starts to fill the trench due to the strong capillary forces. The inset shows the lumped model of the resistances that oppose to the flow of resist.

Figure 6a shows a simple geometry that we can consider to obtain a more precise model of the filling mechanisms in SR-NIL. The assumptions we make to study the viscous flow are the followings:

1) Resist is a Newtonian liquid.
2) Resist is incompressible.
3) Viscosity of the resist does not depend on the fluid velocity and gap of the channels.
4) Henry's constant of the air with the polymer (solubility of trapped air into the resist) does not depend on the pressure.
5) Diffusion of air into the polymer is ruled by Henry's law, so concentration of air in the resist only depends on the pressure of the trapped air and no saturation ever occurs.
6) No species diffuse from the polymer to the trapped air in the trench, so only diffusion of air into the resist is considered.
7) Effect of the meniscus in the capillary rise is not considered.
8) The process is isotherm.

To study the filling process, we are considering an infinitely long grating so the filling is a 2D problem in the plane xz. The grating has pitch p, linewidth L, and pattern depth d. Under the mentioned hypothesis the dynamics of the resist flow can be described as follows. When mold approaches the flat resist film that has a thickness h_0, the resist is dragged inside the grating due to a Laplace pressure differential, given by the equation (1). The overall resistance to the flow is the combined contribution of the friction experienced in the channels formed underneath the mold. These channels have width $h(z)$, whose evolution is also related to the capillary rise by a series of geometric consideration (see Appendix A). As the resist fills the patterns, $h(z)$ decreases, slowing down the flow. The resistance of the flow inside the mold is also ruled by the width of the trench L and the height of the filling z. As the resist meniscus rises inside the trench, the pressure of the air trapped in the gap increases, further slowing down the rise. When the air pressure equals the Laplace pressure, the flow stops. If not escape for the gas trapped inside the gap is present, this will diffuse into the resist. The absorption of a gas in a liquid is ruled by Henry's law, which states that the quantity of gas (in moles) that diffuse inside a liquid is proportional to the relative concentration of the gas in the gap and to a constant called Henry's constant (H^{cp}). The time dependence of the diffusion is described by an integral and depends on a diffusion constant β. Both H^{cp} and β must be determined empirically for a given imprint resist and gas. The lumped model of the capillary flow is shown in the inset of Figure 6b. The mathematical description of the filling dynamics returns an integro-differential equation whose explicit solution is very complicated to attain (see Appendix A). The equation is solved numerically and plotted in Fig. 7 for different values of diffusion constant, resist viscosity and pattern size. Fig. 7a shows that when the diffusion constant is infinite, the trapped air is absorbed instantaneously by the resist and the filling velocity is only given by the resist viscosity and geometrical configuration of the mold patterns. The pitch, linewidth and pattern depth are 200 100 and 100 nm respectively. As β decreases, the resist fills the protrusions only to some extent and stops to allow the gases inside the gap to decompress as the diffusion into the liquid polymer slowly occurs. The smaller the diffusion time the longer the filling time, but filling is complete as long as H_{cp} is large enough. The derived equation in Appendix

A shows that if Henry's constant is not large enough, the filling may be incomplete even after an infinite time.

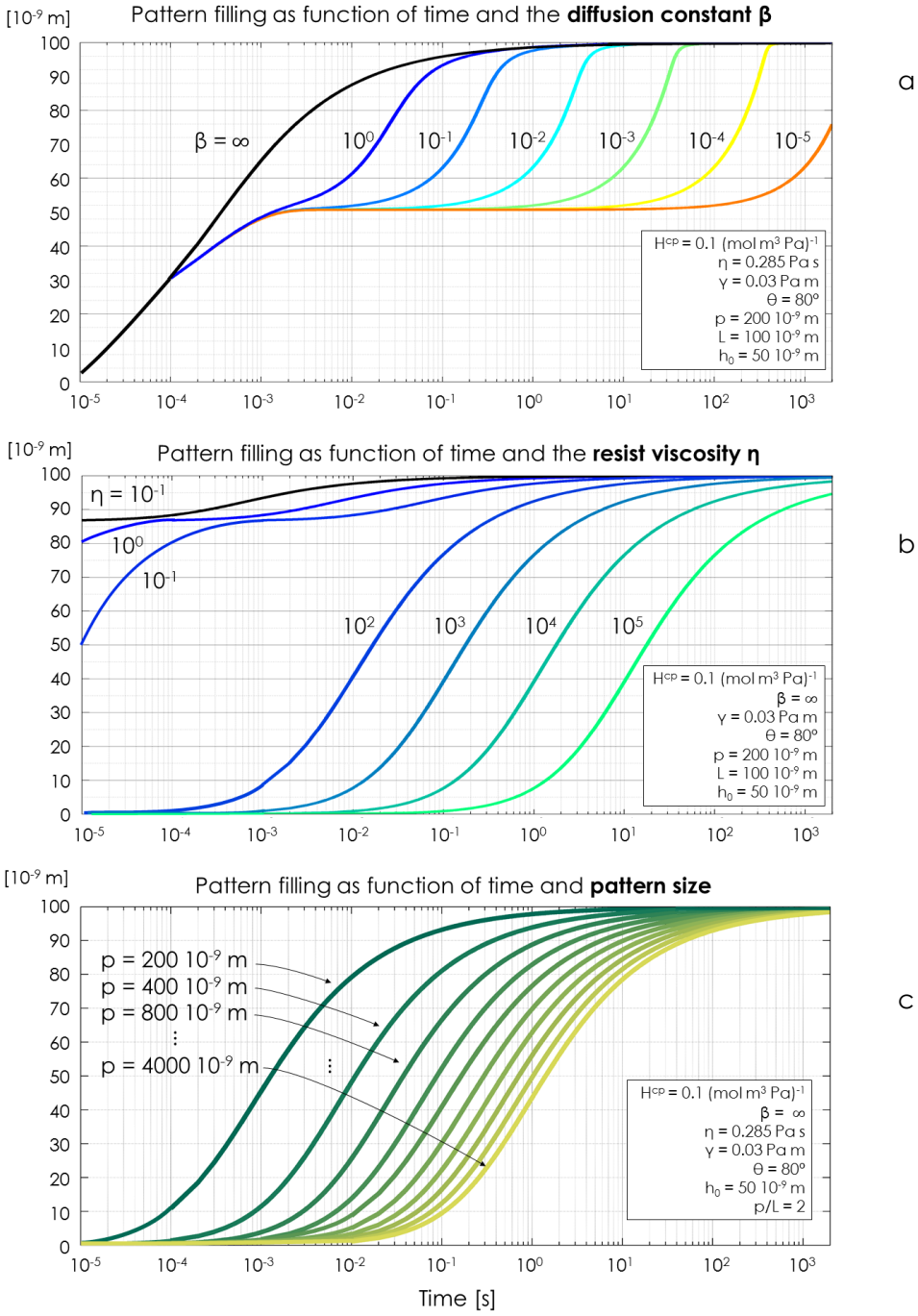

Figure 7 – Evolution of capillary rise and filling in SR-NIL as function of time for different values of diffusivity of the air into the resist (**a**), resist viscosity (**b**) and features sizes (**c**).

Fig. 7b shows the dependence of the filling time from the resist viscosity, given the same pattern dimensions as in Fig. 7a and an instantaneous diffusion of the trapped gases into the polymer. The plot shows that an increase in viscosity by one order of magnitude results approximately in an increase of the filling time also by one order of magnitude. Figure 7c shows the time evolution of the capillary rise for different feature sizes. While only fractions of a second are needed to fill a grating with pitch 200 nm and a 50% duty cycle, this time can go up to thousands of seconds if the pitch becomes 4 μm, being all the other parameters the same. The increase in filling time due to bigger pattern sizes is exponential. This insight is very important for the imprint of the holographic spectrometer, where the feature size varies a lot across the imprinted die (see paragraph III.4).
Other than the cases plotted in Figure 7, the imprint dynamics can be also calculated as function of the initial resist thickness, different resist and gases composition, contact angle and mold functionalization, etc. In spite of the insights that the model provides, it may not encompass the complexity of the seemingly simple phenomenon in question. For example, having ignored the actual profile of the meniscus inside the grating is quite a substantial approximation. In fact, when the rise is close to completion, the higher level of the meniscus touches the upper-inside surface of the mold trench. This causes the Laplace pressure to increase and drag the resist upward more vigorously. Then a lateral filling along the trench occurs, which is similar to the case of J-FIL. This mechanism can be more dominant than one might expect and it accelerates the filling compared to what the model predicts. It is not a deterministic effect since it can happen in proximity of small irregularities inside the mold protrusions. This is why a more complete analytical model of SR-NIL would be pointless. To the best of our knowledge, the simple model derived here provides the most complete description of the filling mechanism during SR-NIL.

II.4 State of the art and technology prospect

Most of the NIL techniques, such as SR-NIL on pre-spincoated film, R-NIL, resist free NIL, and CNP are suitable for university lab research and prototyping, but have hardly been considered by the industry for high volume manufacturing (HVM). NIL proved suitable for several applications (see paragraph II.1). Despite all of the successes and remarkable results that NIL has achieved in laboratories, the technology has not yet delivered the great promise to enter the semiconductor market. IC industry is the larger market for nanolithography and was the main motive that drove a fairly big amount of investments to NIL in the first place. The most attractive features that make NIL interesting to the semiconductor industry are the high patterning resolutions and low cost of ownership (COO). The International Technology Roadmap for Semiconductor[118] (ITRS) listed NIL as a potential candidate starting at the 22 nm node (80 nm pitch), and NIL has in fact demonstrated even higher resolution capabilities. “By making things smaller, everything gets better simultaneously” (G. Moore).[119] Moore’s law started as an

observation of the IC integration trend, and it has turned into a benchmark for the semiconductor industry. Compliance with Moore's Law is certainly what sustains the exponential growth in the IC market.[120] Resolution is the underlying propeller of this market, but optical lithography presents fundamentally insurmountable resolution limits. Smaller nodes are currently achieved by double and quadruple patterning techniques, which caused the cost of IC production plants to peak. As far as resolution is concerned, NIL does not suffer from fundamental limitations as opposed to photolithography. John Roger's group in 2004 shows the replication of a single walled carbon nanotube by NIL and establishes the current record for sub-3 nm imprint[121]. Stephen Chou in 2005 shows a method to fabricate NIL template with 4 nm half-pitch (HP) gratings and demonstrates that lines down to 6 nm HP can be replicated by NIL into a polymer[122]. In 2012, the imprint of a sub-5 nm HP L-shaped grating, fabricated by HIM, is attained[98]. Imprint and transfer into Si by SR-NIL on pre-spin coated film of sub-8 nm lines as well as sub-15 nm metal patterns have been demonstrated by our group recently[99,123]. Another advantage of NIL for HVM is a COO about 41% lower than that of current ArF immersion lithography systems that employ self-align quadruple patterning[124].

While both resolution and COO of NIL outperform the most advanced photolithography tools, there other criteria to factor in to have a complete overview of the state of the art. In fact, we can look at how far NIL is from applications in the semiconductor industry, as this is the field that sets the strictest technology requirements for a new lithography technique. Among all of NIL systems, the J-FIL steppers by Canon Nanotechnology Inc. (CNT) are some of the best tools currently being developed to tackle applications in microelectronics and memories.[124] In February 2014, Canon announced the acquisition of the semiconductor division of MII and the formation of a wholly owned subsidiary, CNT. CNT's goal is to meet the requirements of the semiconductor industry by fabricating the most advanced tools for NIL. This is why a close look at J-FIL and CNT comes close to fully describe the state of the art of NIL.

According to the ITRS guidelines, lithographic processes in the semiconductor industry must meet stringent requirements on defectivity, overlay, throughput, critical dimension uniformity (CDU), line width roughness (LWR), and other metrics. Defectivity is perhaps the most critical issue of NIL[125]. Other than defects which are common to all lithographic techniques – such as line breaks, collapses, bridges, and mouse bites – non-fill and adhesion failure are specific to NIL. Defects originate from templates, processes, materials and wafers. Figure 8 graphs the improvements in defectivity operated by CNT[†] in the last 3 years.[126] In October 2015, at the Nanoimprint and Nanoprint Technology (NNT) conference, CNT demonstrated the current state-of-the-art for the defectivity in J-FIL[127], which is now as low as 4 defects per cm^2. Particle contamination is a serious concern in NIL since particle-related defects may affect both the imprinted die and the mold, and

[†]Although authors in the proceeding are affiliated to Canon, the paper was issued only a few months after the acquisition of MII was completed. So, outcomes and historical data shown in the paper have to be considered as a result of the authors work in the former MII.

can propagate to all subsequent fields. Owing to the implementation of a complete and partial air-flow control system inside the template head, Canon enabled a reduction in the number of particles by 50 times in their new pilot line tool FPA-1100 NZ2 (Figure 9).[127] An astonishing three-order of magnitude improvement in the defectivity was achieved in barely 4 years thanks to the availability of low-defect imprint mold at 26-nm half-pitch.[128] Yet, these numbers are still far from the 0.01 defect/cm^2 that is required for the current and future nodes in the semiconductor industry.[118] This is why applications in the field of data storage and memory seem more realistic in the near future.[129]

Semiconductor and memory devices are very different in terms of processes and requirements. Semiconductor devices consist of many layers, each having a different geometry and specifications, and requiring precise overlay. Due to their built-in redundancy, bit-patterned media (BPM), NAND flash memory, and DRAM devices have much more relaxed requirements on defectivity. For instance, Toshiba has stated that a defect density $<$0.1 defect/cm^2 is sufficient for memory applications.[130] At the same time, memory devices aim at a denser bit integration (i.e. a higher spatial resolution). This makes NIL a perfect candidate for the fabrication of memory devices. The production of BPM hard disk drive (HDD) devices by NIL was expected by the 2011, but the heat-assisted magnetic recording has temporarily delayed the introduction of BPM-HDD. Major companies actively working on the implementation of NIL for memory applications are Samsung[125], Toshiba[130], CNT[124] (former MII), and Seagate[131].

As defectivity is still about one order of magnitude higher than the requirement for memory, the second most crucial specification to refine in imprint is throughput. The primary limiting factor of throughput in J-FIL is the resist fill-time. In 2014 MII demonstrated that the non-fill defect density in J-FIL is inversely proportional to the total fill-time of the dispensed resist.[126] A density of non-fill defects as low as 0.1/cm^2 was achieved with a spread time greater than 1 second. Since there seem to be an inverse correlation between defectivity and throughput, a trade-of must be found. Both resist fill-time and density of defects have been shown to decrease with the diameter of dispensed droplets.[132] This is the route that CNT is undertaking to solve the defectivity/throughput puzzle: newer imprinter models are equipped with a sub-1 pL droplet dispensers.[126] To achieve a throughput of 20 wafers per hour (300 mm in diameter), fill-time must be kept under 1 second. Other processing steps like mold release and UV exposure last as little as 0.1 sec. Reported state of the art for throughput in NIL is 10 wafers/hour per imprint station (Figure 9).[127] Typical values of throughput are on the order of 100 to 200 wafers/hour in the semiconductor industry, and 1000 double disks/hour are expected in the BPM industry.[125] Clustering of stations is a straightforward way to meet throughput requirement and low the COO. A state-of-the-art 4-module imprint station by CNT provides an overall throughput of 40 wafers/hour, but CNT's expected target by 2018 is 80 wafers/hour.[127] Other specifications such as overlay, CDU, and LWR have already surpassed or are very close to the ITRS requirements. J-FIL produces low CDU and LWR very consistently.

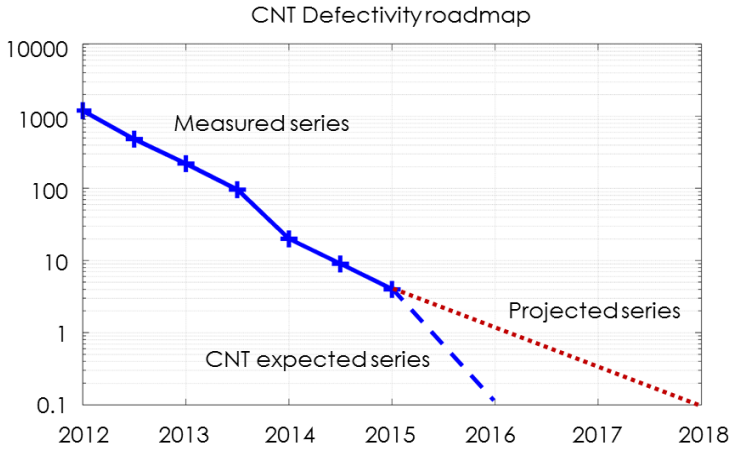

Figure 8 – Trend of improved defectivity in MII-CNT NIL tools and future progress expected by CNT. The projected series is based instead on a simple geometrical projection of the precedent trend.

A CDU of just 1.2 nm (3σ) for grating with a pitch of 56 nm was achieved across a 300 mm wafer, which surpasses by a factor of 2 the ITRS requirement of 2.3 nm.[130] LWR of around 2 nm has been reported by different sources and is only slightly above the requirement for 22-nm flash memory.[125] As for the overlay, historically lithography tools use Moiré interference patterns to align subsequent layers. J-FIL uses the same approach but mechanics and electronics of the template placement must be very well engineered to maintain a nanometer-level accuracy in the placement even after physical contact. By improving the systems responsible for this mechanical process in CNT tools, the overlay accuracy decreased by a factor of 8 only two years and is now about 4.5 nm (3σ).[124] This is only about 1.4 times worse than the requirement of 3 nm indicated by ITRS for nodes smaller than 22 nm. All these results are obtained as averages over different lots of wafers (one lot equals 25 wafers), with one mold being used to imprint over 1000 wafers. The mold used in J-FIL is replicated from a master as described in paragraph II.2. This helps preserving the cleanness and integrity of the expensive master-template and reduce the mastering cost in production.

The obstacles on the road to the semiconductor industry do not end with just defectivity and throughput. A less advertised challenge of NIL is the residual layer.[133] Residual layer removal is an extra step in the fabrication process that increases the fabrication costs and affects the feature size. Solutions have been proposed for a residual layer-free imprint,[134] but no proof has ever been provided that these techniques can actually be applied to a HVM process without affecting the defectivity. Finally, a big concern of NIL is the inspection capability of templates. NIL is a 1× contact lithography, so frequent inspections of templates in production is expected. This is not a simple task to carry "on-the-fly" on nanometer-size features. E-beam reticle/template inspection capability cannot detect defects that are up to 10% smaller than the minimum feature size on the template, as required by ITRS.[125] This results in very expensive e-beam inspection tools, such as the Hermes Microvision eXplorer5200, which uses a 10 nm pixel size and showed a

reliable detection of 22 and 30 nm clear and opaque defects respectively, on a 28 nm HP grating.[135] An inspection by such tools can account for up to 8 days of uninterrupted scanning onto a full-field NIL template (26×33 mm). The use of much faster scatterometry techniques instead of ebeam inspection tools in the HDD industry is enabled by the consistent periodicity of the patterns. These techniques are unable to pinpoint tiny defects. But due to a lower requirement on defectivity, the detection of particles, larger defects, and other anomalies is probably sufficient for the purposes of the memory industry.
Although efforts and investments are being carried to reach the required specifications in the semiconductor industry, NIL is ready for manufacturing photonic devices. The next paragraph merges the topics that were discussed in the first two chapters of this thesis and explains why the application of NIL to photonics can enable the easy fabrication of novel photonic devices with a high reliability, resolution and a low cost.

Figure 9 – New generation Canon FPA-1100 NZ2 imprint tool for HVM.

II.5 NIL: an enabling technology for photonics

Most of the photonic applications that are listed in paragraph I.3 rely on the availability of novel and more powerful micro and nanofabrication capabilities. Unlike electronic ICs, where a large market is served by a handful of integration technologies (mostly CMOS), the broad range of applications of photonics require more flexibility in the fabrication. This originates from the lack of one fundamental building block, similar to the transistor in electronics, and the unfeasibility to converge to one material. Different materials like InP, $LiNbO_3$, GaAs, SiO_2, Si, Si_3N_4, TiO_2, and others are needed for different devices and wavelengths of operation. The absence of device standards also makes economy-to-scale benefits very hard to

achieve in PIC manufacturing. This leads to a situation where different companies in the field of photonics are forced to develop their own fabrication processes and devices independently, generating even more differentiation. As an attempt to contain this phenomenon, in 2004 a large number of European academic and industrial members founded the European network of excellence on Photonic Integrated Components and Circuits (ePIXnet).[136] The mission of ePIXnet is to move from an independent to a more integrated research model with a shared use of expensive infrastructure. However, convergence to standards by itself is not enough to drive down costs.[137] Even though most of the established fabrication processes and expertise in the semiconductor industry can be reclaimed for photonics, today the cost of a new CMOS fabrication facility can be as high as several billions of dollars. This makes competition for HVM of PICs very cost prohibitive, and provides a very small return on investment. These issues suggest that a collateral technology must be found that can support the advancement of photonics towards the market and beyond. This technology should be very versatile and suitable for as many photonic structures and platforms as possible, allow research, prototyping, and manufacturing all together in a very cost-effective manner. We think that NIL can be such technology and the perfect candidate for photonics.

An overview of the state of the art of NIL was presented in the previous paragraph. The level of technology maturity of NIL does not enable imprintable ICs yet, but it certainly surpasses the requirements for photonics. With different degrees depending on the application and geometry, photonic devices are much more defect tolerant. Bubble and non-fill defects are perhaps the worse type of defects in NIL that can kill the functioning of electronic devices. Numerical studies show that if a non-fill defect is present in a waveguide, light can still propagate with an efficiency that is slightly or moderately lowered depending on the size of the defect.[138] The lithography resolution that is needed to fabricate optical metamaterials, PhCs, resonators, and plasmonic devices for visible and near-infrared (NIR) light is achievable at a low cost by NIL. Requirements of photonic devices such as edge smoothness and good CDU have been already proved possible by NIL.[99,139] Other than technology maturity, NIL carries some intrinsic advantages for photonics compared to other lithography techniques. For instance, the capability to pattern any regular or irregular substrate is a conspicuous benefit of NIL for photonics. The broad material compatibility and possibility to fabricate 3D structures in a single step are other excellent features that enable the inexpensive fabrication of many photonic devices. NIL is also a very convenient option in almost all of the stages of a technology development, from testing, prototyping to manufacturing, for both R&D and production.[139] Not only NIL meets all requirements for photonics but it outperforms all other lithography techniques for flexibility, resolution, compatibility and cost-effectiveness.

Many photonic devices and applications have already been demonstrated by NIL. Due to its scalability, NIL is increasingly becoming the preferred lithography tool to fabricate structures that aim at enhancing photovoltaic device performance.[140] Sub-wavelength high contrast diffraction gratings have been fabricated by NIL for

solar energy harvesting and solar-electricity conversion systems that are based on light spectrum-splitting.[141,142] NIL techniques have been already tested for patterning substrate, electrodes, hole-injection layer and photoactive layer of photovoltaic cells with enhancements in efficiency that can reach 660%.[143] R2R-NIL and R2P-NIL are probably the most attractive techniques for photonic applications that require large coverage and that are more defect-tolerant (i.e. solar cell).[144] In both UV and thermal R2R, R2P NIL, a series of rollers pattern a moving plastic film or plate, which was pre-coated with UV-resist or that is embossed by high pressure and temperature. A fabrication speed faster than 1 m/min can be achieved with this technology, which ensures low production costs and increases the competitiveness of photonic devices. R2R-NIL is currently employed in semi-industrial production[140] and a $ 25M facility is expected to open this year at the University of Massachusetts Amherst for advanced roll to roll fabrication and processing.[145] Using similar photonic structures to those patterned by roller NIL onto solar cells, the internal reflection of LEDs and OLEDs can be lowered. This enhances the light extraction and performance of light emitting devices. OLEDs patterned with certain nanoimprinted geometries have demonstrated a twofold increase in the out-coupling.[146] NIL has also been employed to fabricate lasers based on PhCs, as well as 1D, and 2D grating. One of the first example of imprinted laser was demonstrated by John Rogers in 1998.[147] A Bragg reflector was imprinted into a polymer and coated with 2-(4-biphenyl)-5-(4-tert-butylphenyl)-1,3,4-oxadiazole doped with 1 wt% of Coumarin 490. Lasing was obtained in the red range with a lasing threshold of 7kW/cm^2. An even more powerful approach is to embed the gain medium into a functional resist and fabricate a laser through a single-step imprint process. In 2007, Rebound *et al* demonstrated the single-step fabrication of a PhC band-edge laser, which was achieved by direct imprint of mr-NL6000 doped with rhodamine 6G.[148] Several other types of distributed feedback laser diodes were also attained by NIL.[93] PIC components such as waveguides, ring resonators, splitters, holograms, gratings and numerous other planar photonic devices have been already demonstrated by imprint of polymers, high RI dielectrics, and chalcogenide glasses.[149-153] Many examples of imprinted optical metamaterials and plasmonic structures are present in the literature. Negative RI metamaterials working in the mid and near IR were fabricated by NIL with gold (Au) and a stack of silver/Si2O/silver respectively.[154] NIL is particularly suited for the fabrication of plasmonic structures, which require high resolution and very low roughness. Nano-cones in different metals with a sub-10 nm tip were achieved by NIL for surface enhanced Raman spectroscopy (SERS) and sensing applications.[155] Other plasmonic structures fabricated by nanoimprint include plasmonic crystals[156], custom-shaped nanoparticles[157], V-groove waveguides[158], 3D resonant cavity antennas[159], and several others.[160-162] A very active area of research is also imprintable plasmonic structures for biosensing and medical applications.[163-165] Finally, the flexibility and material compatibility of NIL allow unconventional applications such as patterning optical fiber facets for SERS sensing, fiber-to-PIC coupling, and on-wafer optical probing.[166,167]

The above overview covers just a fragment of the field of printable photonics and shows the advantages that the application of NIL to photonics can yield. The

scientific and industrial communities also agree that NIL is one of the most viable options for photonics. EVG has recently announced a new imprint tool that combines pre-processing steps and imprint inside a single platform, claiming "industry-leading productivity and throughput".[168] With this new tool, the company is targeting the photonics market.[169] Although the majority of the applications that are described in the review above rely on basic NIL processes, future 3D photonic structures will require cutting-edge NIL capabilities. In fact, 3D structures should be fabricated with the higher possible overlay accuracy between consecutive layers to minimize light phase mismatch. US Government agencies, such as Department of Defense, also have issued solicitations specifically for the precise fabrication of integrated photonic devices using low-cost nanoimprint processes.[170] Above all, 20+ years of successful research in the field of printable photonics prove irrefutably the feasibility and convenience of this approach.
In the following chapter the fabrication of an integrated holographic spectrometer is demonstrated by SR-NIL. This device was chosen for its widespread use in the field of integrated optics, the potential for sensing, and the variety of optical components that integrates monolithically. Our goal is to demonstrate that reliable fabrication, testing, and prototyping of complex photonic devices is possible by nanoimprint.

III. Digital Holographic spectrometer fabricated using SR-NIL

III.1 Overview of the DPH spectrometer

Spectrometers are used in a variety of applications, ranging from biomedicine, material characterization to product quality control.[171] Dispersive optical elements such as prisms or diffraction gratings are the core components of spectrometers. Traditional spectrometers work in free space: light is coupled in through an optical fiber or a slit, hits the dispersive/diffractive element and is finally projected onto a detector by a series of reflections. Due to the long optical path these spectrometers can have ultrahigh resolution over a broad spectral range, but their applicability is limited by the portability and high cost. While the ICs of the readout can be very compact, the free-space optical components cannot be shrunk without an exponential decrement of the performance. To date, this represents the bottleneck to the very beneficial integration of spectrometers into portable photonic sensors and lab-on-a-chip, such as optofluidic devices,[172-174] micro and nanoelectromechanical systems.[175] Since the advent of PICs, the potential for integrated spectrometers has become a reality and numerous designs of compact spectrometers have been proposed over the last few years. Although miniaturization of spectrometers was demonstrated down to the micrometer scale, the direct proportionality between device footprint and performance still hold. It is hard to combine both high resolution and large spectral range in PICs, so as a spectrometer becomes smaller, a decrement in one of these two factors occurs, similarly to what happens in free-space spectrometers.[176-179] High resolution spectrometers have been fabricated based on microresonators shaped like rings,[180] disks,[181] and donuts.[182] The quality factor (Q-factor) of the resonating structure determines the resolution of the spectrometer. Interferometer-based devices such as spiral waveguides,[183] Mach–Zender,[184] and arrayed-waveguide gratings can also reach very high resolution.[185,186] However, the spectral range of resonator- and interferometer-based spectrometers is constrained by the number of output waveguides, which prevent broadband spectroscopy. Planar diffraction gratings[187] and echelle gratings[188,189] can also provide high resolution in a relatively wide working range. But resolution is directly proportional to the optical path of the light just like in free-space optics. This means that either

the portability of the resolution must be sacrificed. Spectrometers based on PhCs,[190,191] MEMS,[192] and arrays of Fabry–Perot cavities[193] are capable of broadband spectroscopy but exhibit a poor resolution. Moreover, all of the approaches listed above is not sufficiently resilient to fabrication errors. This problem inspired the development a more defect-tolerant, high-resolution spectrometer, which is based on disordered scattering media.[177] Light is coupled into a waveguide and reaches a media full with random subwavelength holes that scatter different wavelengths to different outputs. Intensities are recorded at the outputs and a computer algorithm is used to reconstruct the original spectrum. This spectrometer can be very compact and defect-tolerant. Unfortunately, this solution is not very flexible and only works for a narrow wavelength range.

In order to overcome the limitations of integrated spectrometers, we have designed a miniaturized spectrometer that is based on digital planar holography (DPH). DPH technology is type of computer-generated hologram (CGH)[194] and can encode almost any optical transfer function on the plane by manipulating the light in both the spectral and spatial domains. In CGH, the interference patterns formed by the interaction of an object beam and a reference beam is computationally calculated. This enables the use of volumetric holography to reconstruct complicated 3D wavefronts without the need to use any physical object. A slice of a volumetric hologram is a planar hologram, therefore a DPH can be understood as a CGH in two dimensions (detailed DPH theory in paragraph III.2). DPH technology is fundamentally flexible and customizable. Wavelength demultiplexing is just one of the numerous classes of applications that DPH can handle. Compared to competing technologies for integrated spectroscopy, DPH provides decisive advantages such as resiliency to fabrication errors, high resolution, and a large range of operation. Unlike conventional diffraction gratings where light diffracts in a continuous spectrum, digital holograms can be designed to split and focus different wavelengths into a sequence of focal points, increasing the efficiency of the spectrometer and the potential for compactness.

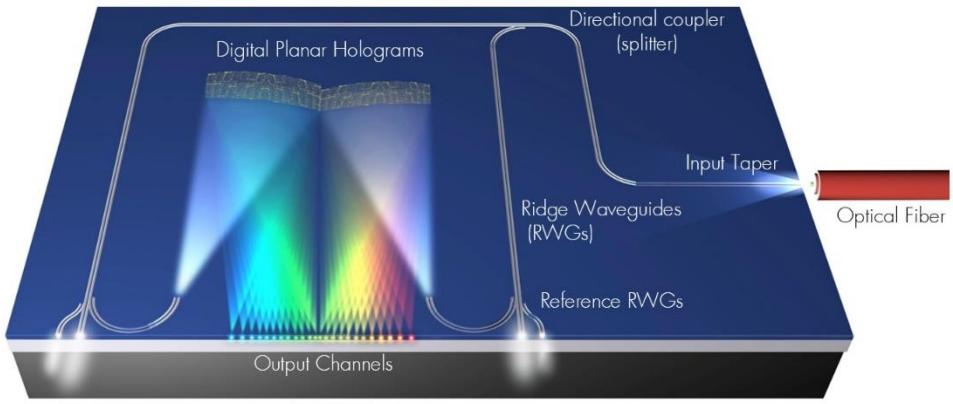

Figure 10 – Drawing of the on-chip spectrometer based on DPH technology. The photonic device integrates a RWG circuit with directional couplers, an input taper and TE-polarizers.

DPH spectrometers have already been fabricated into planar waveguides with different materials, such as SiO_2Ge_x, HfO_2 and Si_3N_4 for applications of light demultiplexing in the visible range.[195-199] Over the last years, DPH demonstrated spectral resolutions down to 0.015 nm in a narrow spectral range (1 nm).[200] Other versions of DPH have been designed to cover multiple separate bands (up to 4), demonstrating the outstanding flexibility of the technology.[197] In all these works, the fabrication of the DPH was performed by EBL and etching and was limited to the mere DPH component only. One paper reported the fabrication DPH by SR-NIL, but the imprint was also limited to a single isolated hologram (2.8×1.3 mm^2).[150] A single DPH has a spectral range that is limited to about 90 nm, so only narrow band spectroscopy can be achieved. To overcome these problems, we designed a PIC that potentially integrates multiple DPHs working on different spectral ranges and that is connected by an optical circuit (Figure 10). The circuit comprises an input taper, a ridge waveguide (RWG) spanning several centimeters, multiple directional couplers, and DPHs. The light is coupled from an optical fiber in the integrated circuit through the input taper. The purpose of the taper is to match the fiber mode with the RWG mode. The overlap of these modes corresponds to the maximum coupling efficiency at the input. The transverse magnetic (TM) polarization is decoupled from the circuit by having a shallow etched RWG. This allows only the transverse electric (TE) polarization to propagate in the RWG and forces the TM polarized light to leak. Polarizers are required since the DPH has different responses for different polarizations. A directional coupler is inserted in the optical circuit that splits light into two separate bands centered with the DPH spectral ranges. The RWGs end points toward the DPH: light exits the RWGs and propagates in the planar waveguide only confined in the vertical direction (Figure 10). The beam aperture in the "free propagation" region is dictated by the wavelength and the waveguide geometry. The Gaussian beams illuminate the hologram, whose encoded function works by focusing different wavelengths into spatially separated foci. The foci corresponds to output channels and are located at the edge of the chip. A photodetector array is integrated at the outputs for the electronic readout. We designed the device in Figure 10 to enable high resolution over a broad band in a very compact spectrometer. The design considered here works over two separate spectral bands (630–694 nm and 766–850 nm), which yield a total bandwidth of 148 nm, with 0.15 nm resolution and 926 output channels.

The device occupies an area of about 15 by 20 mm, which is a tiny footprint considering the amount of integrated functionalities for spectroscopy. At the same time, this is a fairly large area to fabricate by NIL, and it is full of complex optical components. The design depicted in Figure 10 carries many technology challenges for NIL. The theoretical understanding of SR-NIL on pre-spincoated film reported in Chapter II, can help us assess the potential issues in the fabrication of this device. The different pattern dimensions of DPHs and RWGs – spanning 60 nm to >5 μm in feature size, over several millimeters – may result in different filling times and residual layer variation. The RWG cannot have any major defect along its extension. Bubble trapping and other types of non-fill defects can cause irregularities in the RWGs that can compromise the propagation of light. In Chapter II we also covered

the issues about LWR at high resolution in lithography. This is a very important point in case of PICs like the one in question, since LWR would generate propagation losses and light scattering. Another challenge lays in the "free propagation" region. This area does not contain features but a defect in this area would cause light scattering or incorrect illumination of the DPH. Failure to achieve any of the mentioned challenges directly impacts the fabrication yield. This is why we consider this device as the optimal testbed to probe the capabilities of NIL for the fabrication of photonic devices. Statics about the fabrication yield measured after imprint and optical testing are reported. The full characterization of the fabrication process and optical evaluation of the integrated device as a wavelength demultiplexer and spectrometer are discussed in the paragraphs below.

III.2 Theory of Digital Planar Holography

III.2.1 Distributed Bragg Reflector

A distributed Bragg reflector (DBR) is a wavelength selective mirror that can be integrated in waveguides and optical fibers. It consists of a number (N) of pairs of layer that exhibit different refractive indexes (Fig. 11). A DGR is a resonating structure where part of the light is reflected backward at each interface. Wavelengths that are reflected in phase to each other propagate backward ($\mathcal{R}_N$), while all others propagate forward ($\mathcal{T}_N$) yielding a selective mirror. A DPH spectrometer can be physically understood as a superposition of several elliptical Bragg reflectors. DBRs are well-known and popular in photonics. However, a review of the fundamental mathematics of DBR will provide important clues about the functioning of the more complicated DPH design. Approximated formulas of the frequency response and reflectivity of the DBR can be calculated with simple assumptions by ray tracing, but approaches such as the reflection coefficient method[201] and matrix optics[202] can give an exact solution to the problem. The mathematical formulation that is reported in Appendix B is based partially on the textbook of B.E.A Saleh and M.C. Teich[203] and uses matrix manipulation. We will consider the specific and simpler case of light travelling perpendicularly to the interfaces. So polarization can be disregarded.
The DBR considered here has $d_1 = d_2 = 100$ nm, and a RI contrast $\Delta n = 0.5$, with $n_1 = 1.5$ and $n_2 = 2$, i.e. similar to SiO_2 and Si_3N_4 (or TiO_2) respectively. Giving these parameters, the Bragg frequency of the DBG is $\nu_B = 428.3$ THz, which corresponds to a Bragg wavelength in the vacuum $\lambda_B = 700$ nm. Combining eq. (33) to (40) in Appendix B, the $\mathcal{R}_N(\nu)$, is attained in a closed form and plotted in Figure 12a. The graph shows an increment of the reflectance as the number of layers (N) increases, due to the presence of more interfaces where light can reflect backward. We find periodic resonances at every n-th harmonic of the Bragg wavelength with a number of side lobes that also depends on N. A good selective mirror for high-resolution spectroscopy should have a narrow spectral reflection.

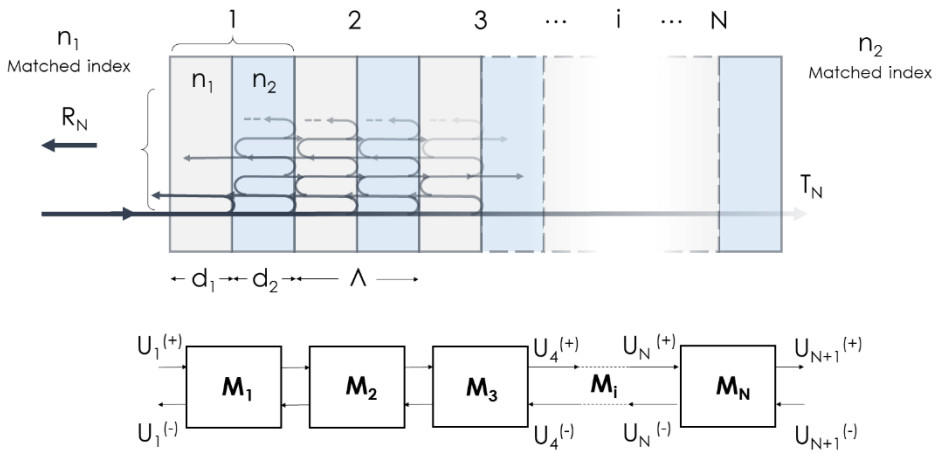

Figure 11 – Schematic representation of a DBR as a sequence of pairs of layers with different refractive indexes (above). The matrix optics model of a DBR is a series of wave transfer matrices, where each block embeds the phase information of a pair of layers (below).

The increase in the number of pairs improves the efficiency of the grating but only marginally improves the spectral response. Figure 12b plots the reflectance as a function of the index contrast for N=50. From Fresnel equations we already know that a lower contrast results in lower reflectance, but here we also see a narrowing of the reflected band. So, a small index contrast induces a gain in resolution. Figure 12c and d show the change in reflectance and full width half maximum (FWHM) of the main lobe as function of the index contrast for different values of N. A high N can make up for the loss in efficiency given by a small Δn and still provide good performance in terms narrow wavelength selection.
Another well-known means to increase the resolution of a DBR is tuning the layer widths d_1 and d_2 such that the wavelength of interest is the k-th harmonic of λ_B. This also can be seen as selecting a different order of the grating. From (40) in Appendix B we have that

$$k\lambda_B = 2n\Lambda = 2n_1 d_1 + 2n_2 d_2 \tag{4}$$

So d_1 and d_2 can be wider such that the first harmonic is k times longer than that of interest. This results in a narrowing of the peak at λ_B like Figure 12e shows. The drawback of selecting another grating order is the presence of more spectral resonances. This is important when using DBRs for broadband spectroscopy: selecting a higher order improves spectral resolution but constrains the range. Finally, regardless of how narrow we design the main lobe, the presence of side lobes in the spectrometer would decrease signal to noise ratio (SNR), induce crass-talk in adjacent spectral channels and force them further apart from each other. Apodization is a simple tool that can be introduced in the design to attenuate the side lobes. It consists of a gradual increase of the index contrast from 0 to Δn and

back to 0 across the grating in the direction of illumination. Appendix B reports the calculation of $\mathcal{R}_N$ when a raise-cosine is used as an apodizing function. Then the combination of (31), (42), and (43) provide the overall reflectance $\mathcal{R}_N$ as function of the apodization factor. Figure 12g shows how an increase in the apodization factor results in a more efficient side lobe suppression, enabling higher SNR at no extra costs. All of these considerations are very useful to understand the fundamental physics behind DPH and will be often recalled in the next paragraphs.

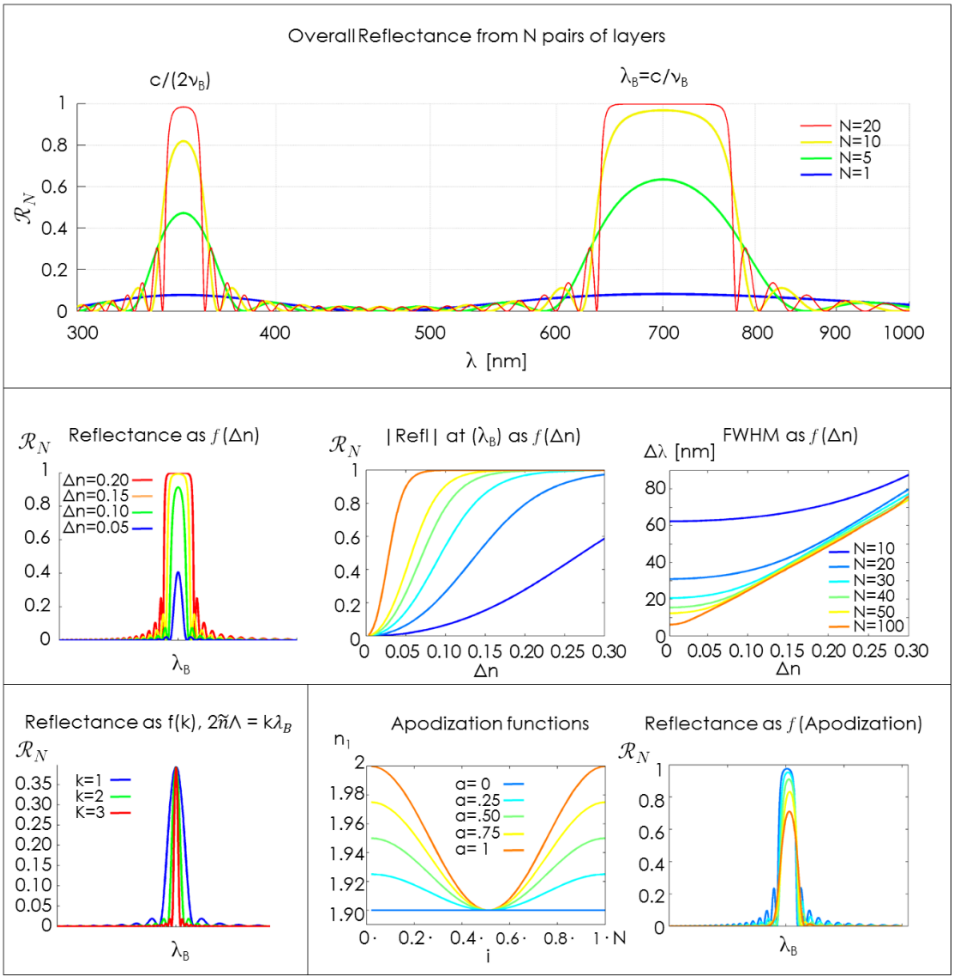

Figure 12 – Reflected waves from a DBR as function of various parameters. **a**. Typical spectral response of a DBR. In this first graph, the response is plotted as function of the number of layers (N). **b**. Spectral response of a DBR as function of the RI contrast **c**. Change in efficiency of the grating as function of RI contrast and number of pairs. **d**. Change in spectral resolution of the grating as function of RI contrast and number of pairs. **e**. Effect of the grating order on the increase in spectral resolution and side-lobe suppression. **f**. Apodization functions to smooth RI profile across the DBR and (**g**) change in spectral response due to the use of apodization functions.

III.2.2 Digital Planar Holography

Holography is a technique that enables recording and reconstruction of lightwaves. A hologram is obtained by "encoding" the interference pattern between an object wave and a reference wave into a medium (Fig. 13a). Depending on the encoding process, we distinguish between absorption and phase holograms. The former encode the interference as a modulation of the transmittance of a transparency, while the latter convert interference into a variable thickness of the medium that introduces a phase shift as the reference wave passes through it. In both cases, the subsequent illumination of the hologram by the same reference beam will cause light to interfere and reconstruct the original object wave (Fig. 13b).
Holography mathematics was proposed by Dennis Gabor in 1948 to improve the resolution of electron microscopes.[204]

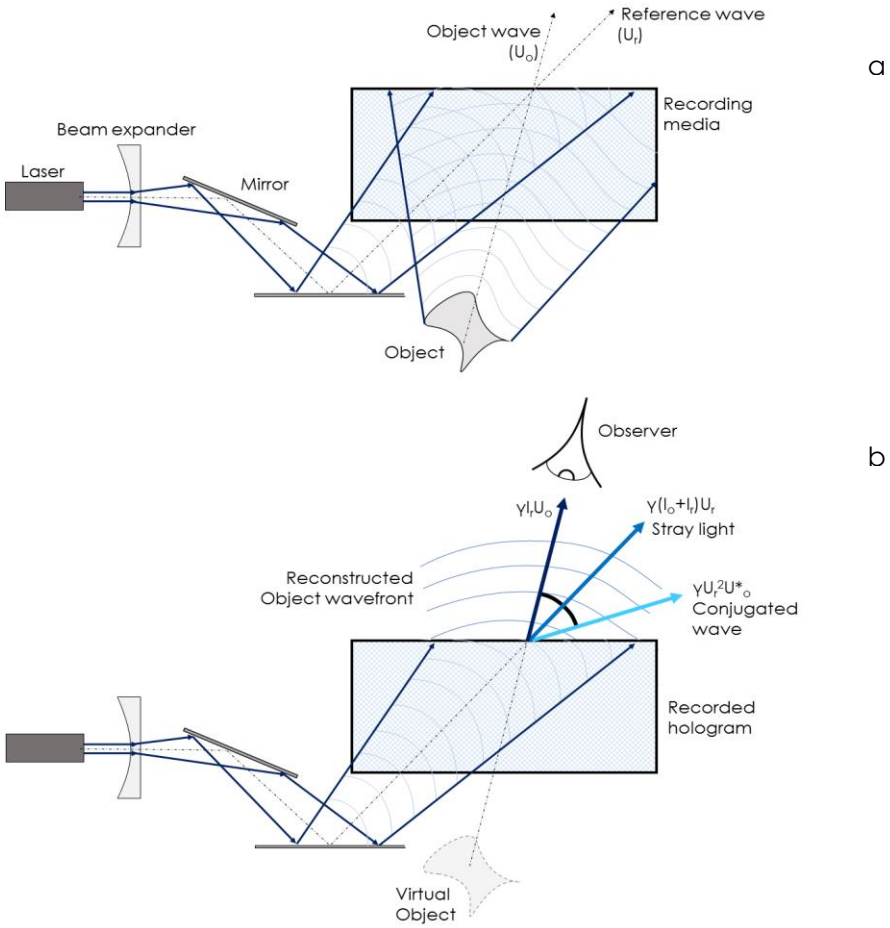

Figure 13 – Working principle of holography. **a**. Recording of the phase information from an object wave inside a medium through interference with a reference wave. **b**. Playback of the object wave by illuminating the medium with the same reference wave. Diffractive waves are also generated that differ from the original object wave.

The invention of lasers, about a decade later, allowed the actual implementation of holography. In 1964, Emmett Leith and Juris Upatnieks of the University of Michigan, demonstrated the first laser transmission hologram by reconstructing 3D objects.[205] Since the invention of computation, CGH have enabled calculation of complex interference pattern of volumetric holograms.
To mathematically describe holography, let $\boldsymbol{U} = \boldsymbol{E_0} e^{i\,\boldsymbol{k}\cdot\boldsymbol{r}+\varphi}$ be the time independent amplitude of an electric field vector $\boldsymbol{E}\ \boldsymbol{r},t$. The time averaged intensity of $\boldsymbol{E}\ \boldsymbol{r},t$ is $I = \langle \boldsymbol{E}\ \boldsymbol{r},t\ \cdot \boldsymbol{E}^*\ \boldsymbol{r},t\ \rangle = \boldsymbol{U}\cdot\boldsymbol{U}^*/\ 2Z$, where $Z = \sqrt{\mu/\varepsilon}$ is the intrinsic impedance of the medium. Thus, the interference pattern of a reference and object waves $\boldsymbol{E}_r$ and $\boldsymbol{E}_o$ respectively, can be calculated as follows:

$$I = \frac{1}{2Z}\ \boldsymbol{U}_r + \boldsymbol{U}_o\ \cdot\ \boldsymbol{U}_r + \boldsymbol{U}_o\ ^* = I_r + I_o + \frac{1}{2Z}(\boldsymbol{U}_o\cdot\boldsymbol{U}_r^* + \boldsymbol{U}_r\cdot\boldsymbol{U}_o^*) \tag{5}$$

If we model the transmittance t of a plate such that $t = \gamma I$ and we illuminate the plate with the playback wave $\boldsymbol{U}_r$, from (5) we have:

$$\widetilde{\boldsymbol{U}}_o = \gamma\ I_r + I_o\ \boldsymbol{U}_r + \gamma I_r \boldsymbol{U}_o + \gamma U_r^2 \boldsymbol{U}_o^* \tag{6}$$

The reconstructed wave $\widetilde{\boldsymbol{U}}_o$ consists of three terms. The first is a stray light component which follows along the direction of the playback beam $\boldsymbol{U}_r$. The second term is the object wave multiplied by a factor. The last term is the conjugated of the object wave. Figure 13b depicts equation (6) and the principle of holography. Equation (6) can be calculated exactly by means on the Fresnel integral and it describes the case of absorbance holograms. A more complicated demonstration is required for phase holograms, but a similar conclusion is ultimately derived. DPH applies the holographic principle to wavelength demultiplexing and belongs to the category of phase holograms. To design a hologram that encodes the working principle of the DPH spectrometer described in paragraph III.1, the interference pattern from the RWG input and all of the output channels must be computed[†††]:

$$I(x,y) \propto \int |E_{out}\ x,y,\omega\ + E_{in}\ x,y,\omega\ |^2 d\omega \tag{7}$$

We considered coupled waves into a planar waveguide, so in (7) the z-axis is omitted (Figure 14). E_{in} is the electric field of the light exiting the RWG, while E_{out} is the light that goes to the output channels. Let us split the spectral range of the integrated spectrometer (S) into a sequence of N adjacent channels with the same spectral width $\Delta\lambda$, each centered around the frequency ω_i and such that $N\Delta\lambda = S$. Then (7) can be approximated as follows:

[†††] In order to simplify the mathematics, we will do a qualitative study of the optics for DPH. The result will not be mathematically exact but it will retain the same physical meaning and it will allow us to comprehend the connections between the design parameters of a planar hologram.

$$I \propto \sum_{i=1}^{N} |E_{out}\ x,y,\omega_i\ + E_{in}\ x,y,\omega_i\ |^2 \tag{8}$$

To reconstruct $E_{out}\ x,y,\omega_i\ $, the RI of the phase hologram must be modulated like the interference pattern in (8), so $n\ x,y\ \propto I(x,y)$. We see that the more channels the DPH has, the more complicated $I(x,y)$ becomes, with multiple levels and a 3D envelope. To embed the continuous RI function $n\ x,y\ $ into a planar waveguide, a 3D fabrication approach would have to be used. This results in a very expensive and difficult mold fabrication – such as gray-scale EBL or gray-scale milling. 3D nanoimprint and multi-level etching should be also used. To allow a viable fabrication, the 3D envelope in (8) is binarized based on a proprietary algorithm, namely Spectroplan.[206]

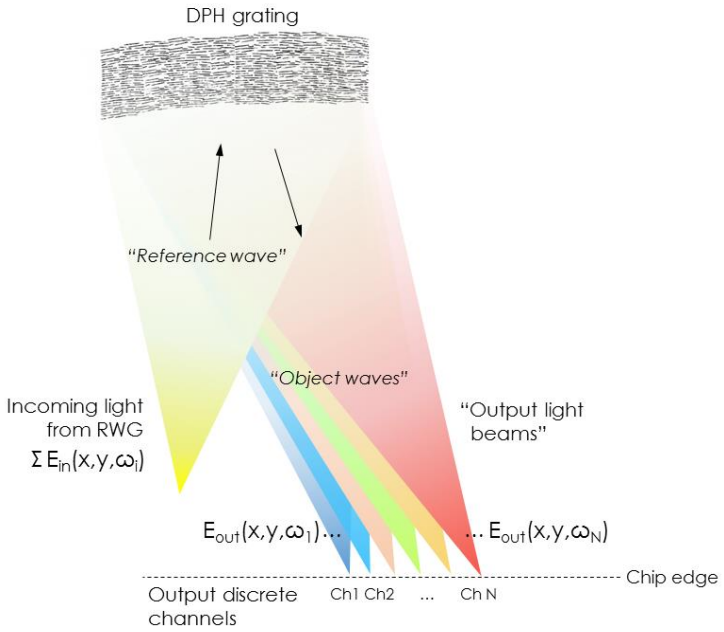

Figure 14 – Working principle of DPH technology. The drawing shows the geometrical location of the E fields that must interfere to generate a DPH wavelength-splitter. Note that this technology can be used to generate any other optical function on chip by choosing the desired distribution and phase of the electric fields.

Upon binarization, the RI assumes only two values. The binary variation of the RI is practically attained by etching the core of the planar waveguide. This enables a 2D fabrication of the original 3D hologram. The variation of the height due to etching is proportional to the binarized equation (8). The binarization process introduces spurious harmonics in the output that may severely compromise the functioning of the spectrometer. Spectroplan features an optimized binarization algorithm that minimizes this scattered light. However, to understand the mathematics at the basis of DPH, any arbitrary binarization rule can be considered with no loss of generality. For instance, let us use the following formula:

$$\Delta h_{bin} = \begin{cases} -h_0 \sigma(I\ x,y\ ) & if\ I\ x,y\ \leq \mu(I\ x,y\ ) \\ 0 & if\ I\ x,y\ > \mu(I\ x,y\ ) \end{cases} \tag{9}$$

where Δh_{bin} is the depth of the grating slits. $\Delta h_{bin}|_0 = 0$ is the 'zero' bit of the binary hologram, where the planar waveguide core is not etched, corresponding to areas of the DPH with a higher RI. $\Delta h_{bin}|_1 = -h_0 \sigma(I\ x,y\ )$ is negative to indicate that the waveguide core is etched down. This results in a lower local RI. The choice of the factor h_0 is arbitrary and can be based on the knowledge about the DBR reported in the previous paragraph (a formula to calculate h_0 is derived below). The average $\mu(I\ x,y\ )$ can be calculated approximating E_{in} and E_{out} as plane waves with unitary amplitude that propagate towards and away from the hologram respectively. Therefore, the time independent form of the input and output waves is $|E_{in}\ x,y,\omega_i\ | = \exp\left(-j(k_{ix}x + k_{iy}y)\right)$ and $|E_{out}\ x,y,\omega_i\ | = \exp\left(j(k_{ix}x + k_{iy}y)\right)$. The choice of opposite k vectors for equal frequencies does not reflect the actual working principle of the spectrometer (see Fig. 14), but it helps simplifying the calculations with no loss of generality:

$$\begin{aligned} \mu(I\ x,y\ ) = \frac{\iint I\ x,y\ dxdy}{\iint dxdy} \propto \frac{\iint \sum_{i=1}^{N} \mathrm{e}^{j(k_{ix}x+k_{iy}y)} + \mathrm{e}^{-j(k_{ix}x+k_{iy}y)}\ ^2 dxdy}{\iint dxdy} = \\ = \frac{\sum_{i=1}^{N} \iint \mathrm{e}^{2j(k_{ix}x+k_{iy}y)}\ dxdy + 2\sum_{i=1}^{N} \iint dxdy + \sum_{i=1}^{N} \iint \mathrm{e}^{-2j(k_{ix}x+k_{iy}y)}\ dxdy}{\iint dxdy} = \\ = 2N \end{aligned} \tag{10}$$

We can use the average intensity in (10) together with the equation in (8) to calculate the standard deviation. The calculations of $\sigma(I\ x,y\ )$ are reported in Appendix C and demonstrate that $\sigma(I\ x,y\ ) \propto \sqrt{N}$. This is used to calculate the etching depth (H) of the DPH, which corresponds to the 'one' bit: $\Delta h_{bin}|_1$. Thus, from the results shown in Appendix C and formula (31) we have $H = \Delta h_{bin}|_1 \propto -h_0\sqrt{N}$. The design factor h_0 determines whether the etching should be deeper or shallower. If we think of the DPH as a superposition of multiple DBRs, we see that higher values of h_0 give deeper trenches, therefore higher RI contrast (Δn). From Figure 12d and the considerations on the DBR reported in the previous paragraph we learned that higher Δn results in a lower resolution ($\Delta\lambda$).[††††] In a DBR, a higher number of pairs of alternating higher and lower RI increase the resolution (Fig. 12d), as well as increasing the efficiency of the grating (Fig. 12c). More pairs translates in a larger length of the hologram (L) in the direction of light propagation. A great improvement in the resolution is also obtained from the choice of a higher grating order k (Fig. 12e). All these statements are demonstrated in the previous paragraph and can be summarized by the following empirical formula:

[††††] Resolution here is intended as the FWHM of the grating resonance in nanometers, represented as ($\Delta\lambda$). Lower resolution means a larger $\Delta\lambda$ and vice versa.

$$\Delta\lambda \propto h_0 \frac{1}{kL} \tag{11}$$

From (11) we can calculate the relationship between the etching depth H and the other design variables:

$$|H| = \propto h_0\sqrt{N} = \Delta\lambda kL\sqrt{N}$$

Since we defined $S = N\Delta\lambda$ the above equation becomes:

$$|H| = \propto \Delta\lambda kL\sqrt{\frac{S}{\Delta\lambda}}$$

Thus,

$$\Delta\lambda \propto \frac{H^2}{k^2L^2S} \tag{12}$$

Equation (12) is the result of all of the considerations about DBR and holography, united to the binarization formula (9). This is the fundamental formula of DPH that relates all the design variables. The spectral resolution of a DPH spectrometer increases – i.e. $\Delta\lambda$ decreases – proportionally the etching depth squared, so a small etching depth should be targeted to reduce the index contrast and increase resolution. A smaller index contrast also gives a smaller reflectance, which has to be compensated by having a longer hologram (L). Already from the study of the DBR we learned that a higher grating order provides smaller $\Delta\lambda$. However, the higher k the more resonances there will be in a given band, limiting the spectral range of our spectrometer. This is why we will set k=2 as the optimal design value. Surprisingly, $\Delta\lambda$ is inversely proportional to the spectral range in (12). The larger the spectral range, the higher the resolution. This means that in a DPH spectrometer a high resolution can be achieved with virtually no trade-off with spectral range. This is different from all of the other spectrometer technologies outlined in paragraph III.1. However, other effects, which are not discussed here, constrain the spectral range – such as losses from light scattering upwards in the hologram and the appearance of higher grating orders, especially when $k \geq 2$ is chosen. This essentially limits the range of a hologram to about 90 nm and forces the monolithic integration of multiple DPHs in a PIC.

III.2.3 Design and simulation of the DPH

The computation of the DPH is performed with Matlab.[207] The RI profile of the DPH is imported into Lumerical,[208] where the simulation of the response at the output channels is obtained by finite difference time domain (FDTD). The simulations are carried for the DPH that works in the red band of the spectrum, from 630 to 694 nm (436 channels and 0.15 nm spectral resolution). The DPH is 3.3 by 0.85 mm^2 in size and is 9 mm away from the RWG that illuminates it. The

output channels are offset in the horizontal axis by 1 mm. The geometry considered in the simulation is scaled down by a factor 30 to reduce computation time. As the geometrical dimensions scale, the spectral performance scales proportionally: the simulated DPH has 15 channels and a resolution of 4.5 nm. The simulated RI of the planar waveguide is 2. The results that are presented here can be immediately extended to the DPH design used in the imprints scaling everything back by a factor 30. Identical considerations also hold for the hologram that works over the NIR band.

Figure 15a shows the interference pattern obtained for the simulated hologram. The light is projected from the bottom with a beam aperture dictated by the horizontal size of the DPH and the distance from the source. The input and output constant intensities, referred to as I_r and I_o in (5), are not considered and only the spatially modulated component is plotted. The result of the apodizing function is visible across the vertical extent: the intensity fades out to zero as we move towards the upper and lower edges of the DPH. Figure 15b shows an up-close view of the interference pattern. Here the intensity map is converted into RI modulation and a 3D continuous variation of the RI between $+\frac{\Delta n}{2}$ and $-\frac{\Delta n}{2}$ is clearly visible. Δn is arbitrary and was chosen equal to 0.02 to maximize the spectral demultiplexing capability. Figure 15c depicts the same region as in Figure 15b. Here, the RI profile is binarized based on the threshold algorithm (31). The refractive index now jumps only between 2 and $2 - \Delta$n, i.e. non-etched and etched features. The circles in Figure 15c enclose features that funnel down to a few nanometers and are practically very hard to fabricate. In these situations a simple threshold algorithm fails to provide a feasible layout for fabrication. On the contrary, Spectroplan includes a function that discards these small geometries and facilitates the fabrication of the DPH. Spectroplan also changes the design to minimize light scattering that may occur as a result of the binarization algorithm and removal of these small features. Figure 15d-g are obtained by FDTD simulations, using the binarized and non-binarized RI maps that have been computed by Matlab. Figures 15d and e graph the light intensity that is focused by the DPH at the output channels. A uniform spectral and spatial distribution of the light in the channels for both non-binarized and binarized holograms is evident in the graphs. Figure 15f and g plot the spectral response of each channel for non-binarized and binarized holograms respectively. The binarization introduces an intensity distortion. This is why multiple iterations are needed in the design of the DPH to smoothen such variations with the introduction of different multiplication coefficients for each input/output. Features that are etched into the planar waveguide and apodization also must be factored in the iterations, in order to finally converge to an optimized design. Other than the intensity distortion and a slightly smaller signal to noise ratio (SNR), this simple threshold binarization already provides very good demultiplexing performance. This proves the robustness of DPH technology and gives a clue about the resilience to fabrication errors. Finally, as discussed in the previous paragraphs, the FWHM of the channels can be reduced by using a higher order of the grating. In the imprinted DPH, an order $k = 2$ is used, which yields approximately a pitch and linewidth equal to 600 and 150 nm respectively.

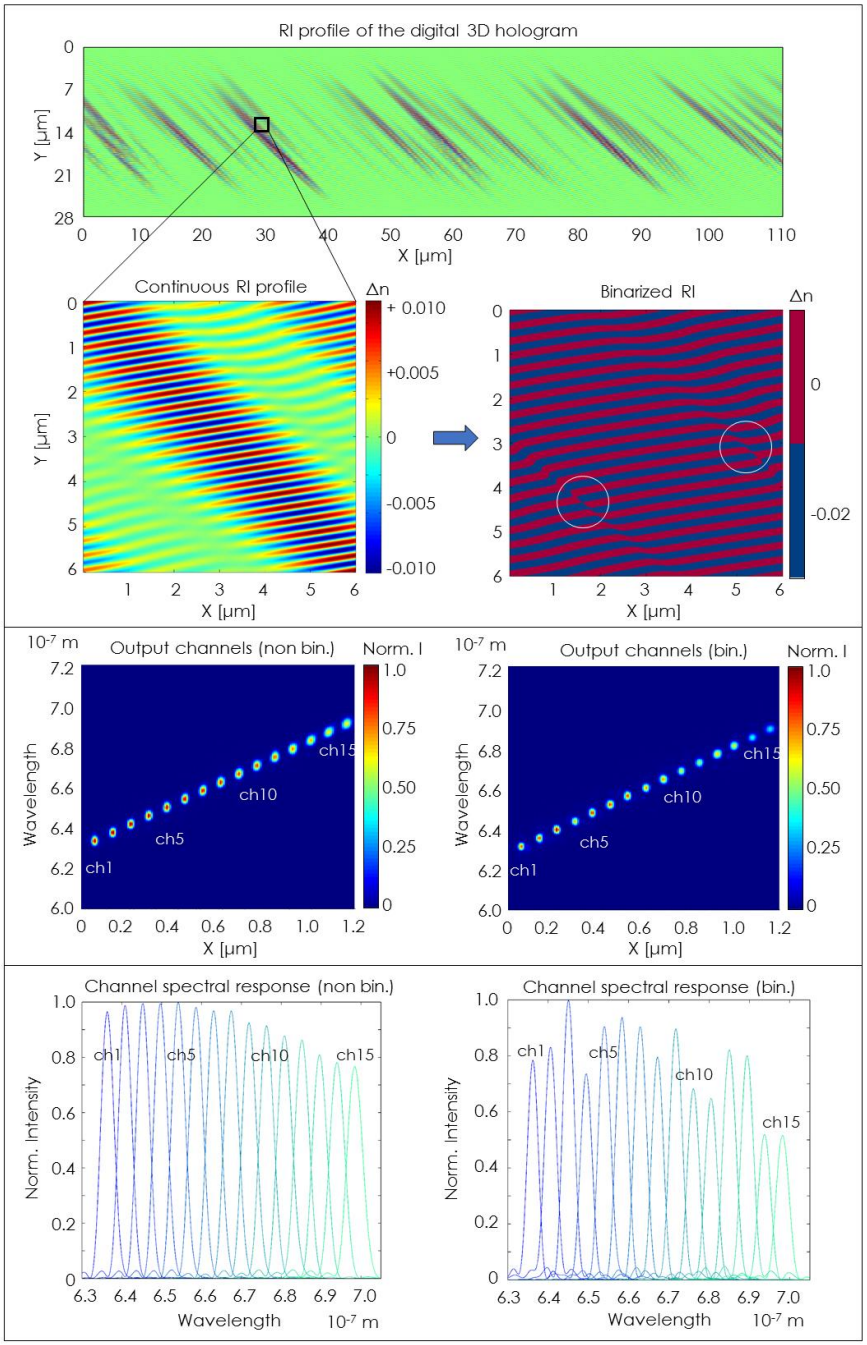

Figure 15 – FDTD simulation of a digital planar hologram design for on-chip spectroscopy. **a**. Interference pattern on the plane of all input and output waves. **b**. Close-up view of the continuous RI modulation. **c**. binarized RI profile,obtained using formula (9). **d**. spatial and spectral mapping of the foci intensity at the output of a DPH fabricated using the continuous RI profile in (b). **e**. spatial and spectral mapping of the foci intensity at the output of a DPH fabricated using the binarized RI profile in (c). **f**. Spectral content of each output channel in a DPH fabricated using the continuous (f) and binarized (**g**) RI profile.

In the next paragraph the integration of other optical components with the DPH in a planar waveguide is discussed.

III.3 Integrated optical components in the DPH spectrometer

The fundamental component of the DPH spectrometer is a wave guiding circuitry that spans several centimeters and connects the two holograms to the other functionalities of the photonic chip. The theory of integrated waveguides dates back to the 1960s and is very well developed. For more information about the underlying physics of integrated waveguides, we refer to a very famous paper by E.A.J. Marcatili of 1969.[209] Since the advent of computation, techniques like finite element analysis (FEA), FDTD simulations and the beam propagation method (BPM) have replaced time-consuming calculations for waveguides and integrated optics. Here, we report the results of some simulations that were performed on different optical components of the integrated circuitry: linear waveguide, polarizers, input taper, and directional coupler. The simplest waveguide configuration for our case that can ensure lateral confinement is represented by the RWG, a ridge of high RI material surrounded by lower RI material. This is achieved by etching the area around the RWG into a layer of high RI material, which leave a central ridge made of high RI material. The ED of the RWG should deep to allow good confinement of the photonic mode, but the DPH in the same chip should be very shallow to allow high spectral resolution. Therefore, either the RWG circuitry is deep-etched in a different lithography step from that of the DPH, or the whole device is etched with a unique ED. In the first case, the deeply-etched RWG would be capable of a very good confinement, tight bends and potentially low propagation losses. Then DPH would have to be fabricated with a second lithography and etch step, which complicates the process and may give overlay issues. This option was explored in a recent work of ours, where two lithography steps and alignment were performed by EBL.[210] The use of a unique shallow etch for both circuitry and DPH is ideal to simplify the fabrication process. Shallow waveguides can result in leakages and do not allow for tight RWG turns. Although they also provide two important advantages: propagation in shallow waveguides is less sensitive to LER, and polarization separation is straightforward. These are crucial advantages that tilt the choice in favor of the shallow ED and imprint of the whole device in one lithography step. With simple geometrical averaging and considering a grating order $k = 2$, it is easy to calculate that $\Delta n \cong 0.02$ can achieved with an ED of 15 nm on a 160 nm thick waveguide core that has $n = 2$. Silicon wafers that are coated with 8 μm thick SiO_2 and 160 nm thick Si_3N_4 are purchased from LionixBV.[211] The SiO_2 ($n = 1.46$) and Si_3N_4 ($n = 2$) function as the lower cladding and core of the planar waveguide respectively. The mode profile for a shallow etched RWG that is 15 nm tall and 1.5 μm wide is shown in Figure 16. The figure shows how the small RI perturbation on the surface of the Si_3N_4 can generate a guided mode that is mainly confined in within

the nitride. A minimum radius of curvature of 1 mm for turns in the RWG circuitry is calculated by BPM, assuming ED=15nm and a RWG width of 1.2 μm.

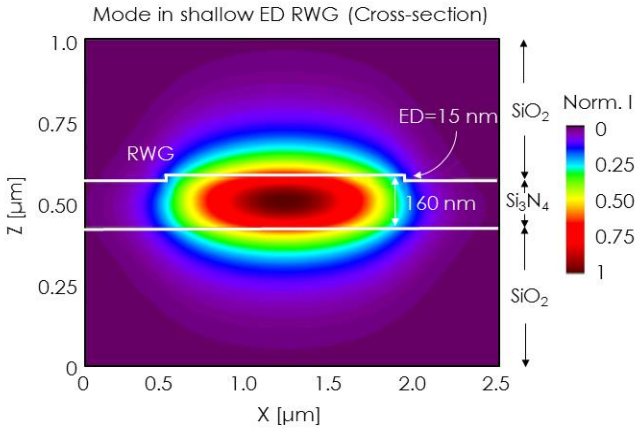

Figure 16 – Cross-sectional view of the mode in a shallow RWG. The thin ridge is sufficient to induce a refractive index perturbation that creates a guided mode in the Si_3N_4 layer.

The DPH should only receive TE-polarized light to have a unique frequency response, thus an integrated polarizer must be inserted. The etching depth and width of the waveguide can be changed to exhibit a high extinction coefficient for TM polarization (κ_{TM}) at a given wavelength. Figure 17a shows the simulation of κ_{TM} as function of the etching depth and RWG width for $\lambda = 660$ nm. The absolute maximum $\kappa_{TM} = 40$ dB/mm is achieved with a width of 500 nm and etching depth of 45 nm. As the etching depth tends to 160 nm, propagation TM-polarized light is again efficient. Figure 17b plots the variation of κ_{TM} as function of the wavelength and RWG widths for ED=40 nm. Here the maximum κ_{TM} across the spectrum that goes from green to NIR is achieved with a width of about 350 nm. Since the RWG is centimeters long, κ can be as low as a couple of dB/mm. Similar graphs for the propagation of TE-polarized light in the waveguide can be used to determine the best design parameters.

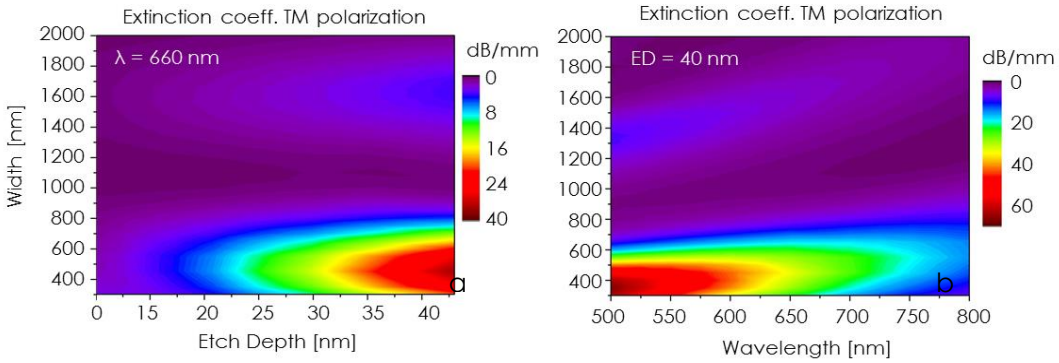

Figure 17 – Extinction coefficients for TM-polarized light propagating in the shallow RWG, as function of the RWG width and ED (**a**) and RWG width and wavelength of light (**b**).

Therefore, a waveguide width of 600 nm and 10<ED<20 nm should be used for the RWG to function as a polarizer and enable efficient propagation of TE polarization. Away from this polarizers, the width of the circuitry can be adiabatically increased to propagate light while enlarging the mode profile. This makes RWG even less sensitive to local defects and LER.
The coupling between a single mode (SM) optical fiber and integrated circuitry is achieved by means of an input taper (Fig. 18a). The taper functions by matching mode profiles of the RWG and optical fiber. The dot product of these two modes is equal to the coupling efficiency. The input taper must be much longer than the wavelength of light to allow adiabatic compression of the mode from the taper to RWG. The taper width is tuned to maximize coupling efficiency in the red region of the spectrum. Figure 18b shows the trend of the coupling as the width of the taper goes from 500 nm to 6 μm, for ED = 20 nm. The table in Figure 18c illustrates the values of taper width that maximize the coupling efficiency for different wavelengths and EDs. Given the spectral range of our DPH device, a width of 5.2 μm is chosen for the input taper with ED of 15 nm for the RWG circuitry. This will provide the small RI contrast required for the DPH and still work for the RWG circuitry, taper and polarizer.

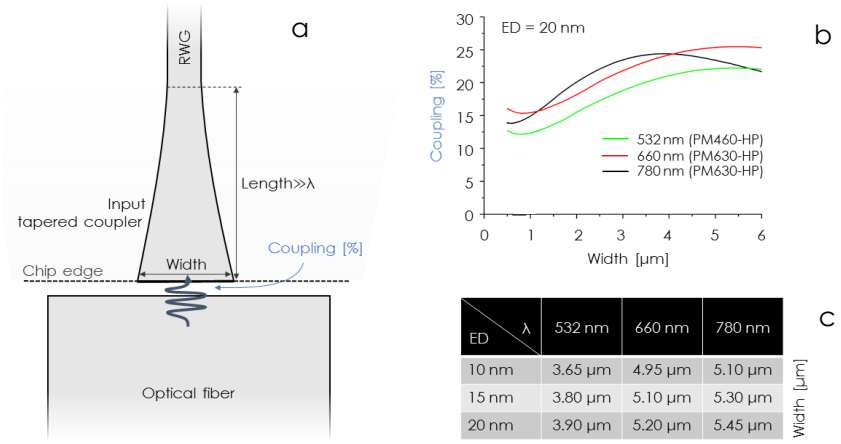

ED \ λ	532 nm	660 nm	780 nm
10 nm	3.65 µm	4.95 µm	5.10 µm
15 nm	3.80 µm	5.10 µm	5.30 µm
20 nm	3.90 µm	5.20 µm	5.45 µm

Figure 18 – Input taper. (**a**) Schematic of the coupling between an optical fiber and the RWG circuitry through the input taper. (**b**) Coupling efficiency as function of the taper width for lambda=532, 660, and 780 nm. The codes in parenthesis are the SM fibers used. (**c**) Optimal taper width for three different EDs and wavelengths.

Finally, different wavelengths must be directed to different DPHs. This is attained by means of an integrated directional couplers (or splitters).[212] The directional coupler used here consist of two parallel RWGs, called branches (or arms), which are disconnected but close enough to allow energy transfer between them. When transition between branch 1 and 2 is in phase, light switches branch. This depends on the geometrical dimensions of the splitter and wavelength of light. Choosing the correct design, different wavelengths will propagate into different branches (Fig. 19a and b). Figure 19c shows the wavelength response of the two branches of the splitter

for the holographic spectrometer considered here. A coupling efficiency into the branches higher than 75% was chosen as a threshold and two spectral ranges of operation of the DPH were determined from this. Note that since these ranges are separated by an empty band, the crosstalk between the two ranges is very low (Fig. 19c).

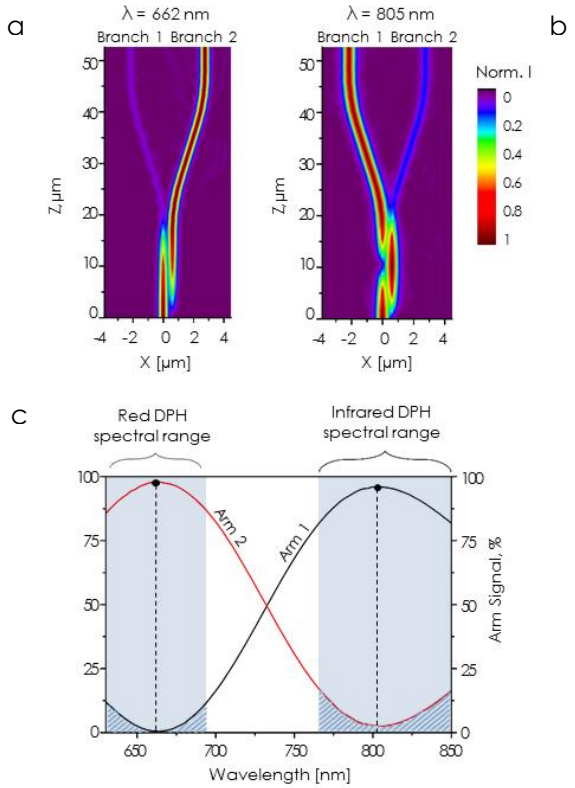

Figure 19 – Directional coupler (splitter). FEA simulation of the splitter for lambda=662 nm (a) and 805 nm (b). Coupling efficiency of the two branches of the splitter as function of the wavelength (c).

We have thoroughly discussed the theoretical foundations of DPH and the design of the integrated chip. The fabrication process by SR-NIL of this device is reported in the following paragraph.

III.4 SR-NIL and fabrication process of the DPH spectrometer

The imprint machine used here to fabricate the DPH spectrometer is an Imprio 55 by MII (Fig. 20). This is one of the first tools manufactured by MII originally for J-FIL and commercialized around the year 2004. In previous works, we have demonstrated that the Imprio 55 can be also operated to perform SR-NIL, which enabled resolution down to 7 nm linewidth and 20 nm pitch.[99,101,123] The imprio is ideally suited for use in research and development facilities, it is capable of overlay

accuracy of about 1 μm (1σ) and wafer handling flexibility up to 8-inch in diameter. The mold consists of a quartz parallelepiped of 65×65×6.4 mm^3 in size, which contains a 25×25 mm region in the center, namely mesa. The mesa is the only active print area of the mold, which corresponds to the imprinted field or dye, and is extruded 100 μm from the bulk mold. The spectrometer device is directly patterned by EBL into Hydrogen Silsesquioxane (HSQ) without etching step. HSQ is a negative resist available commercially. It is diluted at 6% volume in methyl isobutyl ketone and spincoated onto the quartz mold at 2000 rpm, which yields a film thickness around 110 nm. To allow discharging and minimize thermal heating during EBL exposure, a thin layer of conductive polymer (Aquasave from Mitsubishi Rayon) is spincoated on the HSQ film. Dose proximity correction with CATS software by Synopsis is carried out on the layout file of the spectrometer. EBL writing is carried out with a beam current of 500 pA at an accelerating voltage of 100 kV, with a dose of 3500 μC/cm^2. The EBL system used is a VB-300 from Vistec. After exposure the device is developed in a salty solution of 1 wt.% NaOH and 4 wt.% NaCl for 4 min. The salty development allows high contrast and resolution down to 10 nm. The patterned template is finally treated for several hours (usually overnight) with a fluorinated anti-adhesion layer of 1H, 1H, 2H, 2H-perfluo-octyltriethoxysilane in a vacuum oven at 90 °C.

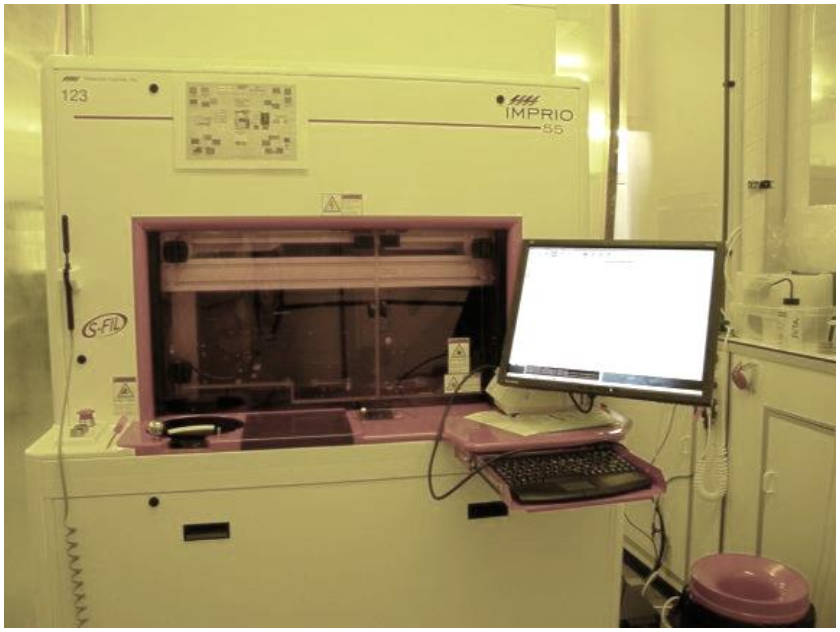

Figure 20 – Imprio 55 machine at the Molecular Foundry (LBNL)

In a collaboration project with *micro resist technology* GMbH,[97] we recently reported a study on the best resist characteristics to improve reproducibility in imprinting of photonic devices such as the DPH spectrometer.[213] In fact, while particle-induced defects remain the key concern in NIL,[214] occurrence of resist peel-off and bubble defects can be reduced by means of specific resist formulations.[109,215,216] During the

development of the SR-NIL process, a set of specifications on the NIL resist were collected that aim at optimizing the imprint performance. Based on these inputs, *micro resist technology* developed a proprietary resist formulation for SR-NIL: mr-NIL200. The dynamic viscosity of mr-NIL200 in absence of solvent is around 285 mPa·s at 25 °C. This is higher than common J-FIL resists and even of some other NIL formulations. However, the viscosity of mr-NIL200 is still sufficiently low to perform low pressures imprints (<2 bar), like it is required by SR-NIL. As discussed in paragraph II.3, much lower viscosity resists would speed up the imprint but also present wettability issues during spincoating. The reactive components of mr-NIL200 exhibit a low volatility at room temperature, so the film quality is preserved preventing any evaporation of the resist components. This formulation also contains additives that improve its adhesion proprieties to the substrate, which ensures no peeling during demolding. The introduction of these additives gives the resist film a self-priming characteristic that enables high quality printing with no need for an adhesion promoter coating. This reduces the wafer pre-processing as well as the probability of environmental contamination. However the action of these adhesion promoters on the mold is prevented by the addition of a small amount of a fluorine-based chemical, which migrates to the surface after spincoating and allows a safe demolding. Despite the presence of the fluorine-based chemical, resist descum and stripping is possible by pure oxygen plasma. A major limitation of many conventional SR-NIL low-viscosity resists is the oxygen-inhibition of their curing chemistry.[102,217] Oxygen sensitivity is particularly inconvenient in NIL, since the presence of air bubbles, imperfect mold-to-substrate contact and particles may cause locally uncured resist. The uncured resist then adheres to the template and affects the imprint of following fields. To prevent these issues, micro resist formulated mr-NIL200 to feature an oxygen-insensitive cross-linking chemistry, which guarantees mold cleanness and repeatability over several dies.

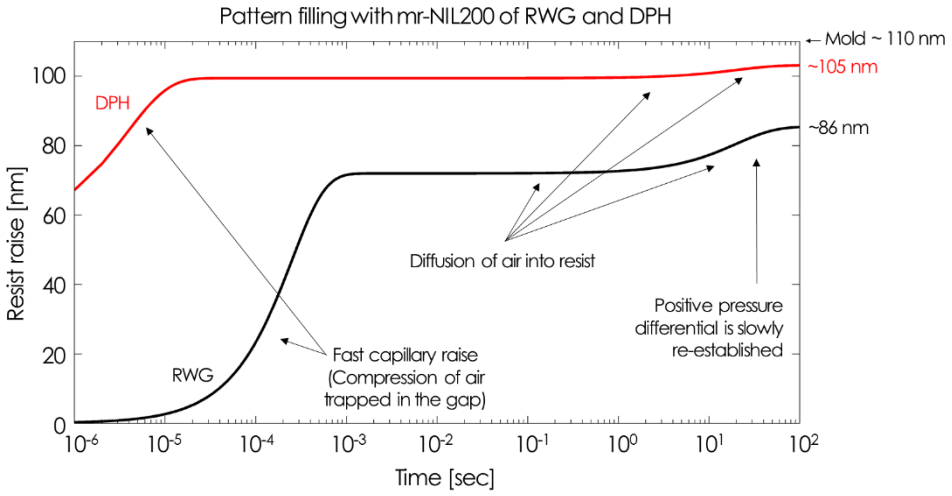

Figure 21 – Simulated pattern filling of DPH and RWG in SR-NIL process by Imprio55.

The analytical model for capillary raise in SR-NIL that was reported in paragraph II.3 and Appendix A is applied here to the typical DPH and RWG feature size, to predict filling behavior. For the imprint of the DPH spectrometer device, mr-NIL200-400nm was diluted 50% in volume with solvent ma-T1050 and spincoated at 3000 rpm for 45 seconds on 6-inch $Si_3N_4/SiO_2/Si$ wafers (see paragraph III.3).

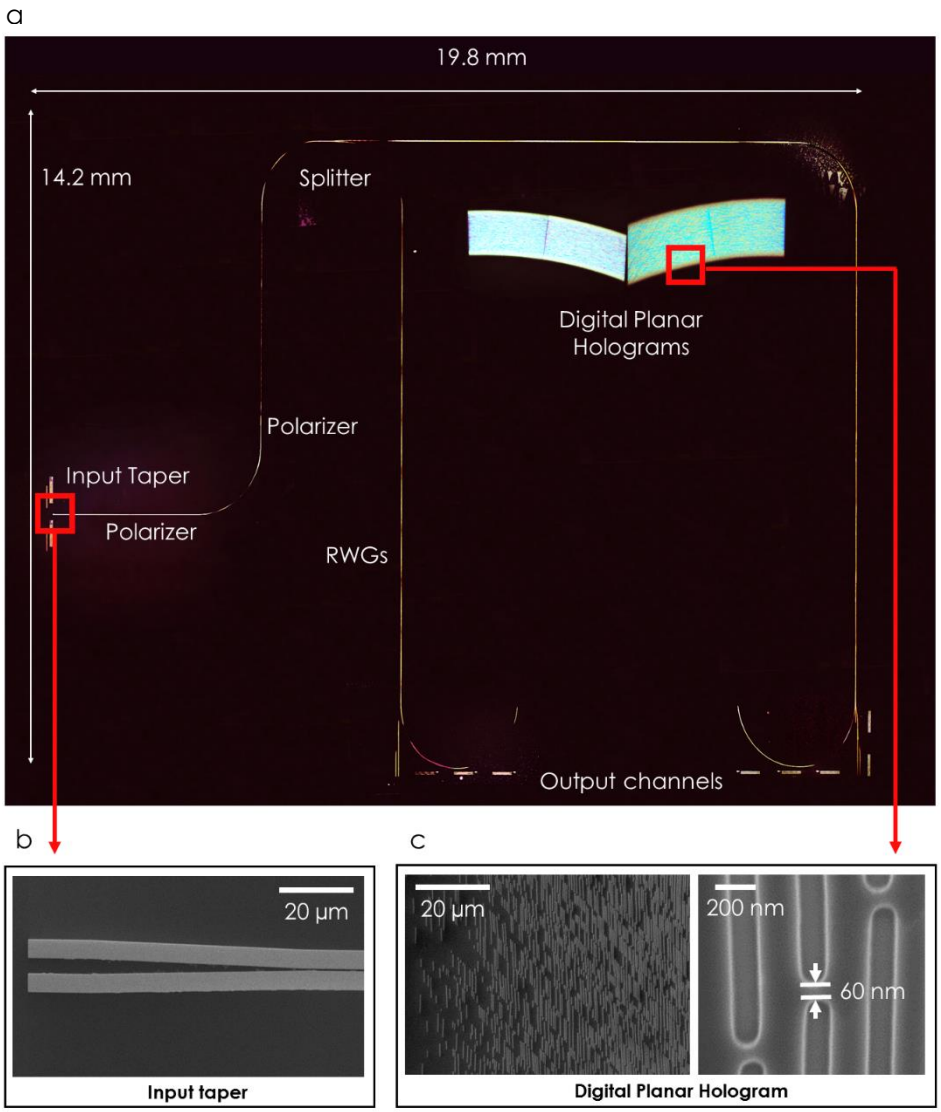

Figure 22 – Imprinted DPH Spectrometer device. **a**. Dark field image of the imprinted chip taken from an optical microscope. We chose dark field imaging since the circuit would not be visible in bright field, due to the small etching depth. The image is a combination of several photos that portrayed small sections of the chip. Pictures were taken by a 5x objective with NA=0.28. This image shows the entire device that lays on an extended imprint area with different pattern densities and sizes. **b**. Top-view of the input taper that is located at the input of the RWG circuitry. **c**. Top-view of the high-density patterns within each hologram. Here, sizes can go from a minimum feature of 60 nm, to a 120-nm groove, and density varies according to apodization.

This yielded an initial film thickness h_0 of about 120 nm. Henry's factor for the diffusion of air into the resist was set to 10^{-5} mol·m^2·Pa with a diffusion coefficient of 0.05 s^{-1}. These empirical values were obtained from previous experiments. The contact angle between mr-NIL200 and the fluorinated mold that we used in the model is 80°, which was experimentally measured in a contact angle setup. The surface tension of the fluorinated quartz is approximately $\gamma = 0.03$ Pa · m.[218] An imprint force of 40 N is used for the actual imprints, which translates into 64 kPa of pressure over the $6.25 \cdot 10^{-4}$ m^2 mesa. Figure 21 plots the results of the model for features sizes of 100 nm linewidth over 200 nm pitch (similar to DPH) and 500 nm linewidth over 5 um pitch (RWG).[†††††] The different phases of the filling mechanisms in SR-NIL can be identified. The initial fast capillary raise compresses the air inside the protrusions until the pressure differential is balanced (time ~ $10^{-5} \div 10^{-3}$ sec). The diffusion of air into the resist re-establishes a positive pressure that finally completes the filling (time ~ 100 sec). In both cases, the predicted filling is not perfect, leaving a few nanometers for the DPH and potentially as much as 24 nm for the RWG. This does not necessarily impact the residual layer, which depends on the geometrical proximity of the features and is hard to predict. Given the simulation, the pre-delay time of 120 seconds was chosen. The SR-NIL machine lowers the mold with a speed of 1 µm/sec until contact with the wafer occurs. After pre-delay time, UV light with a power density of 4 mW/cm^2 is turned on for 60 seconds and resist is crosslinked.

Figure 22a shows a dark-field optical image of an imprinted device after demolding. The totality of the optical components are successfully imprinted despite the vast size difference (see Fig. 22b and c). The presence of some filling defects is visible in the upper-right region of the device near the RWG bend. Figure 23 is a collection of SEM images that report the most common defects that were encountered during the fabrication of the photonic chip. Figure 23a shows a case of incomplete dissolution of air into the resist before curing over an extended area near DPH and RWG. These defects would certainly compromise the functioning of the spectrometer and must be avoided. Figure 23b illustrates an area of the RWG that presents incomplete filling of the waveguide ridge. Such a defect would cause light losses and prevent the light to jump from one end to the other of the RWG. Figure 23c shows a particle defect on a RWG. The defect in this case is limited to a small area of the waveguide, it would generate scattered light but might not dramatically impair the optical performance. However, such defects can be extremely harmful for the template. They might replicate over all of the dies and extend their impact as the stepping process recurs. Manual metrology investigation is performed over all the imprinted fields and those that present similar defects are discarded. The overall yield is thus determined (see next paragraph).

A residual layer thickness of about 35 ± 5 nm was measured in the DPH area (Fig. 24a). The residual layer etch is carried in an Oxford Plasmalab 80 reactive ion etcher

[†††††] Note that the analytical model for capillary raise was determined for periodic features, which is a good approximation of DPH, but not of the RWG circuitry. So prediction on the filling of the RWG is quite approximated.

(RIE), with a mixture of 17%O_2 in Ar. A gas flow of 12 sccm, radio frequency (RF) power of 100 W and pressure of 33 mTorr is used to completely etch the residual layer in 35 seconds. Figure 24a and 24b show cross-sectional views of the DPH before and after residual layer etch respectively. The patterned mrNIL200 is used as a mask to etch 15 nm into the Si_3N_4.

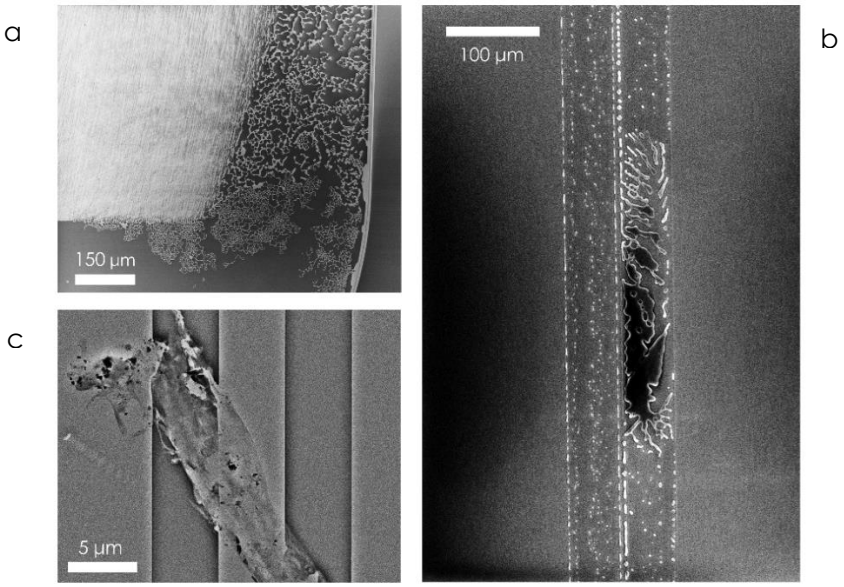

Figure 23 – Most common defects in nanoimprint of the DPH device. (a) Incomplete dissolution of trapped air. The picture shows an extended defect near one DPH and RWG, which jeopardize the functioning of the photonic device. (b) Incomplete filling of an isolated span of RWG. This defect prevents light to go from one end to the other of the RWG. (c) Particle defect in RWG. This defect would generate losses but probably would not impact the performance sensibly.

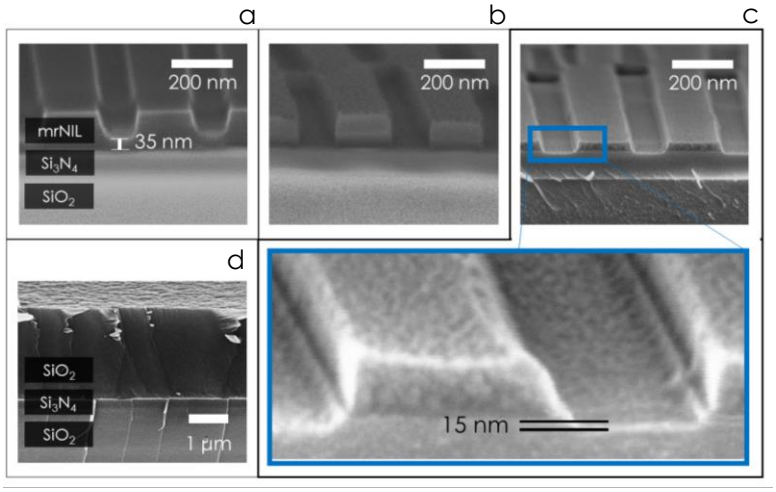

Figure 24 – SEM cross-sectional view of etching steps and upper cladding deposition. a. Imprinted lines with about 35 nm residual layer thickness. **b**. Residual layer etch to open up trenches for nitride etch. **c**. The 15-nm silicon nitride etch causes the imprint resist to visibly reduce its thickness due to the presence of oxygen in the plasma etching process, which etches. **d**. A 2-µm thick layer of SiO2 covers the patterns and seals the planar waveguide core. (NB: images might not necessarily come from the same chip spot and substrate).

The pattern transfer is achieved in RIE over 130 seconds of etching with 4% CHF_3 in O_2, a gas flow of 50 sccm, 25 W of RF power and 55 mTorr of pressure (Fig. 24c). The residual mr-NIL200 is stripped by a piranha bath. The photonic device is coated with 2 μm of SiO_2, which is deposited by plasma enhanced chemical vapor deposition at 350 °C for 30 minutes (Fig. 24d). The SiO_2 coating constitutes the upper-cladding of the planar waveguide. It encloses the guide modes thus reducing probability of upward light scattering due to particles and defects. Finally, all devices are diced along dicing marks that were included in the device layout. The edges of the chip in correspondence of the input taper and output channels are mechanically polished to improve optical proprieties.

III.5 Characterization of the SR-NIL process and performance of the imprinted devices

After imprint, but before residual layer etch and pattern transfer, each die undertakes a thorough defect inspection at the SEM and optical microscope, to ensure that no defect such as those in Figure 23 is found. A total of 180 imprints were performed and 131 fields successfully passed the defect inspection. Figure 25a is a photograph of one of the devices that passed the inspection. The diffracted light from the DPH and partly from the RWG is visible. Figure 25b graphs the statistical distribution of imprinted wafers and yield. The number of imprinted fields on a 6-inch wafer varied between 5 and 12, depending on the presence of particles and quality of the spincoated film. The statistics shows that the average yield is about 73%, and that the majority of wafers have a yield that is equal or greater than 50%. Given the fact that the work was performed in a research facility, this is a very good result. From the SEM investigation it was found that the most frequent cause of failure was airborne dust that was stuck on the wafers, probably collected during pre-processing. A smaller sample of 20 imprinted chips was chosen out of the 131 imprints that passed the defect inspection and went through a deeper optical characterization.
Spectral resolution, hologram reflectivity and RWG transmission were set to be the examining criteria to evaluate the optical performance of the imprinted spectrometers. An identical device was fabricated by EBL and used as a reference chip to compare the performance of the imprinted devices. For the measurement of the spectral resolution, a laser at 660 nm with a FHWM smaller than 150 pm was coupled in the devices (Fig. 18). Based on the design shown in paragraph III.2.3, the FWHM of the laser is narrower than the spectral resolution of the DPH. Therefore an ideal device would focus all light into one single channel and read a FWHM of 150 pm. In actual devices, scattered light from tiny fabrication irregularities generates cross-talk, which ultimately affects the FWHM reading. Figure 26a shows a top-view, long exposure photograph of an imprinted device while the 660 nm laser light is coupled from an optical fiber into the photonic circuit.

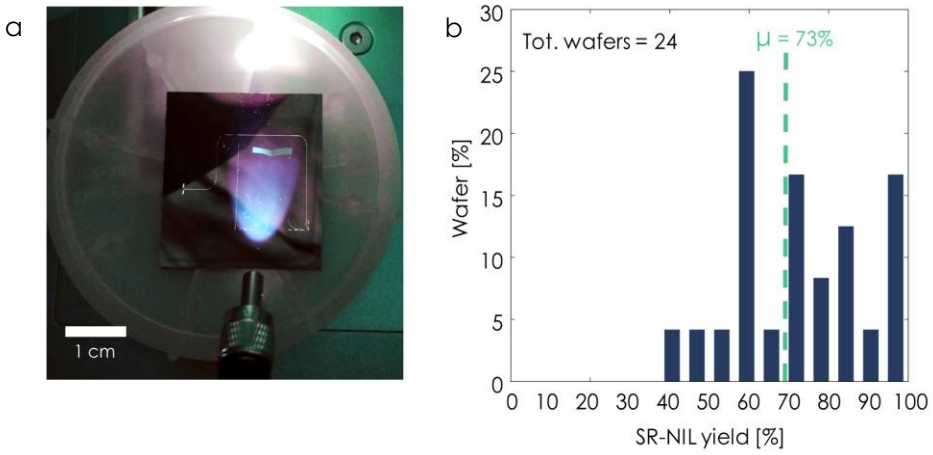

Figure 25 – **a**. Photo of an imprinted die illuminated by white light through a multimode fiber. Diffraction that comes from DPHs is clearly visible in the center of the field (whereas diffraction of RWGs was barely visible, so it has been enhanced by locally increasing the image contrast). **b**. Statistical distribution of imprint yield: satisfactory imprints from each wafer are counted and a success rate per wafer is determined. Rate of good imprints per wafer and population of wafers with a given success rate are reported on the x- and y-axis, respectively. The graph shows the wafer count for each level of success rate. Out of the 180 imprinted fields, 131 passed the defect investigation, constituting a 73% total success rate

Light propagates in the RWG and the TM polarization leaks out of the polarizers (see paragraph III.3). Once light reaches the splitter it turns into the lower branch to illuminate the DPH that operates over the wavelength of the laser. Tiny brighter spots along the RWG reveal the presence of small imprint defects, which do not affect the performance of the imprinted device. The light that scatters out from these defects and the intrinsic material losses lower the total RWG transmission. Some reference RWGs are introduced in the design, which branch out of the main circuitry and reach the edge of the chip. Light escaping from different reference waveguides is compared in order to determine of the RWG losses. The comparison of this light with that is focused by the DPH into the output channels provides a precise evaluation of the hologram reflectivity.

Figure 26b plots the output light intensity from 4 imprinted chips and the EBL device. The dark banners beneath the plots are actual views of the output channels from a CCD camera. The continuous lines in the graphs are obtained by smoothening the CCD pixel values and represent the spectrum of the laser read by the device. The FWHM here is defined as the waist of the smoothened curve at half its maximum. The statistics in Figure 26c report the distribution of all FWHM measurements for the 20 selected devices. Most of the imprinted devices read a FWHM in the range from 150 to 300 pm, equal to one to two spectral channels, as opposed to the EBL device that instead read a FWHM of 417 pm, that is 2.78 spectral channels. The average FWHM is 273 pm for imprinted chips with 111 pm of standard deviation. This indicates a higher precision of the printed chips on the spectral response compared to the reference (Fig. 26c). This difference in performance in favor of the imprinted devices is surprising. It may be due to the availability of fewer EBL devices for the development of the fabrication process, as

opposed to the numerous imprint chips that were used to fine tune all parameters and improve the SR-NIL process.

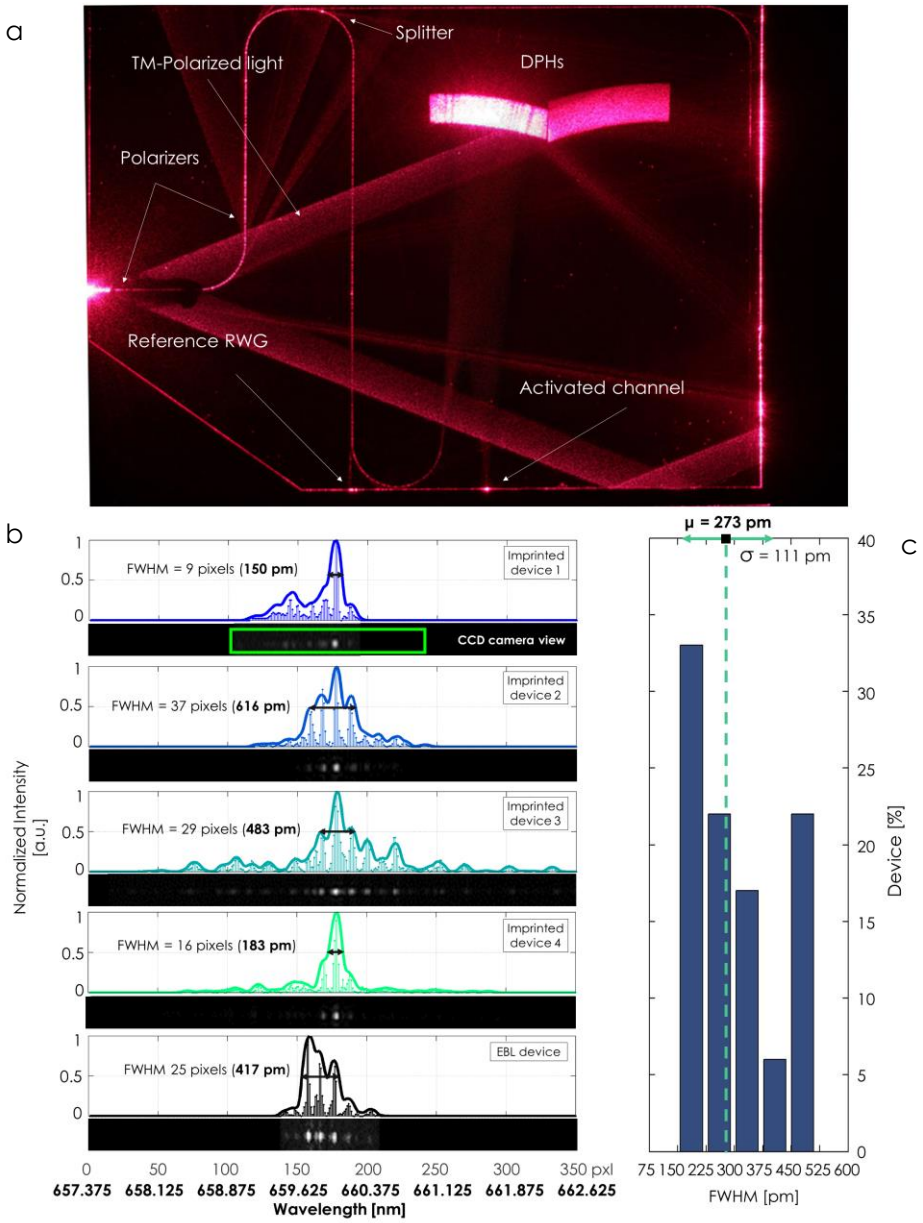

Figure 26 – **Optical characterization of the imprinted chips by OPO with λ=660 nm**. **a**. Long exposure picture of an imprinted chip while the laser light is coupled into the input taper. The TM-polarized light quite visibly leaks out of the waveguide, resulting in light beams bouncing on the planar waveguide edges and illuminating the chip. **b**. Five responses to the OPO: one EBL-fabricated and four imprinted chips. CCD cross-sectional view of the output channels is reported beneath the device responses. In the plots, stems represent normalized intensities of camera pixels, while solid lines denote the derived spectral measurements of the nano-spectrometer. **c**. Statistical distribution of the laser FWHM measured by the imprinted chips. The variance of the measurement is only 0.11 nm, which shows a high level of accuracy for all the randomly selected devices.

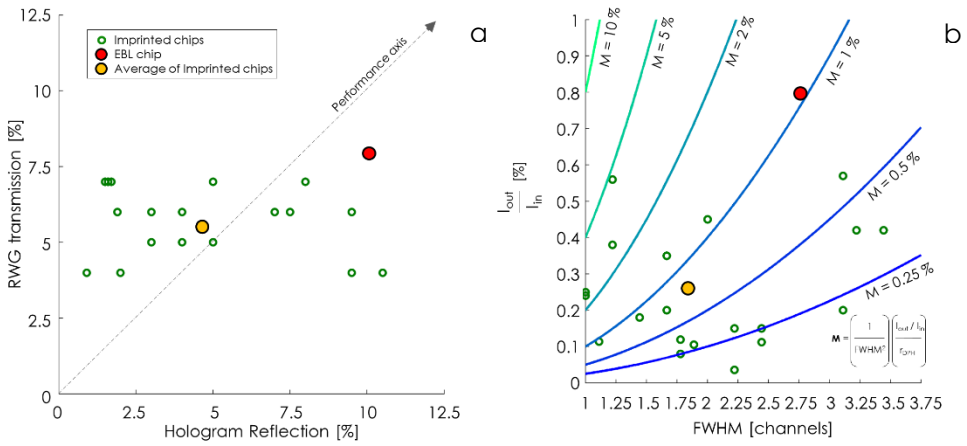

Figure 27 – Quick assessment of optical performance for device acceptance. a. Green dots denote imprinted chips with a given RWG transmission and DPH reflection. The direction of the arrow in the performance axis indicates an increase in the total efficiency. **b.** Map of the device based on the figure of merit that we use as a relative measure of the overall device optical performances. Parabolas indicate equal merit. Note that the average performance of NIL chips lays almost on the same curve as the EBL reference, which means that their merits is very similar.

Figure 27a maps the performance of the imprinted device as function of the DPH reflection and RWG transmission. Conversely, here the EBL chip performs generally better than the imprinted ones. Spectroplan simulations estimate a DPH reflection of about 10% at 660 nm, which matches with the measured hologram reflection in the EBL chip. The average DPH reflection for imprinted devices is 4.63 %. RWG transmission for EBL and imprinted chips are 8% and 5.6%. The small defects along the circuitry that were discussed earlier certainly contribute to the reduction of the RWG transmission and may explain the difference between reference and NIL chips. The overall optical performance of the imprinted chips is evaluated by the definition of an arbitrary figure of merit M, which includes all of the measured device proprieties:

$$\mathrm{M} = \left(\frac{1}{\mathrm{FWHM}}\right)^2 \frac{I_{out}/I_{in}}{r_{DPH}}\ 100\% \tag{13}$$

I_{out}/I_{in} is the overall device efficiency, which includes coupling, DPH actual reflection, and material losses; r_{DPH} is the simulated DPH reflection at 660 nm. FWHM is measured in number of activated channels. In the figure of merit, the retrieved FWHM is squared so that the performance on spectral resolution weigh more than the device efficiency. This choice is dictated by the original ambition of DPH technology to provide nano-spectrometers for high-resolution spectroscopy.
In Figure 27b, the imprinted devices are mapped in the space of M, with the x- and y- axes being respectively FWHM and I_{out}/I_{in}. This final plot demonstrates that the overall performance of the imprinted chips is in average very well aligned with that of the reference device. The average imprinted DPH spectrometer presents a merit that is only marginally lower than that of the EBL device (0.75% versus 1.05%).

In the next paragraph, the optical validation of an imprinted spectrometer is reported.

III.6 Validation the imprinted DPH spectrometers

The previous paragraph discussed a simple optical evaluation of the imprinted chips that was performed to effectively measure the yield and overall performance of SR-NIL on the fabrication of complex integrated photonic devices. The spatial distribution of light at the output channels was linearly interpreted as a spectral reading. While this is the procedure that our integrated spectrometer would ultimately use to deliver spectral measurements, it is correct only if the spectrum within each output channel is exactly 0.15 nm, and there are neither spectral nor intensity distortions. Measurements of the light spectrum of coming out from each output channel is very time consuming and cannot be performed for all of the imprinted devices. To achieve this characterization, light from a super luminescent diode is coupled in the photonic chip. The spectrum of the diode spans several tens of nanometers and covers many output channels of both DPHs. An optical fiber that is connected to a Fourier spectrometer is accurately aligned with each output channel. Channels are spaced apart 8 μm along the chip edge, so spectral content of individual outputs can be coupled into the optical fiber. Figure 28a and b plot the results of this measurements for both red and NIR DPHs. The spectral width is 138±7 nm and 169±10 nm for the red and NIR DPH respectively, in very good agreement with the design. The channel intensity is very even, so no distortion in the spectrum is introduced. The cross-talk between channels is also very low for the red DPH and within the acceptable tolerance for the NIR DPH.
Figure 29 shows the final prototype of a "spectrometer-stick", which is the result of the integration of an imprinted photonic device with a printed circuit board (PCB). The electronic/photonic device terminates in a FC/PC connector for SM fibers on one side and a USB port on the other side for connecting to a computer. To ultimately validate DPH technology and the SR-NIL process used to fabricate the photonic chip, the spectral emission of a laser diode – operating below lasing threshold – was measured by both our spectrometer and a commercially available one by Avantes.[219] Figure 29 reports the result of the measurement: the upper banner graphs the intensity measured by a CCD array at the output of the chip, which is represented by the gray curve in the plot beneath. The interpolation of this quantized spectral samples forms the spectrum of the laser light as seen by the imprinted spectrometer (green curve). The red curve is the spectral measurement of the same input light that was obtained by the commercial spectrometer. The spectra from both spectrometers are very similar. This graph, united with all of the previous results, confirm the great potential of SR-NIL technology to fabricate miniaturized spectrometers with optical performance that are aligned with that of conventional, bulkier, free-space optical systems. Due to the high-level integration and complexity of the photonic device demonstrated here, these results can be virtually extended to a variety of other components. Put in a wider perspective, this proves that

nanoimprint can potentially represent the most flexible and cost-effective solution for the fabrication of a number of advanced PICs in pilot productions, even in research facilities.
In the next chapter these results are taken even farther. A one-step nanoimprint process of planar photonic devices is enabled by the formulation of a functional printable material with high RI. The transition to the next chapter takes us from the pure technology considerations explored here to a deeper study on how materials science can contribute to the fabrication of photonic devices. We will also slowly progress toward photonic chips that allow off-the-plane light coupling and a more versatile integration. This path will ultimately lead us to the conclusive remarks and ongoing research where three dimensionality in photonics and more embedded material functionalities are tackled.

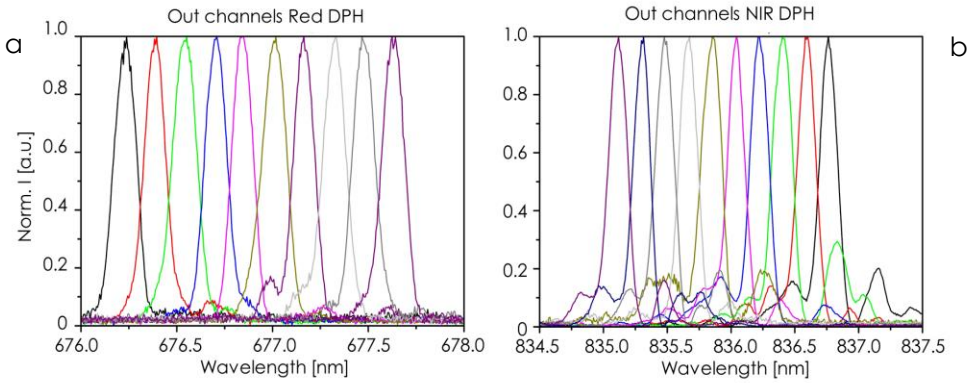

Figure 28 – Characterization of the spectral responses from output channels for the DPH that operates in the Red (a) and NIR spectral range (b).

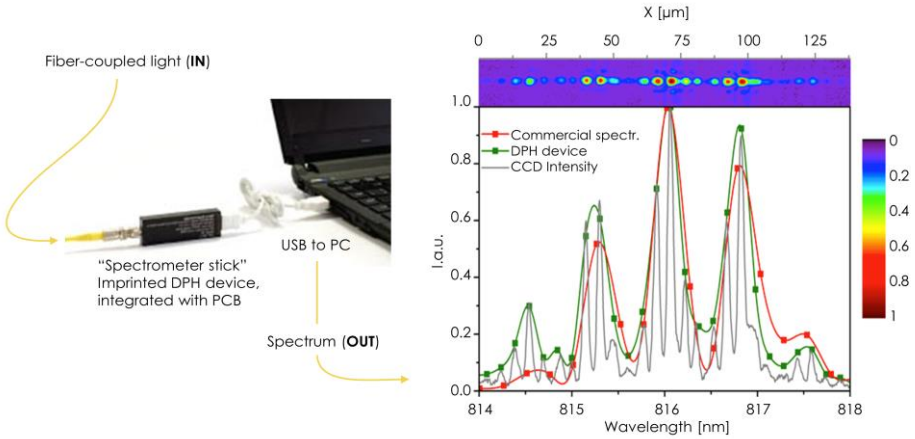

Figure 29 – Validation of the imprinted DPH on-chip spectrometer. The sprectrum of a laser emitting below the threshold is measured by a commercial spectrometer and out DPH integrated device. The spectral readings are is very good agreement, which validates DPH technology and SR-NIL for the fabrication of thiss category of integrated photonic devices.

IV. Fabrication of planar photonic devices by direct and reverse NIL of a high-refractive index sol-gel material

IV.1 Novel TiO_2 sol-gel material for nanoimprint

The previous chapter demonstrated the reliability of SR-NIL on the fabrication of a complex integrated photonic device. The imprint process was limited to the lithography stage and an etching step was required to transfer the imprinted patterns into the core of a planar waveguide. If the lithography step returned directly the final photonic device with no need for etching, the fabrication would present an even lower COO, higher convenience and throughput. One way to achieve such a goal is the imprint of a functional material, which is a material that carries the ultimate proprieties of the device. In case of photonic devices, an ideal functional material would have a high RI, so as to more easily allow the control of light creating guided modes or introducing a phase shift. For this purpose, a material that presents a high RI and low viscosity show be formulated. The material should also be imprintable with a high resolution and transparent in the range of operation, i.e. visible light. In this chapter, TiO_2-based material is formulated and used to imprint high RI structures in a single step, which fully shows the versatility of this technology for the fabrication of photonic devices. An integrated DPH light demultiplexer and a PhC slab is demonstrated by direct UV-NIL and R-NIL respectively. The first application recalls the work that was reported in the previous chapter and advances it with the introduction of bottom-up chemical functionalities (high RI). The imprint of PhCs on a transparent substrate allows us to explore photonic behaviors in transmission modes. By doing so, we begin to shift the paradigm of imprintable photonics from in-plane to out-of-plane coupling.

The TiO_2 imprintable material is obtained by sol-gel processing, which is a method for producing solid materials from small molecules.[220] This is achieved by using a colloidal solution (sol) that acts as a precursor for the formation of an integrated network (gel). A colloidal solution is a suspension of solid particles in a liquid where the dispersed material is so small (typical is the range of 1 to 1000 nm) that

interactions are mainly dominated by short-range forces – i.e. van der Waals and surface charges. In the sol-gel process, the starting compounds for preparing a colloid consist of a metal or metalloid element that is surrounded by various ligands, usually alkoxies, such as methoxy ($\bullet\,OCH_3$) or ethoxy ($\bullet\,OC_2H_5$), since they react readily with water. Without loss of generality, let us consider the case of silicon to show a typical reaction that transforms a sol into a gel. The starting metalorganic silicon molecule in the colloid can be written as $\mathrm{Si\ OR}_{\ 4}$, where R is any open ligand or an alkoxy group. The addition of water generates the following hydrolysis reaction:

$$\mathrm{Si\ OR}_{\ 4} + \mathrm{H_2O} \rightarrow \mathrm{HO\text{-}Si\ OR}_{\ 3} + \mathrm{ROH} \tag{14}$$

If R is an alkoxy, then ROH is an alcohol. Depending the amount of water and catalyst the hydrolysis may go to completion:

$$\mathrm{Si\ OR}_{\ 4} + 4\mathrm{H_2O} \rightarrow \mathrm{Si\ OH}_{\ 4} + 4\mathrm{ROH} \tag{15}$$

Partially hydrolyzed molecules can link together in either one of the following a condensation reactions:

$$\mathrm{OR}_{\ 3}\mathrm{Si\text{-}HO} + \mathrm{HO\text{-}Si\ OR}_{\ 3} \rightarrow \ \mathrm{OR}_{\ 3}\mathrm{Si\text{-}O\text{-}Si\ OR}_{\ 3} + \mathrm{H_2O} \tag{16}$$

$$\mathrm{OR}_{\ 3}\mathrm{Si\text{-}HR} + \mathrm{HO\text{-}Si\ OR}_{\ 3} \rightarrow \ \mathrm{OR}_{\ 3}\mathrm{Si\text{-}O\text{-}Si\ OR}_{\ 3} + \mathrm{ROH} \tag{17}$$

The reactions in (16) and (17) liberate molecules such as water (16) and alcohol (17) and form longer molecules in a process called polymerization. If the monomer involved in this reaction can make more than two bonds, then there is no limit in the final size of the molecule. When the reaction reaches macroscopic dimensions and extends throughout the solution, the substance is called gel. The gel consists of a continuous skeleton that encloses a liquid phase. The polymerization in a sol-gel material can be induced by UV-light using compatible photo-initiators and cross-linkers. The trapped liquid phase can be evaporated by baking (or annealing), which results in the reduction of the gel to an almost pure matrix of metal oxide. In the example reported above, the annealing step would result in a matrix of SiO_2.
TiO_2 is a particularly attractive material in visible light applications due to its high RI (n~2.5 in the anatase form) and low extinction coefficient in the visible wavelengths range. Organic–inorganic metal alkoxides materials (including TiO_2) developed by sol-gel process for direct patterning of high RI nanostructures have been already tested.[221-226] However, alkoxide precursors are highly reactive and form pre-condensed solid films of TiO_2 gel just after spin-coating.[227-229] This means that high pressures are required to carry the imprint, which leads to poor film homogeneity. Some solutions have been proposed to control the polymerization process and facilitate the imprint. One approach consists of retaining the solvent inside the polymer film. This promotes flow into the mold protrusion since it acts as a plasticizer for the sol-gel material.[221,222,226] In all of the situations where this approach was employed it resulted in non-uniform films due to uneven solvent evaporation. Other solutions rely on different hybrid organic–inorganic chemistries.

For instance, alkanoate-based precursors and metal-methacrylate systems have been used in UV-NIL of TiO_2 and ZrO_2 sol-gel materials.[230,231] Unfortunately, the former suffer from a large material shrinkage and low imprint throughput, whereas metal-methacrylate systems contain low molecular weight precursors that evaporate quickly after spincoating, leading to numerous film defects.

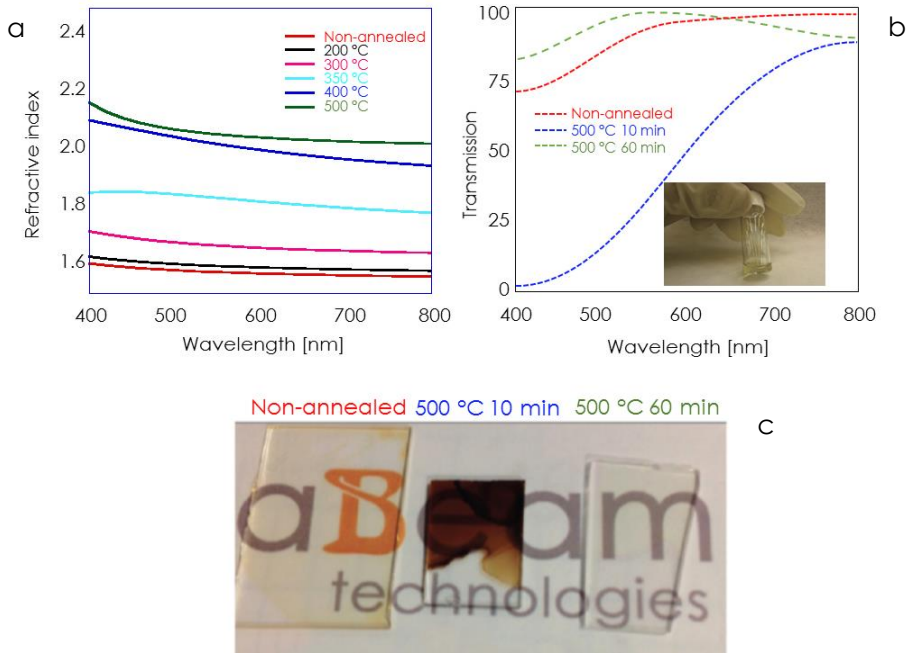

Figure 30 – Optical proprieties of the TiO2 printable material. a. Refractive index (λ=600 nm) as function of the wavelength and baking temperature. **b**. Plot of the transmission through a 1 µm thick film of TiO2 as a function of wavelength baked at different temperatures. Inset: vial containing the printable material. **c**. Picture of the film baked at different temperatures on a logo of aBeam Technologies.

Recently we have developed a titanium-based inorganic–organic hybrid material by sol-gel processing that can form a TiO_2 crack-free films over a large area.[94,232] The resin was synthesized by mixing titanium ethoxide[233] with a photoinitiator, an organic crosslinker and 3-butenoic acid, all diluted in propylene glycol methyl ether acetate (PGMEA). The material was formulated to provide a high RI and transparency at visible wavelengths after annealing. The appropriate choices of photo-initiator and cross-linker allow the spin coated film to present a high uniformity and homogeneity in film thickness, spanning 20 nm up to 5 μm. The thickness of the film is varied by changing the concentration of titania precursor in the material and tuning the spin velocity. After spin coating, the film is soft-baked at 100 °C for 1 minute to evaporate all PGMEA content. To complete polymerization the film is cross-linked under UV-light at 100 mW/cm^2 for 3 minutes. The organic phase of the gel is selectively removed by annealing the film at different temperatures. Figure 30 shows a basic optical characterization of the film. Figure 30a reports the RI measurements performed on a spin coated and cross-linked film that is annealed on a hotplate in air at different temperatures for 1 hour. The RI

was measured by a Horiba Jobin Yvon Uvisel Spectroscopy Ellipsometer. Results show that the RI can be tuned from 1.6 up to 2.04 (at λ=600 nm) by changing the annealing temperature. A RI higher than 2 is achieved throughout the entire visible spectrum after baking the material at 500 °C for 60 minutes. Figure 30b and c display the transmission curves and appearance of a 1-μm film of TiO_2 material for different annealing conditions: no annealing, annealing at 500 °C for 10 and 60 minutes. Partial removal of the organic phase (10 minutes annealing) results in a sensitive drop of the film transparency due to degradation of the organic component. The figure shows that a 500 °C bake for 60 minutes provides the desired optical performance in terms of both a RI~2 and a transparency higher than 90% at a wavelength of 600 nm. X-ray diffraction analysis was performed on films baked at 400 and 500 °C. Measurements show that the film consists of pure TiO_2 molecules in amorphous state at 400 °C. The material transitions to an anatase polycrystalline structure at 500 °C, which explains the increase in RI and transparency of the film. More importantly, we characterized the mechanical proprieties of the resin by performing a direct UV-NIL on a spin coated film (Figure 31). Direct UV-NIL is very similar to SR-NIL on pre-spin coated film, in that the underlying principles for pattern filling and replication are the same (see paragraph II.3). The process starts by mechanical printing a spin coated film of TiO_2-based material at a low pressure (<1.5 bar), which is still liquid after soft-bake (Fig. 31a). Due to the low viscosity of the resin, the filling mechanism is ruled by capillary force. After UV-light curing (Fig. 31b) the printed patterns are demolded (Fig. 31c). The substrate is finally annealed to attained high RI patterns (Fig. 31d). Instead of performing an automatic stepping process as in SR-NIL, here molding and demolding are carried manually. This process is more suitable to research facilities and R&D projects since it allows for more experimental flexibility. On the other hand it can be less reproducible and harder to control, so less appropriate for prototyping and pilot productions. To evaluate the imprinting proprieties of the synthesized material, a simple test mold with different gratings ranging from 500 to 40 nm pitch was fabricated in HSQ on a Si substrate by EBL, using a very similar process to that described in paragraph III.4. The fluorosilane treatment for anti-adhesion is also reported in the same paragraph.

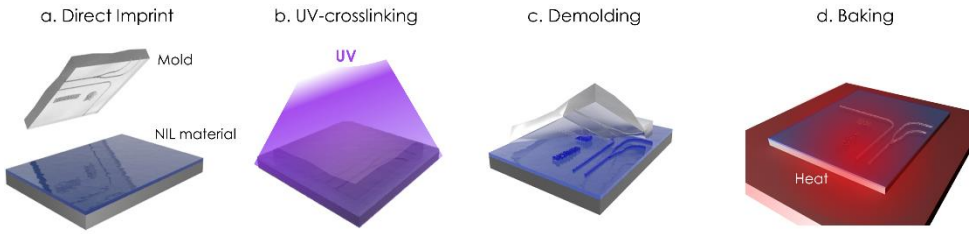

Figure 31 – Direct UV-NIL patterning process for printable photonic devices. a) A spin coated film is manually imprinted using a stamp. b) During imprint, the resin is cross-linked under the action of UV-light. c) The stamped patterns are revealed by demolding the hardened resist. d) The material is annealed (baked) on a hotplate to attain pure TiO_2 structures.

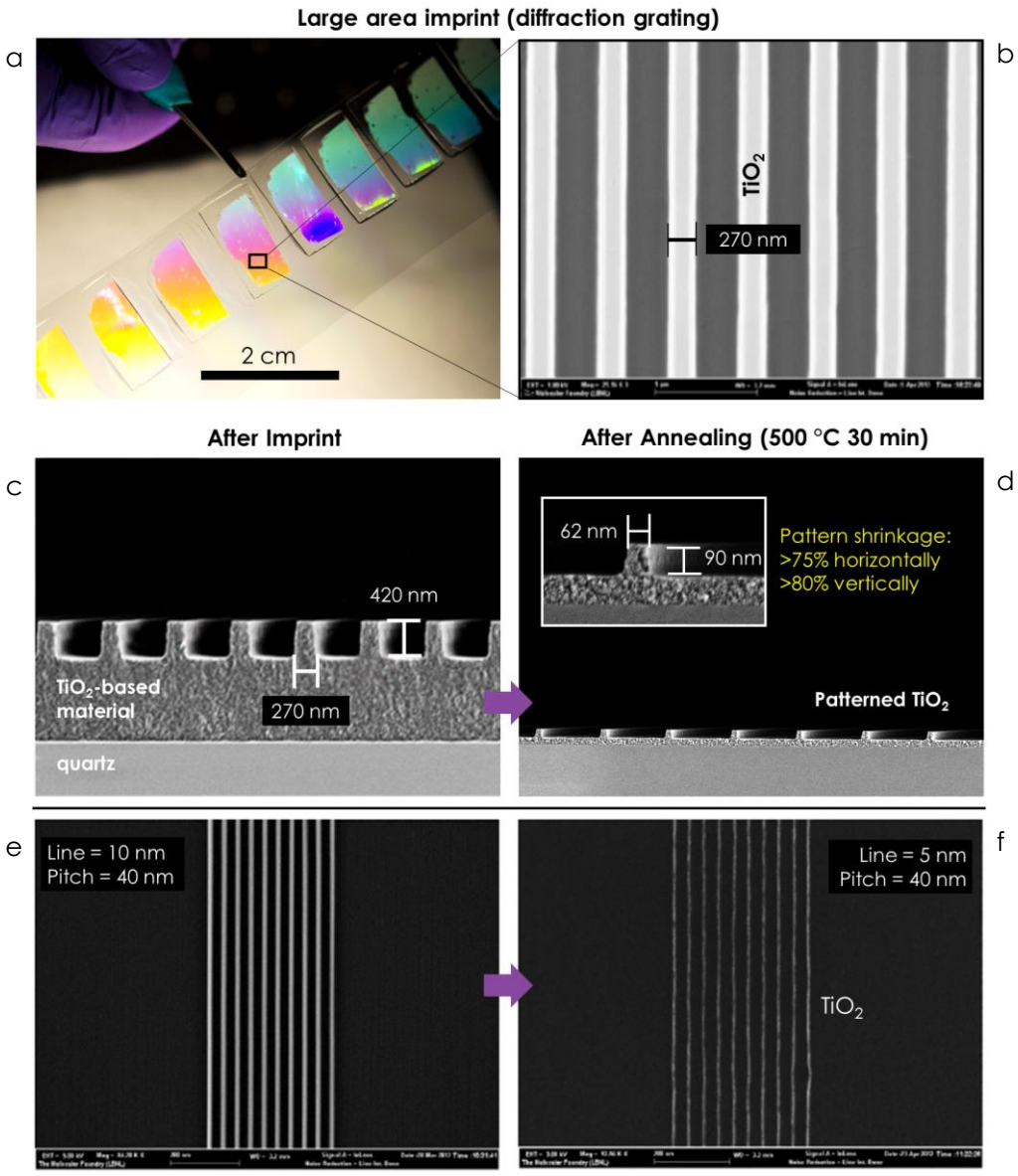

Figure 32 – High resolution gratings imprinted on a transparent substrate using the TiO_2 material. a. Large area imprint of several chips by manual step and repeat on a microscope quartz slide. The diffraction from the grating generates different bring colors, which give an indication of the good imprint quality. **b**. SEM top-view a central area of the imprinted grating. **c**. SEM cross-sectional view of the grating in (b). **d**. SEM cross-sectional view of the grating in (c) after annealing. A material shrinkage higher than 75% was calculated. The porosity is due to the polycrystalline structure of the material. **e**. High-resolution imprint of a grating. The image shows the excellent mechanical properties of the synthesized material for NIL, with very smooth LER and pattern uniformity down to 10 nm linewidth. **f**. SEM top-view of the same grating after annealing at 500 °C for 30 minutes. Pitch stays the same, but the linewidth shrinks to 5 nm.

The results and metrology characterization of the imprint tests are reported in Figure 32.[94] Figure 32a shows some large area imprints of the grating, which was manually stepped on a quartz microscope slide. Diffracted light generates different

colors that indicate the high-quality of the imprinted patterns. Figure 32b and c show a SEM top-view and cross-section respectively of the imprinted grating. The initial film thickness resulted in a very thick residual layer. However, post-annealing images show that the material exhibits a shrinkage greater than 75%, which reduces the residual layer along with all of the other dimensions, except the pitch of the grating, which stays the same (Fig. 32d). The shrinkage is associated with loss of organic matter from the NIL material. The inset in Fig. 32d displays a close-up view of a TiO_2 line, which exhibits a high granularity of the material after annealing. This is most likely caused by the different orientations of the crystals inside the film. Finally, Figure 32e and f show the results after imprint and annealing of a high-resolution grating. The imprinted patterns feature a high uniformity and very low LER, in spite of the very small linewidth (~10 nm). After annealing, the linewidth reduces to 5 nm (Fig. 32f). We found that an exact prediction of the shrinkage in the different dimensions is very hard to make, since it depends on the imprint parameters, annealing conditions, amount of titania precursor in the material, initial film thickness and geometry of the patterns. We experimentally found shrinkage rates in the range of 50% to 90%. The shrinkage can be exploited as an advantageous propriety of the imprint material in order to go beyond the resolution of the mold, as it is shown in Figure 32f. More importantly, shrinkage allows for a wider tolerance in the control of the residual layer during imprint. Even when these advantages are not needed, the loss of CD may not compromise the performance of the imprinted device. This is the case of the planar photonic devices that are demonstrated in the next paragraph. In other cases instead, the size reduction is a strongly limiting factor that prevents the fabrication or the functioning of the device. This is the case of the PhCs slab discussed in paragraph IV.3, where a high-fidelity imprint process will have to be designed to eliminate shrinkage.
The novel TiO_2 sol-gel material has demonstrated very good optical proprieties, a RI higher than 2 and transparency in the visible range as well as an excellent imprintability. The high uniformity of the crack-free film enabled homogeneous imprints of a grating with linewidths down to 5 nm. The high-refractive index functionality and suitability to high-resolution NIL enable the single-step, direct patterning of photonic structures into the synthesized resist. In the next chapter, the resist is tested on the direct fabrication of a DPH-based wavelength demultiplexer, and other planar RWGs.

IV.2 Direct printing of integrated DPHs and RWGs in the TiO_2 sol-gel material

IV.2.1 Direct UV-NIL process results

Our TiO_2 material is tested on the direct UV-NIL patterning of planar photonic devices for light guiding (RWGs) and demultiplexing (DPHs).[234]

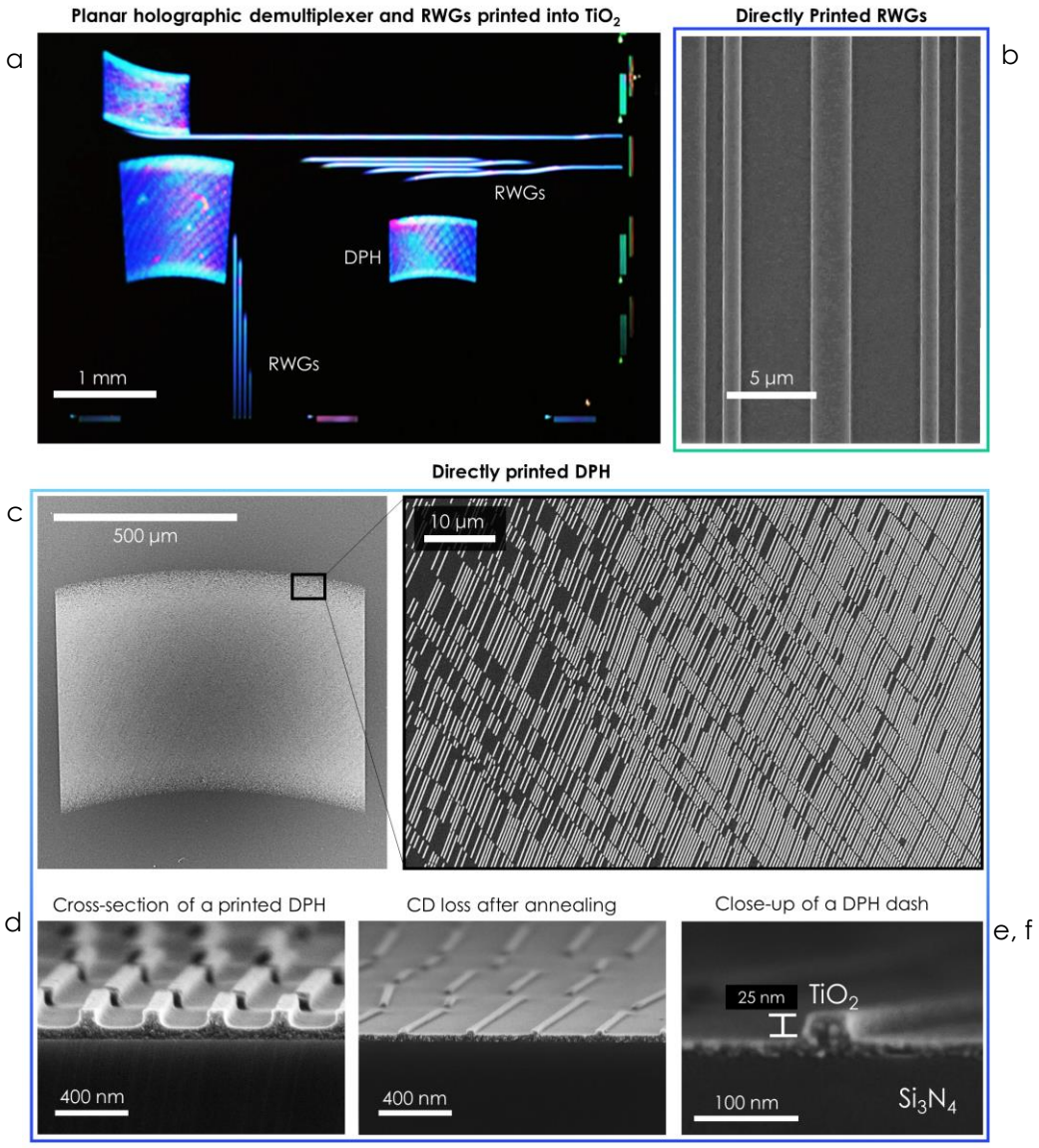

Figure 33 – Imprinted planar holograms and waveguides in the high-RI TiO_2 sol-gel material. **a**. Dark-field photograph of an imprinted photonic chip. **b**. SEM top-view of an imprinted RWG. **c**. SEM top-view of the four-channel DPH DEMUX, which contains millions of sub-150 nm dashes. The SEM shows that the entire DPH is uniformly imprinted with no visible defect. **d**. Cross-sectional SEM view of imprinted DPH dashes before (d) and after annealing (**e**,**f**).

The theoretical notions behind the DPH and RWG are thoroughly discussed in paragraphs III.2 and III.3, so the fabrication and optical results are immediately presented here. The mold layout consists of DPHs that work on different wavelength ranges and output channels. Unlike the holographic spectrometer shown in chapter III, here light is projected towards the hologram directly from the chip edge. The RWGs are not connected to the DPHs and their purpose is to measure losses in the printed waveguides. Three Y-splitters[235] branch out of the main RWG and lead to

four 90° turns that have different radii of curvature. BPM simulations show that 95% of the light can be transmitted through turns with curvature radii greater than 900 μm. The bends also ensure that no straight light from the waveguide input reaches the output, which would nullify the characterization of propagation losses. The mastermold of the planar chip is written by EBL into HSQ, which is coated with an anti-sticking layer (see paragraph III.4 for process details). Depth of the mold is about 120 nm. The master-mold is replicated into a daughter mold by means of an Ormostamp and hard-polydimethylsiloxane (PDMS) bilayer. The daughter mold also goes through the same anti-sticking treatment to prevent TiO_2 features from getting stuck inside the mold intrusions, which would be very hard to remove. The direct UV-NIL process depicted in Figure 31 is used to print the photonic components. The TiO_2 sol-gel material is spin coated on a substrate formed by 160 nm Si_3N_4 and 8 μm SiO_2 on silicon. This is the same planar waveguide structure used in Chapter III to fabricate the on-chip spectrometer. After imprinting, the chip is baked at 400 °C for 60 minutes to remove the organic phase of the polymer and reach a high transparency with a RI of 2.05.

The result of this process is showed in the dark-field photograph of Figure 33a: the printed photonic chip is illuminated by orthogonal white light sources that generate blue light diffraction at the DPHs and along the straight RWGs. The horizontal and vertical RWGs are connected although the bends cannot be seen in this image due to the limited number of illumination points. The change in color within the DPHs indicate a local variation of the residual layer thickness of about ±5 nm. However, the photograph demonstrates that a high replication quality over the full 5×4 mm^2 area can be achieved by imprinting the TiO_2 material. The UV-NIL produced uniform filling of both the RWGs (Figure 33b) and DPH lines (Figure 33c-f), that is micrometer and nanometer size features respectively. Figure 33c displays SEM top-view images of an imprinted holograms in the chip, with the high-fidelity replication of millions of sub-150 nm dashes. The SEM cross-sectional view in Figure 33d show that a residual layer thickness of about 60 nm is present beneath the DPH dashes. A shrinkage after annealing of about 50% and 60% for the lateral and vertical dimensions respectively is revealed by Figure 33e and f. This leads to a final thicknesses of the residual layer of about 18 nm with the DPH dashes being 25 nm high. Similar values of shrinkage are observed in the RWG for the vertical dimension, while no major CD loss is recorded for the lateral dimension due to the large width of the RWG.

As aforementioned, the photonic devices are printed onto a planar waveguide core of Si_3N_4. Due to the small RI contrast between TiO_2 and Si_3N_4, the fabricated patterns act as a superficial RI perturbation similar to that induced by etching the Si_3N_4 waveguide core, which was reported in Chapter III. The difference between the planar device from Chapter III and this is that here we are using an additive fabrication process (direct printing), instead of subtractive (etching). For light propagating in the plane there is no boundary between the Si_3N_4 and the added TiO_2 layer, with the latter being just an extension of the former. As a result, a mode profile similar to Figure 16 is obtained for the shallow TiO_2 RWGs, with light almost completely confined within the Si_3N_4 layer and guided in the plane by the superficial

TiO_2 patterns. The presence of a thin residual layer does not compromise the device functioning but it may slightly shift the central wavelength of operation. However, if a heavy residual layer variation is present this can result in light aberration. As far as the DPH is concerned, a lateral shrinkage of the dashes does not shift the spectral range of operation, since this is defined by the pitch of the grating rather than the linewidth (see discussion on Bragg grating and DPH in paragraphs III.2.1 and III.2.2). The fabrication of the device is completed by depositing 2 μm of PECVD SiO_2, which acts as the upper cladding of the planar waveguide.

IV.2.2 Optical characterization of the printed TiO_2 devices

The optical characterization of the imprinted device is carried in a homemade optical setup. Laser light with a wavelength of 660 nm is coupled from a SM fiber (630 HP) into the main RWG by precisely placing the fiber in proximity of the RWG input at the chip edge. This operation is carried using a mechanical XYZ-stage. The output light is collected by a 40× objective and focused onto a CCD camera. Figure 34a shows a photograph of an imprinted chip during laser coupling into the RWG circuit. To measure insertion loss of the RWGs, light intensity exiting the waveguide is recorded in the CCD camera. In a second time, the output light from the same RWG is coupled into another fiber, which leads to the same CCD camera. The ratio of the intensities that are measured in these two experiments gives the coupling efficiency between the fiber and the RWG, which was found to be around 7 dB. The total insertion loss was determined to be around 27 dB. The total loss is the combination of coupling and propagation losses over 5 mm RWG. From simple math, it can be calculated that propagation losses inside the RWG are around 40±5 dB/cm at λ=660 nm. This figure is comparable with values of 30 and 58 dB/cm losses that were measured by other groups in amorphous and anatase TiO_2 waveguides respectively, which were fabricated using EBL and etching.[236]
The characterization of DPH DEMUXs is carried by coupling light from a 10× objective into the planar waveguide. As light is coupled into the waveguide, it diffracts and illuminates the entire DPH. The output channels are observed from the same objective. Figure 34b shows the CCD pixel intensity recorded at the chip edge as we tune the wavelength from 624.7 to 644.0 nm. Some cross-talk between output channels is visible in Figure 34c that plots the spectral content of each output channel. Applications of demultiplexing in fiber optics communication, for instance, can tolerate some cross-talk, as long as it is low enough to not affect the bit error rate. Conversely, this level of cross-talk might not be tolerable in many areas of spectroscopy, where broadband spectra have to be measured with a very high accuracy. Preliminary optical measurements of a 100-channel DPH DEMUX have been also performed. The spectral content of one channel that has a spectral width of 0.35 nm is shown in Figure 34d, while the dispersion curve of the same device is graphed in Figure 34e. The dispersion curve relates the channel wavelength (in abscissa) to the channel position (in ordinate). The graph shows that the dispersion curve is a straight line, which is exactly the linear behavior we expect from a DEMUX.

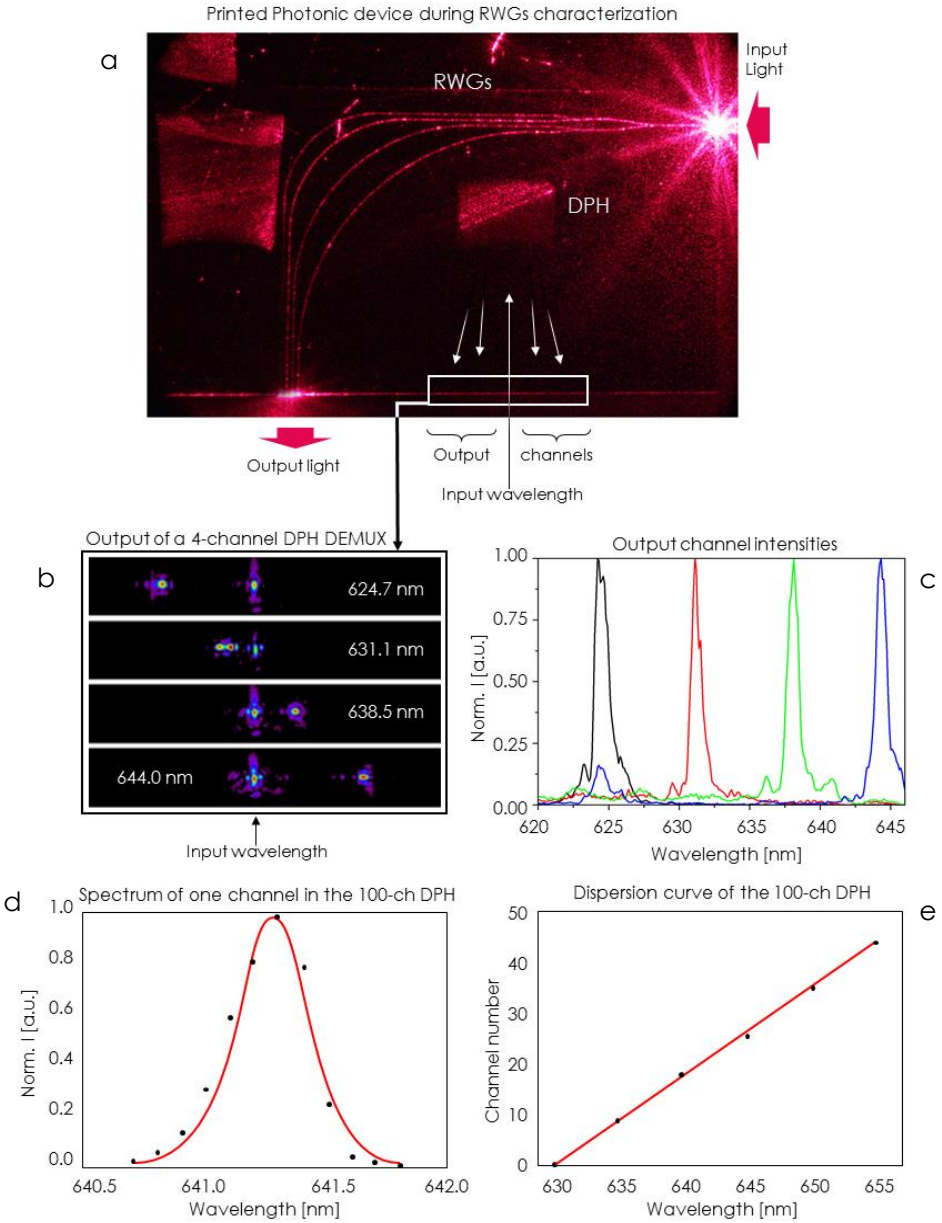

Figure 34 – Optical characterization of the printed TiO_2 RWGs and DPH DEMUXs. a. Long exposure photograph of the printed holographic circuit while laser light is coupled into RWGs. **b**. CCD camera view of the chip edge in correspondence of the DPH output channels. **c**. Spectral content of the 4 output channels in the printed DPH. **d**. Spectral content of one output channel in a different DPH DEMUX that has 100-channels. The figure shows a spectral resolution of 0.35 nm. **e**. Dispersion curve of the 100-channel DPH DEMUX.

These optical characterizations confirm the suitability of direct patterning for integrated photonic devices using our high-refractive index imprintable polymer. The central block of this report that concerned the fabrication of complex integrated photonic devices by NIL concludes here. In the final paragraphs, we will explore the

opportunity to fabricate imprintable TiO_2 PhCs for off-the-plane light excitation and collection. Following this course, we start to shift our research focus from light travelling within the plane towards the third dimension, which will ultimately lead us to discuss the ongoing research on 3D printable photonics.

IV.3 Reverse Imprint of high refractive index photonic crystals for visible light

IV.3.1 Brief overview of PhC theory and bandgap structure

Photonic crystals (PhCs) are periodic structures that affects the motion of photons just like ionic lattices formed by atoms or molecules in solids affect electrons.[21] Quantum mechanics (QM) explains how electrons avoid scattering while travelling through a periodic potential inside a conducting crystal. The explanation offered by QM is that electrons are waves, and waves that meet certain criteria can propagate through a period potential without scattering. The propagation of waves, however, can be prohibited in certain directions for certain electron energies. Equivalently, specific light wavelengths can be prevented from propagating in certain directions within a medium that presents a periodic dielectric function. Due to the relative difference in wavelength between photons and electrons, PhCs are thousands of times bigger than any atomic-scale crystal lattice. While nature abounds with lattice structures for electrons, PhCs are much less prevalent. Nevertheless, biology originated surprising biostructures where the use of periodic dielectrics is required to have an evolutionary advantage.[237] Figure 35a show the blue iridescence reflection from the wings of a Morpho rhetenor butterfly. A SEM cross-sectional view of the wings show the 3D nano-structure that composes the natural PhCs (Fig. 35b). Interestingly, the color of the organic material that composes the 3D structure is brown-gray, nevertheless the emerging color may be very different if the same material is arranged properly at the nano level. This occurs because photons with certain wavelengths cannot propagate inside the PhC and reflect backwards. In this thesis, we already encountered a special case of 1D PhCs when we discussed the response of DBRs that introduced the theory of DPH (paragraph III.2.1 and Appendix B). Even in that case, we saw that the propagation of discrete wavelengths or bands was forbidden inside the DBR. That was also a direct effect of the presence of photonic bandgaps in the DBR. In general terms, what is the physical origin of these photonic bandgaps? This is a very interesting question that is worth investigating and explains the underlying phenomenon that makes PhCs useful in practical applications. A simplified qualitative analysis on the origin of the bandgap effect and dispersion curve of PhCs is reported below as a brief theoretical introduction to the fabrication of PhCs. A more detailed description of the PhC properties is out of the scope of this thesis and can be rather found in many textbooks.[203,238-240]

Just like crystal lattices in solid state physics, PhCs enjoy a discrete translational symmetry, which means that the geometrical proprieties of the crystals are invariant

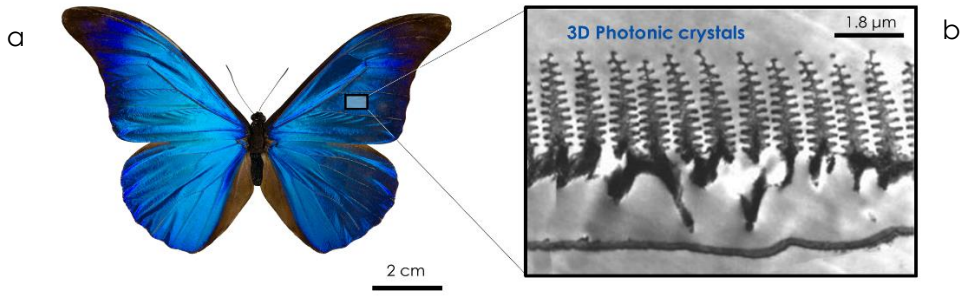

Figure 35 – Natural Photonic Crystals.[237] **a.** Photo of a Morpho rhetenor butterfly, exhibiting its blue iridescence color. **b.** SEM cross-sectional view of the butterfly patterned wings. The 3D PhC structure causes a selective reflection of blue light coming from all directions. This is a rear case of a complete photonic bandgap structure in nature.

under distances that are multiple of a fixed step length:

$$\eta\ \mathbf{r} + n\mathbf{\Lambda}_{\mathrm{i}}\ = \eta\ \mathbf{r}\quad \forall n = \pm 1, \pm 2, ... \tag{18}$$

where $\eta\ \mathbf{r}\ = \epsilon_0/\epsilon(\mathbf{r})$ is the electric impermeability of the photonic structure and $\mathbf{\Lambda}_{\mathrm{i}}$ is one primitive vector of the crystal (Fig. 36a).
Now, consider the generalized Helmholtz equation for the magnetic field:

$$\Theta\mathbf{H} = \frac{\omega^2}{c_0^2}\mathbf{H} \tag{19}$$

where $\Theta \triangleq \nabla \times\ \eta\ \mathbf{r}\ \nabla \times\ \cdot$. The equation (19) is formulated as an eingenvalue problem, the mode of the magnetic field H is the eigenfunction and $\frac{\omega^2}{c_0^2}$ is the eigenvalue. As a result of the fact that the operator Θ is Hermitian, the modes of propagation $\mathbf{H}$ inside the structure (18) enjoy the same translational symmetry of $\eta\ \mathbf{r}$. From this, it immediately follows that the eigenfunctions of (19) must be Bloch modes.[238] Bloch functions are composed by two terms: a propagating plane wave and a modulation function that is periodic with period $|\mathbf{\Lambda}_{\mathrm{i}}|$, called Bloch periodic function. To take advantage of the symmetries, let us consider only the propagation of light along the crystal vectors of a fundamental unit cell, called irreducible Brillouin zone. Any crystal node outside the irreducible Brillouin zone can be reached by a linear combination of vectors $\mathbf{\Lambda}_{\mathrm{i}}$ inside this unit cell, this is why $\mathbf{\Lambda}_{\mathrm{i}}$ are called primitive vectors. In the mathematical space of the crystal, $\mathbf{\Lambda}_{\mathrm{i}}$ are then orthogonal to each other. From the proprieties of the Hermitian operator Θ it follows that even the solutions of the wave equation along the primitive vectors are orthogonal eigenfunctions $\mathbf{H_i}$. Thus, since $\mathbf{\Lambda}_{\mathrm{i}}$ is a basis for the discrete crystal space, the modes associated with the propagation along $\mathbf{\Lambda}_{\mathrm{i}}$ also form a basis. In other words, all possible propagation states within the entire crystal are linear combinations of the propagation modes along the primitive vectors. From this we can define a reciprocal lattice where the coordinates are represented by the

wavevectors ($\mathbf{k}_\mathrm{i}$) of the propagation modes along the primitive crystal vectors $\mathbf{\Lambda}_\mathrm{i}$ (Fig. 36b). The relationship between the two will be: $\mathbf{k}_\mathrm{i} \cdot \mathbf{\Lambda}_\mathrm{j} = 2\pi\delta_{ij}$. The Bloch modes will then take the following form:

$$\mathbf{H}_{\mathbf{k}_\mathrm{i}}\ \mathbf{r}\ = e^{i\mathbf{k}_\mathrm{i}\cdot\mathbf{r}}\ \boldsymbol{u}_{\mathbf{k}_\mathrm{i}}(\mathbf{r}) \tag{20}$$

Where $e^{i\mathbf{k}_\mathrm{i}\cdot\mathbf{r}}$ is a plane wave with wavevector $\mathbf{k}_\mathrm{i} = (\frac{2\pi}{\Lambda_{i1}}, \frac{2\pi}{\Lambda_{i2}}, \dots)$, and $\boldsymbol{u}_{\mathbf{k}_\mathrm{i}}(\mathbf{r})$ is a standing wave with period $\mathbf{\Lambda}_\mathrm{i}$:

$$\boldsymbol{u}_{\mathbf{k}_\mathrm{i}}\ \mathbf{r} + n\mathbf{\Lambda}_\mathrm{i}\ = \boldsymbol{u}_{\mathbf{k}_\mathrm{i}}\ \mathbf{r}\quad \forall n = \pm1, \pm2, \dots$$

The dispersion curve $(\omega, \mathbf{k})$ is obtained by substitution of (20) in (19). The resulting system of differential equations can be resolved by Fourier expansion of the harmonic components of $\boldsymbol{u}_{\mathbf{k}_\mathrm{i}}(\mathbf{r})$ and $\eta\ \mathbf{r}$. One can then convert Helmholtz equations into a set of algebraic equations cast in the form of a matrix eigenvalue problem. The dispersion curve $(\omega, \mathbf{k})$ is never a continuous function of $\mathbf{k}$. This arises from the symmetries of the crystal. With no loss of generality, let us consider the case of a 1D PhC with periodicity along the z axis. Let us assume a wave propagating along z. Since we saw that k is periodic with a period $2\pi/\Lambda$, the problem can be studied in the range $k = [-\frac{\pi}{\Lambda}, +\frac{\pi}{\Lambda}]$. The origin of the discontinuities in $(\omega, \mathbf{k})$ lies in the special symmetry that emerges at the edges of the Brillouin zone when $= \pm\frac{\pi}{\Lambda}$, i.e. when the period of the waves in the crystal equals half the crystal period. The modes associated to $k = \pm\frac{\pi}{\Lambda}$ are $\mathbf{H}_{\pm\frac{\pi}{\Lambda}}\ \mathrm{z}$. These modes travel with the same wavenumber $\frac{\pi}{\Lambda}$ but in opposite directions. However, these modes are actually one and the same, since their Bloch numbers differ by a full period $\frac{2\pi}{\Lambda}$. In other words, at the edge of the Brillouin zone there are two Bloch periodic functions that are inverted version of one another: $\mathbf{u}_{+\frac{\pi}{\Lambda}}\ \mathrm{z}\ = \mathbf{u}_{-\frac{\pi}{\Lambda}}\ -\mathrm{z}$.

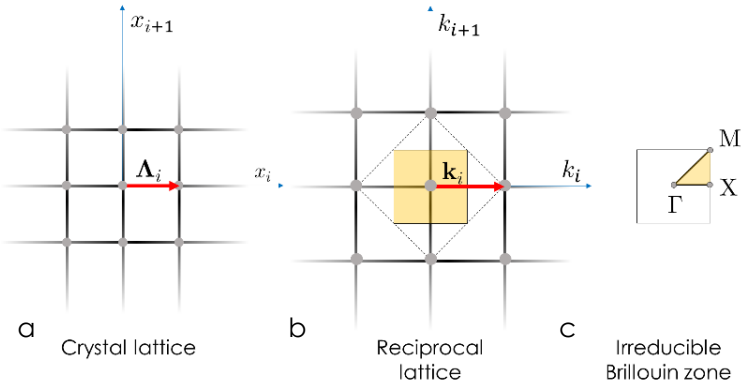

Figure 36 – **a**. Schematic of a crystal lattice and one lattice vector. **b**. Reciprocal lattice in the space of wavevectors. **c**. Irreducible Brillouin lattice.

These modes have the same spatial periodicity but – since the medium is inhomogeneous – they see different dielectric functions and therefore have different eigenvalues, i.e. distinct values of ω. This explains the discontinuity that arises as the dispersion curve crosses the boundary of the Brillouin zone (Fig. 37). This phenomenon can be more rigorously derived using the variational principle and showing that each pair of waves with $k = \pm\frac{\pi}{\Lambda}n$, $\forall n \in \mathbb{Z}$, have same wavenumber but distinct distributions of the displacement field $\mathbf{D}$ throughout the crystal. The range of angular frequencies that is not crossed by the dispersion curve because of this discontinuity is called bandgap. When the bandgap extends through all primitive vectors of the reciprocal Brillouin zone, then it is said to be complete. This is what prohibits, for example, blue light coming from any direction to travel through the PhCs on the butterfly wings and gives it its iridescent blue color.

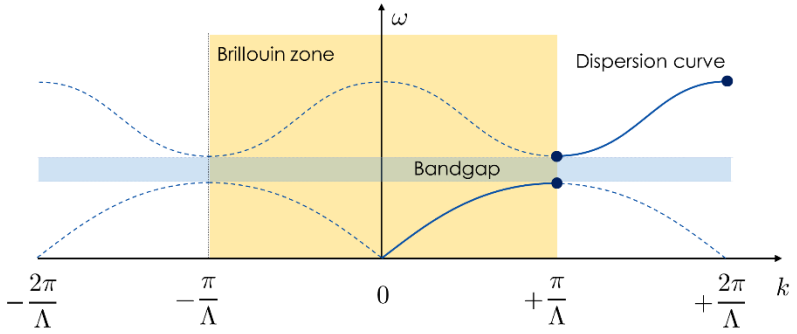

Figure 37 – Dispersion curve and band structure of a multivalued period dielectric function with period Λ.

The unique propriety of PhCs to present photonic bandgaps has been explored in nanotechnology for the fabrication of many powerful optical devices, such as point-defect and band-edge lasers[23,241], high-efficiency extractor for LEDs[242], waveguide with tight turns[243], PhC fibers[244], dispersion compensator[245], ultra-fast all-optical switches[246], Y-splitter[247], directional couplers[248], wavelength division MUX and DEMUX[249], PhC spectrometers[191], etc. Owing to the enormous range of functionalities that PhCs enabled, they have been vastly applied to a variety of other fields, particularly biology and medicine for the detection of different analytes with ultra-low detection limit as well as for several applications in sensing.[250-254]
Most of the applications for PhCs work with wavelengths in the range between 400 and 1500 nm and present a bandgap in one and two dimensions. In order to have a complete bandgap, PhCs with a 3D symmetry are required, which are very difficult to fabricate.[255] Moreover, to have a bandgap at visible wavelengths, a sub-wavelength lithography resolution must be used. The required resolution varies depending on the refractive index of the patterned medium, but it is usually sub-100 nm. This leaves no space for photolithography, except for the very expensive tools used in the semiconductor industry for microelectronics. PhCs for visible light are typically fabricated using EBL, which limits their application to research and prototyping because of the low throughput and expensive fabrication process. This is why scientists have recently explored NIL as a fast replication tool for PhCs. Here, we want to take this technology to the next level, and use our high RI sol-gel

material to cast PhCs without the need for pattern transfer. This sets very difficult challenges, since the loss of CD resulting from material shrinkage at high temperatures strongly affects the performance of the PhCs, unlike the case of the integrated photonic devices showed in paragraph IV.2. For this reason, we recently proposed a novel R-NIL approach to obtain high RI photonic structures with zero shrinkage.[256]
In the following paragraphs, the R-NIL fabrication process will be described and experimentally tested on the fabrication of PhCs in titania for light in the visible spectrum. The optical simulations and characterization of the printed PhCs are extensively discussed. Finally, to fully demonstrate the potential of this novel fabrication technique and validate it for the inexpensive fabrication of photonic devices, the performance of a PhC fabricated using EBL and that of a printed PhC are compared.

IV.3.2 R-NIL process for the fabrication of TiO_2 photonic devices without material shrinkage

Titania is one of the most promising materials for the fabrication of PhCs and PhC-based devices in the visible range due to its high RI and low extinction coefficient. Unfortunately, due to the difficulty to pattern TiO_2 and the high-resolution capability required, only a few devices have been so far demonstrated. PhCs in titania are typically fabricated using nanoparticles and other self-assembly techniques.[257,258] Only a limited the number of geometries can be fabricated using these approaches, which ultimately constrains the range of applications. Another technique consists of dip-infiltrating 2D and 3D porous, organic materials and biological samples in a titania sol-gel. The organic material is consequently removed by annealing process and a skeleton of TiO_2 remains.[255,257,258] This technique is very powerful since it allows 3D patterning. However, it is constrained to the availability of simple 3D materials and offer very low customizability over the PhC design. It is also a destructive technique, since the mold that is used to cast the photonic structure is irremediably lost after a single use. On the other hand, the direct-NIL process described in paragraph IV.2 for the fabrication of planar photonic devices in titania presents a severe shrinkage that hamper its applicability to PhCs. In case of integrated photonic devices, we saw that material shrinkage does not impair the performance of optical functions, since the photonic modes are confined inside a Si_3N_4 slab that is located beneath the patterned TiO_2. The same index-perturbation effect cannot be applied to the fabrication of PhCs in transmission, since the photonic modes must lay within the patterned PhC slab. This makes direct-NIL not suitable to the development of PhCs. We recently proposed a novel approach that consist of R-NIL. Figure 38 shows the steps that are needed to implement the R-NIL process. The mold is fabricated by EBL in HSQ on silicon, as described in paragraphs IV.2.1 and III.4. The depth of the mold is about 160 nm. Instead of conventional fluorosilane treatment, the mold is coated with gold to create a low energy surface and facilitate demolding. The use of fluorosilane does not allow the resist to fill the cavities of the mold in R-NIL. The sol-gel material is spin coated

on the mold and the PGMEA is evaporated through a soft bake at 100 °C for 1 min (Fig. 38a). The annealing is carried on a hotplate at 400 °C for 10 min (Fig. 38b). After annealing, the film inside the mold is extracted by reverse imprinting on a transparent substrate (glass) with the help of Ormostamp, which works as a glue for the TiO_2 film (Fig. 38c). The Ormostamp is cross-linked by UV light (Fig. 38d) and the mold is finally released, which results in a 160 nm thick PhC slab of TiO_2 on an Ormostamp layer (Fig. 38e). As opposed to direct NIL, here the material is annealed while it is still inside the mold, therefore mold reliefs delimit the material shrinkage, enabling a replication with a higher fidelity.

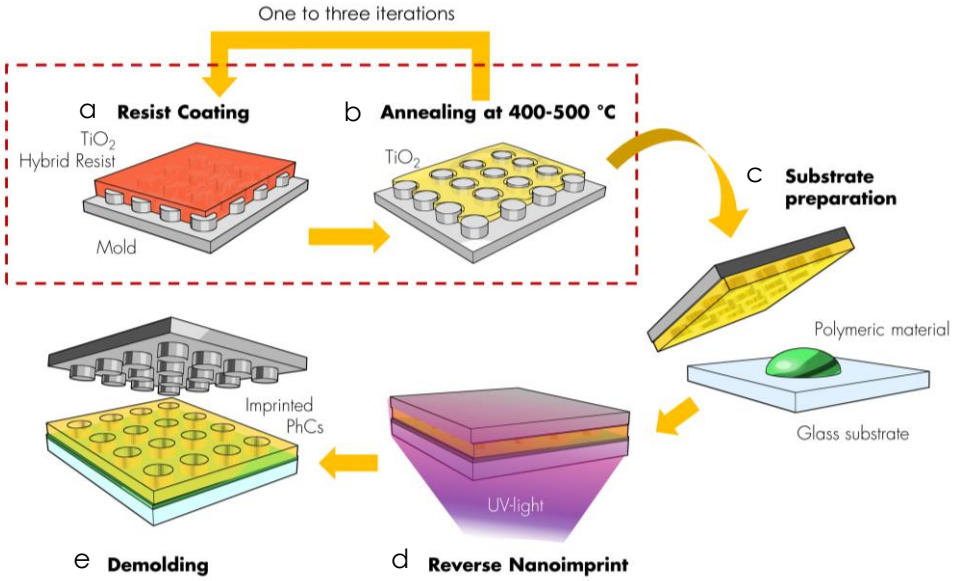

Figure 38 – Schematic of the R-NIL process for the fabrication of PhCs into our TiO2 sol-gel resin without material shrinkage.

Figure 39a shows a SEM cross-sectional image of the mold (bottom) and TiO_2 layer (top) after annealing (like in Fig. 38b). We found that the patterns still exhibit shrinkage, which indicates that conventional R-NIL is not sufficient to prevent loss of CD. To overcome this issue, steps *a* and *b* of the process in Figure 38 are repeated cyclically. At each cycle the hybrid material layer fills up the mold only partially. The mold is fully covered only after the entire sequence is repeated 3 times. Figure 39b shows a SEM cross-sectional view of this tri-layer coating that demonstrates how the cyclical implementation of the first two steps of the process allows conformal coating of the mold and preserves the critical dimensions (CD). This occurs because the material from following spin coatings fills the voids that were created during the annealing of previous layers. Figure 39c shows a SEM top-view of a square lattice PhC mold with a lattice constant $\Lambda = 355$ nm and a diameter $\varnothing = 173$ nm. The white dots are HSQ cylinders defined by EBL. Figures 39d and e show the PhCs that were obtained from imprinting the mold in Figure 39c with mono-layer and tri-layer R-NIL respectively. A statistical study was carried on these SEM images to

measure the variation of diameters and determine the loss of CD in PhCs that were imprinted with mono- and tri-layer R-NIL. For this purpose, SEM images of 500 holes within the same PhC in the mold and the two imprints were analyzed using myCD by aBeam Technologies Inc.[259]

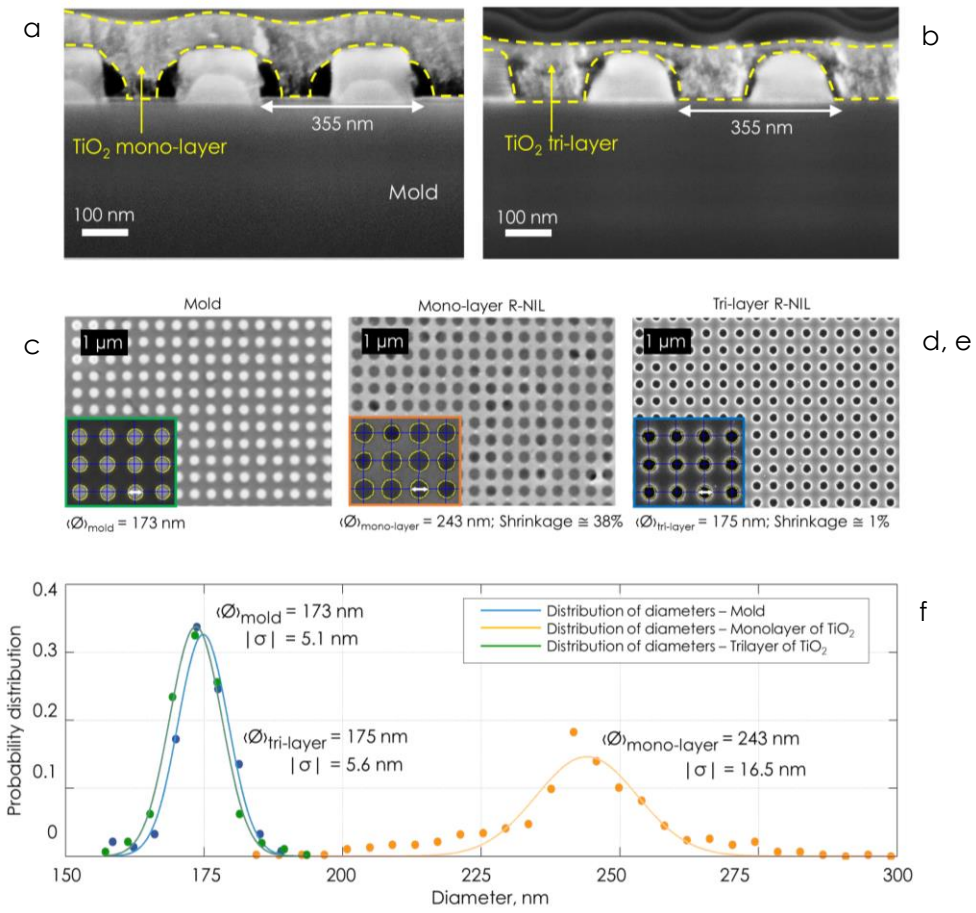

Figure 39 – Characterization of the R-NIL fabrication process. **a**. SEM Cross-sectional view of a mono-layer of TiO_2 material on the HSQ mold after annealing. The shrinkage is still present. **b**. SEM cross-sectional view of a tri-layer of TiO_2 material on the mold. Imprint in conformal with the mold protrusions. **c**. SEM top-view of the mold for a PhC having a lattice constant of 355 nm and a diameter of 173 nm. **d**. SEM top-view of the PhC imprinted by mono-layer R-NIL. **e**. SEM top-view of the PhC imprinted by tri-layer R-NIL. **f**. Distribution of diameters of mold, mono-layer and tri-layer R-NIL for the PhC in (c).

MyCD is a software that implements a physical model to simulate electron scattering during imaging and estimates quite accurately the actual sizes of patterns in SEM images. The insets in Figure 39c-e show the detection of PhC hole boundaries operated by myCD. Figure 39f plots the distribution of diameters that myCD returned for the PhC in Figures 38c-e. The PhC in the mold was found to have a Gaussian distribution of diameters with a standard deviation of 5.1 nm, and an average diameter of 173 nm. The PhC imprinted by mono-layer and tri-layer R-NIL have average diameters of 243 nm and 175, and standard deviations of 16.5 nm

and 5.6 nm respectively. The diameter distribution of the PhC that was replicated by tri-layer R-NIL is also very similar to that of the mold. From this data, a material shrinkage of about 38% is computed for the mono-layer R-NIL. This confirms that an improvement in material shrinkage can be obtained using typical R-NIL process. In fact, direct-NIL was always returning shrinkages above 50%. However, this still represents a huge loss of CD that cannot be tolerated in the fabrication of many photonic devices. Conversely, the tri-layer R-NIL returned an average diameter that is only 2 nm wider, which corresponds to a lateral shrinkage of only about 1%. This shows that our novel R-NIL approach enables the simple patterning of high-resolution TiO_2 photonic devices with a high fidelity.

IV.3.3 Optical characterization of printed PhCs

To complete the characterization of the proposed R-NIL process, optical measurements of mono-layer and tri-layer PhCs are performed and compared with simulations. Figure 40 is a low magnification microscope image of an array of printed PhCs taken in reflection under white light illumination conditions. The device comprises 550 PhCs with a square lattice, which were designed to exhibit resonance modes across the full visible spectrum. Each square is an array of several thousand holes with size 50×50 μm^2, which form one PhC. Each PhC has a uniquely identified lattice constant and hole diameter. These design parameters are varied with a step of 5 and 10 nm respectively, spanning 270 to 500 nm for lattice constant and 60 to 250 nm for diameter. The titania slab has a RI of about 2.05, whereas the Ormostamp layer and glass substrate have RI~1.50. Figure 40 shows that the position of the photonic bandgap can be easily tuned to span the entire visible spectrum, which generates different shades and colors of reflected light.
Simulations of the PhC resonances were performed by FDTD method in Lumerical with a three-dimensional model.[208] Let the PhC slab be the xy-plane, then incoming light wave is polarized along x and incident in z – all simulations and measurements are carried assuming an excitation at Γ point. The input wave was simulated as white light, i.e. a linear combination of plane waves with wavelength from 400 to 800 nm. The homemade setup for optical characterization reproduces the functioning of a confocal microscope with polarizers (Fig. 41a). Collimated white light is sent to a wire-grid polarizer and then from a 50 μm pinhole to a 10× objective that focuses it onto the PhC. Transmitted light from PhCs is collected via a 4× objective, passes through a second polarizer and is coupled to a spectrometer and a CCD camera. Low numerical aperture objectives ensures that the excitation waves are as similar as possible to plane waves. The bandgaps of the crystal can be identified in a cross-polarization measurement. Zero order from the transmitted light is cut off due to cross-polarization, while band-gap wavelengths scatter in all directions with random polarizations. Some of the scattered waves eventually couple inside the collection objective and are measured by the spectrometer. Figure 41b shows cross-polarization measurements of two PhCs imprinted by mono-layer and tri-layer R-NIL and the simulation of an ideal PhC.

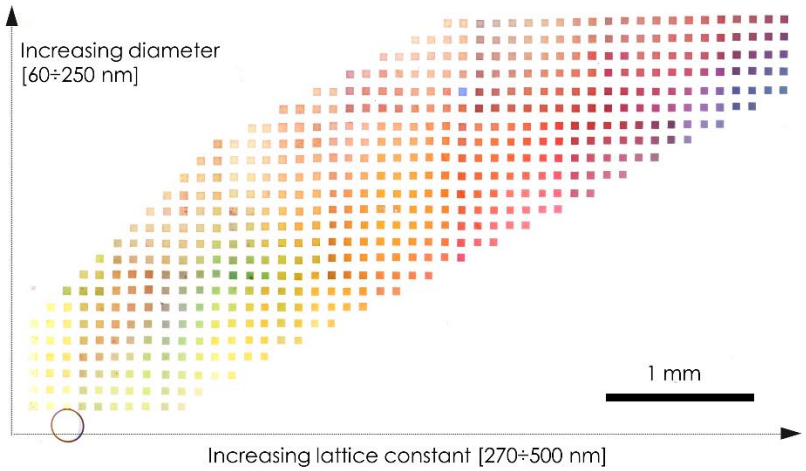

Figure 40 – Low-magnification image of the imprinted device, taken in a reflection microscope with white light illumination. The different structural colors corresponds to different photonic bandgaps in the visible range.

The lattice constant and nominal diameter of the simulated PhC are 355 nm and 173 nm respectively, which are extracted from the SEM of the mold in Fig. 39c, while the measured curves refer to the replicated crystals in Fig. 39 d and e. In Fig. 41b the simulation (red line) shows that only waves with $\lambda = 562$, 577 nm are prevented from going through the crystal. The performance of the PhC imprinted by tri-layer process (bluedotted curve) is very similar to that of the ideal PhC. The resonances in the monolayer imprint are blue-shifted compared to the tri-layer R-NIL. This is due to the 38% material shrinkage that reduces the width of dielectric veins between crystal holes. Both tri-layer and mono-layer PhCs show broader resonances compared to the ideal PhC from the simulation. Figure 41c demonstrates that such a mismatch in resonance width depends on the varied distribution of hole diameters. The figure compares the simulation of an ideal PhC and one that has a distribution of holes like in Fig. 38f. Calculations shows that a Gaussian distribution of diameters results in the enlargement of PhC resonances and loss of efficiency, which is what we have partially observed in the measurement of a printed PhC with similar feature size (Fig. 41c). Some incongruences are still observed in the measurement of the resonance peak at shorter wavelengths. These differences between simulation and measurements are attributed to small misalignments of the beam in the optical setup. In fact, we noticed a strong dependence of the resonance peak from the angle of incidence and collection of light, as well as for its polarization. This is expected from theory, which predicts different behaviors for different wave vectors propagating through the crystal (see paragraph IV.3.1).
Figure 42a shows a 10 nm resonance shift in two PhCs that have a pitch difference (lattice constant difference) of only 5 nm.

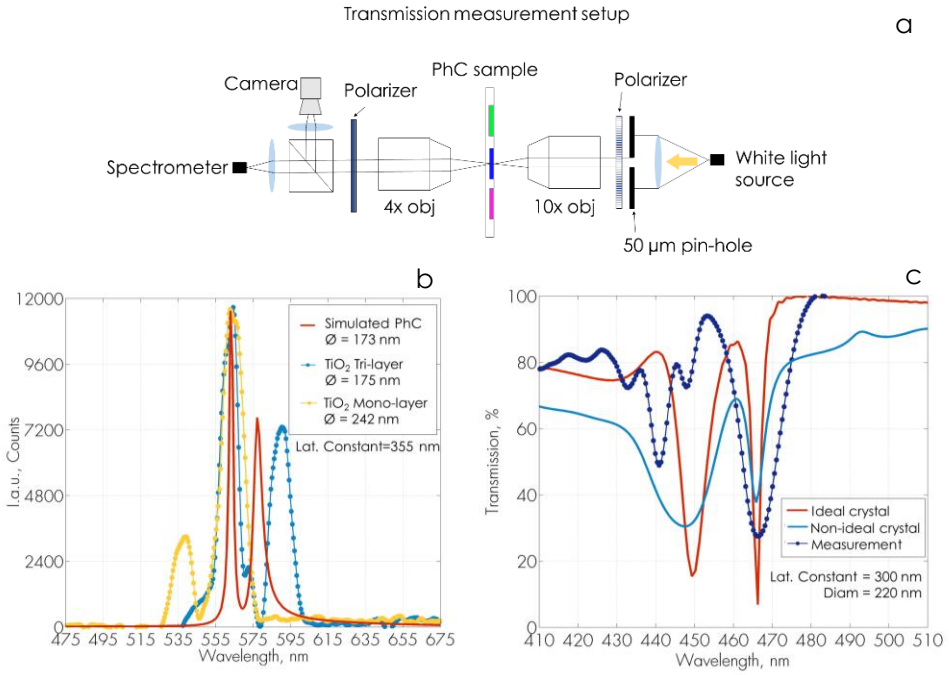

Figure 41 – **Comparison between simulation and optical measurements of PhCs. a**. Schematics of the optical setup used to measure the PhCs response in transmission and cross-polarization. **b**. Cross-polarization measurement of a theoretical and two PhCs that are imprinted by mono-layer and tri-layer R-NIL. **c**. Transmission measurement of a printed PhC (tri-layer R-NIL) compared to a simulated ideal and non-ideal PhC.

Such a shift is predicted by simulation, which indicates that the tri-layer R-NIL process provides a lithography accuracy of about 5 nm. Figure 42b proves that the photonic bandgap can be tuned across the entire visible spectrum by varying lattice constant and diameter of the crystals. These diagrams plot the complementary spectra of the structural colors shown in Fig. 40. Finally, Figure 42c compares transmission spectra of an imprinted PhC and another crystal that was fabricated into Si_3N_4 by EBL and etching. The fabrication of the Si_3N_4 PhC is similar to that of the DPH benchmark device that was described in paragraph III.5. A similar distribution of diameters with an average of 220 nm and standard deviation 6 nm was also measured in the Si_3N_4 PhC. To achieve a spectral overlap of the responses from the two crystals, the lattice constant and diameter of the Si_3N_4 PhC was properly tuned. Figure 42c shows that the spectral responses of the two devices are very similar. They exhibit inverted coupling efficiencies in the air- and dielectric modes that are responsible for the reversed peak intensities at 445 and 465 nm. Imprinted titania is also more transparent than the Si_3N_4 deposited by PECVD over most part of the visible spectrum. This demonstrates the excellent optical properties of our sol-gel material for photonic application in transmission mode. The overall performance of the PhCs printed by tri-layer R-NIL are in good agreement with the simulation and well compare to the optical behavior of a similar device that is fabricated by EBL. The results shown here also validate our tri-layer R-NIL process

for the single-step fabrication of photonic devices into a high-refractive index material for visible light applications.

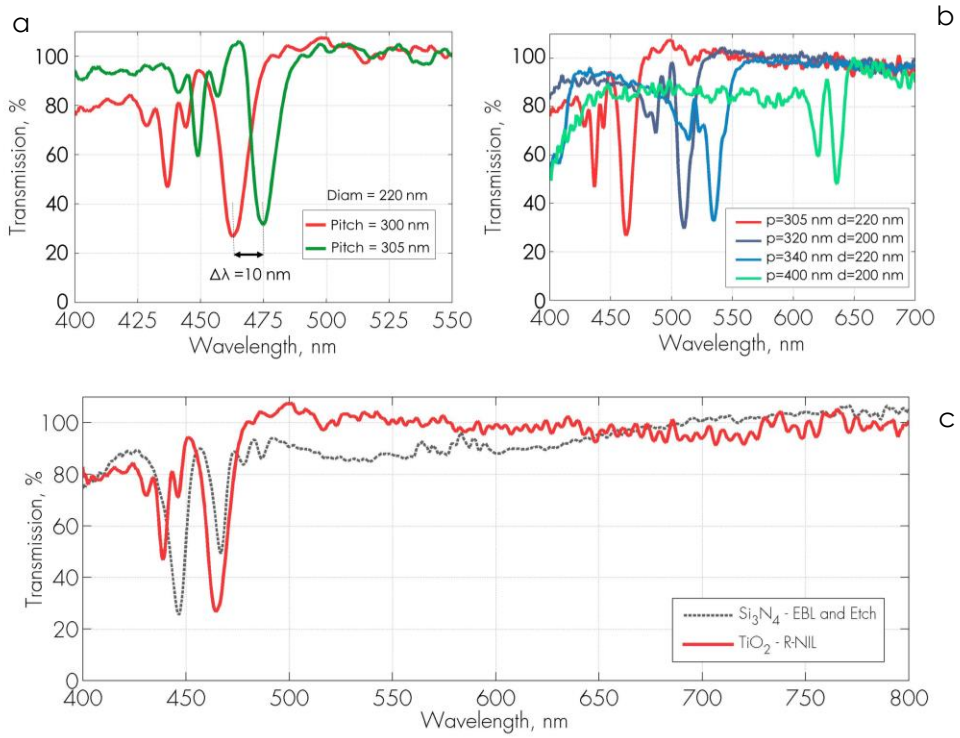

Figure 42 – **Transmission measurements of imprinted PhCs**. **a**. Fine control in the position of the resonance implies great accuracy (sub 5 nm) of the imprinted patterns, which can be achieved only thanks to a shrinkage-less process. **b**. Optical resonances of the imprinted PhCs can cover the entire visible spectrum. **c**. Comparison between an imprinted PhC and one that is fabricated by EBL and etching into silicon nitride.

Conclusion and perspectives

Summary of the thesis

The purpose of this work was to research and evaluate novel nanofabrication technologies, materials and device concepts to support and innovate the fields of photonics and nanotechnology. Advancement in both these fields is progressively enabling the discovery of unprecedented proprieties of interaction between light and nanostructured matter. The new capabilities offered by photonics (see paragraph I.3) are expected to revolutionize the world we live in. New powerful sensors, detectors, lasers, more efficient light harvesters and emitters, flexible displays, faster cable communication and others are just a speckle of the profound changes fueled by photonics. In little more than one year we will be immersed into a world of virtual and augmented reality, where new headsets and visors will assist and improve our life experience. Although this is all coming towards us, technology constraints still exist that either limit the applicability of these discoveries or hamper the research for more. The focus of this thesis was to propose and investigate new technologies and materials that can enable the inexpensive and scalable fabrication of photonic devices for application in the visible light spectrum. The main challenges associated with the fabrication of devices for the manipulation of visible light concern the need for high lithography resolution and the research for suitable materials. Only a few lithography techniques to date meet all of the technology requirements for the fabrication of photonic devices. Unfortunately, these techniques are either too expensive for high volume manufacturing (EBL) or very hard to access at affordable costs (photolithography tools in semiconductor plants).
NIL was analyzed here as a suitable, versatile, low-cost lithography solution for photonics. To demonstrate and advance the potential of printable photonics two research themes were explored in parallel. The first concerned the development and testing of NIL technologies on the fabrication of progressively more complex devices, from planar integration (Chapter III) to PhCs in transmission and off-the-plane coupling (Chapter IV). The ongoing research discussed in the next pages will fulfill this theme with the demonstration of three-dimensional photonics/plasmonic structures by NIL (currently in progress). The second research theme concerned the use of materials science to couple bottom-up chemical functionalities offered by synthetic materials, i.e. high refractive index, with top-down NIL patterning. The development of these research themes led to the implementation of different NIL techniques for the imprint of novel photonic devices with both purely organic NIL resists and a hybrid, organic-inorganic, functional sol-gel material.

Achievements

This report provided a thorough introduction of photonics (Chapter I) and nanoimprint (Chapter II). A critical literature review supported the discussion about the state of the art, achievements, and future perspectives of both fields. Paragraph II.5 finally merges these two fields and put forward the idea of printable photonics. An analytical model was derived that describes the pattern filling during imprint in NIL processes that are dominated by capillary effects, such as those used in this work. The model provided support data to understand the rheological mechanisms that occur at the nanoscale during imprint. The model was applied to the fabrication by SR-NIL of a complex photonic device for on-chip spectroscopy. The integrated spectrometer was designed based on DPH technology. The physical and mathematical description of DPH was thoroughly derived and discussed. Simulations of all of the optical components that are integrated into the spectrometer chip were provided and commented (RWGs, input taper, directional coupler and waveguide TE-polarizers). The formulation of a novel organic imprint polymer for SR-NIL was tested on the fabrication of the integrated spectrometer and a yield of 73% over 180 devices was determined by metrology investigations of the imprinted dies. This is a relatively high yield, considering that results were obtained in a research facility. Imprinted DPH devices were etched into the core of a Si_3N_4/SiO_2 planar waveguide. A number of imprinted chips undertook a thorough optical characterization. The results of the characterization were compared and contrasted with that of an identical device that was fabricated by EBL and used as a benchmark. In average, the optical performance of the imprinted photonic devices – i.e. spectral resolution, DPH reflectivity and RWG losses – align very well with optical simulations and are similar to that of the EBL chip. The spectrum of a laser that emits below threshold was measured by both an imprinted DPH chip and a commercial spectrometer. The spectral readings from the two spectrometers are in very good agreement, which validates DPH technology for on-chip spectroscopy. More importantly, this shows the reliability of SR-NIL to successfully fabricate integrated photonic devices.

The potential of NIL discussed in Chapter III were brought to the next level in Chapter IV, where the one-step fabrication of two distinct photonic devices was demonstrated by direct and reverse NIL of a novel hybrid organic-inorganic sol-gel material, based on TiO_2. With this application we are moving towards coupling top-down capabilities of NIL with bottom-up functionalities offered by materials science. Our sol-gel material was tested on the single-step imprint of a DPH device for optical demultiplexing on the core of a Si_3N_4/SiO_2 planar waveguide. After imprinting, the patterned material is annealed at over 400 $^{\circ}$C. Heat degrades the organic phase of the hybrid polymer and leaves polycrystalline patterned titania structures. This comes at a cost of a severe structural shrinkage ($>$50%). However, we demonstrated that the shrinkage does not impair the optical performance of the printed devices. The small refractive index perturbation operated by the nano features of TiO_2 on the surface of Si_3N_4 proved sufficient to generate guided modes inside the Si_3N_4 layer.

In fact, printed titania is only used here to guide light, and all optical modes are hosted mostly within the nitride. Printed RWGs showed losses of about 40 dB/cm, which are aligned with experiments of other research groups on fabrication of RWGs in TiO_2 by EBL and etching. The performance of the imprinted four-channel DPH wavelength demultiplexer are also in good agreement with simulations.
In order to move progressively towards less planar printable devices, the step from in-plane to out-of-plane coupling is required. To achieve this, two-dimensional PhCs were printed into our functional material by means of a novel R-NIL process. The PhC devices differ from the DPH demultiplexer on that the guided modes lay within a thick layer of patterned TiO_2 material and light coupling occurs out of the imprint plane. R-NIL was designed to reduce material shrinkage during annealing, and enable a high lithography fidelity, avoiding loss of CD. In fact, while integrated devices proved robust against material shrinkage, any CD loss would dramatically impair the optical performance of the PhCs, shifting resonances or preventing the fabrication. A layout that contains 550 PhCs with optical resonances that span the entire visible range was imprinted. The specifically designed R-NIL process reduced material shrinkage from over 60% to only about 1%. The PhCs were characterized with off-the-plane excitation and collection at the Γ point of the crystal. Both transmission and cross-polarization measurements of the PhCs overlap quite well with simulations. The transmission spectra of an imprinted PhC is compared to that of a similar PhCs in Si_3N_4 that was fabricated by EBL. Again, the performance of the imprinted PhCs are in very good agreement with that of the EBL chip.
The encouraging outcomes that were attained with all of the different photonic devices prove the disruptive potential of printable photonics as a low cost, high-throughput and potentially high-yield technology for future optical devices. The application of digital holography for the manipulation and control of visible light in the spatial and spectral domain can offer unprecedented optical functions to the field of fiber optic communication, optical interconnects, and bio-sensing. At the same time, the single-step imprinting of a high refractive index functional material can enable inexpensive manufacturing of photonic devices at all stages of technology development, from R&D to volume production.
The variety and complexity of processes, materials and photonic structures that were explored in this work allow us to confidently stretch the validity of these results to include many other photonic components. In fact, research on this topic is still progressing towards the exploration of more complex device concepts with yet more embedded functionalities.

Ongoing research

Certainly the next step in lithography is 3D. Even for photonics, 3D structures would allow the full exploitation of photonic effects and break ground for an even broader range of devices and applications. Many groups have started the exploration of the 3D patterning with relatively good results. Unfortunately, currently explored techniques are either too slow (two-photon lithography), or not sufficiently flexible

to achieve custom patterning (holographic and interference lithography). The other drawback of photon-based lithography techniques is that they can hardly reach diffraction limited resolutions. Even here, NIL seem to be the most suitable technology in terms of throughput, cost, and resolution. Three-dimensional patterning by NIL can be attained by a layer-to-layer fabrication. Overlay accuracy of state-of-the-art imprint tools is now about 5 nm (see paragraph II.4), which is well within tolerance for devices that work in visible wavelengths.

Our scientific endeavors are currently oriented in very much the same direction, with the goal of advancing the research in printable 3D photonics and extend the spectrum of applications. After demonstrating the feasibility of NIL on planar photonics for planar devices and PhCs in transmission, our main focus is technology development for the imprint of 3D (or quasi-3D) structures onto the facet of optical fibers. This would offer unique opportunities for probing and sensing due to inherently coupled optical functionalities onto a fiber tip. The technological challenges presented by this development are enormous, beginning with the mechanical handling and patterning of an optical fiber as a substrate that is smaller than 125 μm in diameter. The imprinted structures also require a fine alignment to the fiber core and control of the imprint residual layer. With this line of work we are targeting the fabrication of fiber-coupled plasmonic probes for near-field scanning optical microscopy (SNOM). As the SNOM probe we chose to pattern a Campanile tip.[260] Campanile consists of a fiber-coupled pyramidal optical transformer that squeezes light adiabatically below the diffraction limit, allowing for high efficiency and enhancement of the electric field at the nanoscale. This SNOM probe is emerging as a powerful characterization tool in materials science and it has already enabled important scientific breakthroughs.[261,262] The Campanile probe has been fabricated by FIB so far, with very low throughput and yield, which has limited its widespread use in nanoimaging. Thanks to the unique capability of NIL on the fabrication of quasi-3D structures in one step, we demonstrated that the complex geometry of the campanile can be stamped directly onto a fiber facet. The Campanile mold is fabricated by grayscale Gallium milling and contains micron to nanometer size features over a 3D structure (Fig 43a). The imprint on the fiber with a good control of the residual layer is successfully performed. A gold layer is selectively evaporated onto two faces of the imprinted Campanile, leaving a sub-50 nm plasmonic gap at the apex of the pyramid, which creates the required plasmonic enhancement. Preliminary near-field measurements of Perovskite samples performed by printed Campanile tips prove the presence of sub-diffraction heterogeneities in the emitted photoluminescence (Fig 43b). This validates the imprinted tips and paves the way for the low-cost, high-throughput fabrication of fiber-optics SNOM probes by NIL. This achievement has potential to boost the research in materials science and discovery of new fundamental properties of light-matter interaction.

This research line targets the advancement of top-down technologies towards three-dimensionality and higher lithography versatility, and follows the same path that was explored in this thesis with the development and testing of SR-NIL, direct and reverse NIL processes.

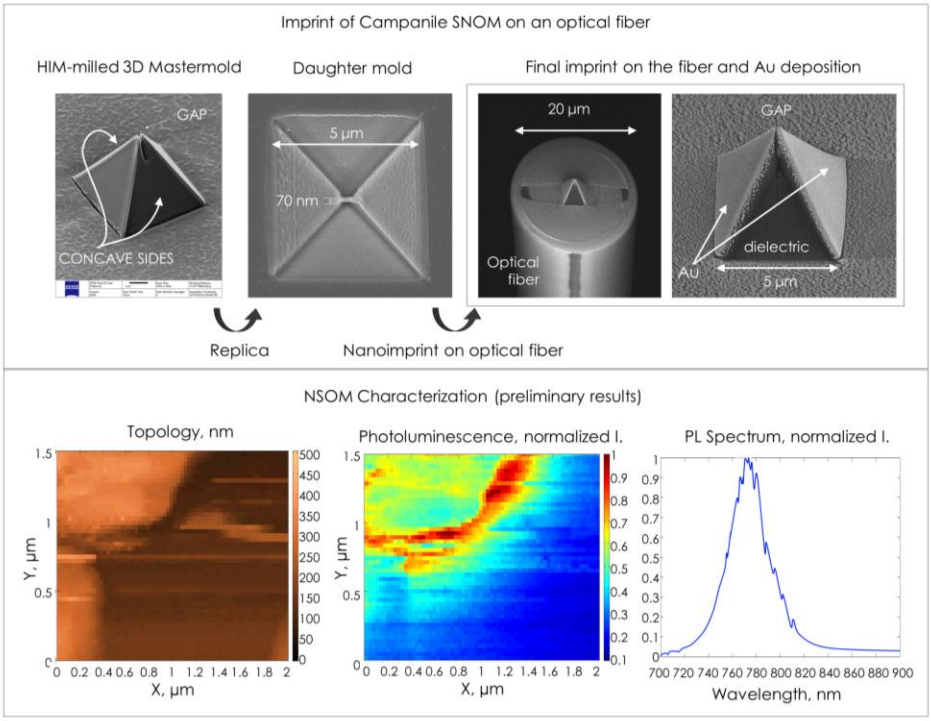

Figure 43 – Campanile near-field probe fabricated by imprinting on an optical fiber. a. The 3D mastemold is fabricated by embossing and 3D Gallium milling and a daughter mold is obtained by NIL replication. The daughter mold is used to imprint the 3D structure onto a fiber and metal evaporation completes the fabrication process, leaving a sub-50 nm gap on the apex of the pyramid, which creates a plasmonic enhancement of the electric field. **b**. Preliminary results from SNOM measurements of a Perovskite sample shown sub-diffraction PL features, which clearly indicate that our printed Campanile probe is working.

However, the development of new material functionalities from bottom-up approaches also proceeds with the embedment of a gain medium inside the TiO_2 sol-gel material for the formulation of a photoluminescent, high-refractive index imprintable resin.[263] After demonstrating the single-step patterning of passive PhCs, the direct printing of active 1D PhC cavities for a nano-laser array is currently being researched. For this purpose, thermally stable quantum dot nanocrystals were synthesized and functionalized with organic ligands that allowed the incorporation into our sol-gel material. Printing of 2D PhCs with our active polymer showed that high resolution photonic structures with an integrated gain medium can be achieved. Figure 44 shows the preliminary results from photoluminescence (PL) mapping of the printed photonic devices without (left) and with embedded QDs in the high RI material. In the chip with QDs we notice an enhancement of the PL emission within the patterned medium, which is due to the higher density of photonic states. This paves the way for the inexpensive fabrication more advanced photonic devices, which include optically pumped nanolasers and high-efficiency LEDs.
To conclude, in this thesis we walked through the recent advancements in the field of printable photonics, ranging from integrated holographic devices for on-chip spectroscopy to imprintable photonic crystals for visible light applications.

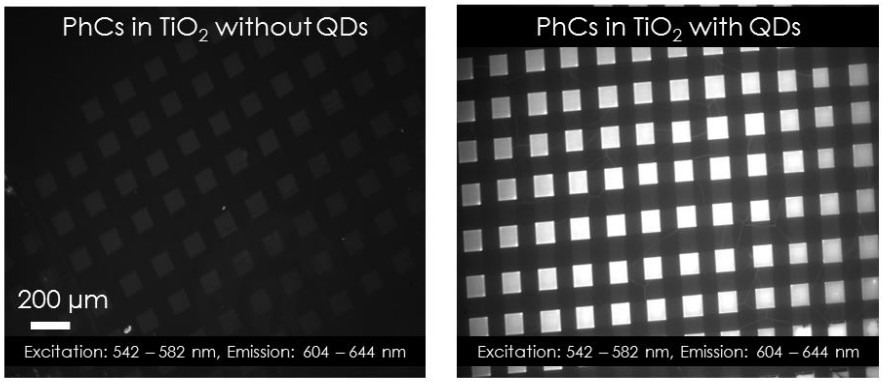

Figure 44 – PL mapping of an imprinted photonic device without (left) and with (right) embedded QDs. The presence of a high PL emission within the patterned PhCs compared to the background implies a strong interaction between the gain medium and the photonic resonators.

In doing so, we studied, tested and evaluated different imprint technologies and novel photonic devices. The brief overview of the ongoing research provides perspectives that go beyond the planar integration of photonics, with the fabrication of three-dimensional photonic and plasmonic structures and the embedment of more optical functionalities into imprintable materials. The arguments and scientific evidences that were delivered throughout this thesis clearly illustrate the potential of printable photonics to support both scientific and technological innovation. Printable photonics is expected to increasingly enable new exciting discoveries that will certainly improve our lives and lead us towards a future full of (visible) light.

Appendix **A** – Derivation of an analytical model for the resist flow and pattern filling in SR-NIL

The results of the calculations reported here are discussed in Paragraph II.3. The nomenclature used in the formulas below refers to Figure 6. The assumptions used in the physical study of the resist flow behavior in nanometer size protrusions for SR-NIL are reported below:

1) Resist is a Newtonian liquid.
2) Resist is incompressible.
3) Viscosity of the resist does not depend on the fluid velocity and gap of the channels.
4) Henry's constant of the air with the polymer (solubility of trapped air into the resist) does not depend on the pressure.
5) Diffusion of air into the polymer is ruled by Henry's law, so concentration of air in the resist only depends on the pressure of the trapped air and no saturation ever occurs.
6) No species diffuse from the polymer to the trapped air in the trench, so only diffusion of air into the resist is considered.
7) Effect of the meniscus in the capillary rise is not considered.
8) The process is isotherm.

We start by modelling the resist behavior as a Poiseuille flow along x between two parallel plates that have perfect no slip boundaries and are separated by a gap h:

$$v_x = \frac{\partial P}{\partial x}\frac{1}{2\eta}(z^2 - h^2) \tag{21}$$

As described by equation (21), the cross-section of the flux is parabolic, faster in the center and still at the boundaries. The volumetric flow rate is given by the integral of the velocity across the gap, times W:

$$\frac{dV}{dt} = W\int_{-h}^{0} v_x(z)dz = \frac{\partial P}{\partial x}\frac{W}{2\eta}\int_{-h}^{0}(z^2 - h^2)dz \rightarrow \frac{dV}{dt} = -\frac{\frac{\partial P}{\partial x}}{3\eta/Wh^3} \tag{22}$$

Formula (22) links the velocity of the flow directly to the pressure differential along the channel and inversely to a term which represents a lumped resistance per unit length. Figure 6b describes the filling mechanisms of an infinitely long trench along z as the combination of two flows are along x. Using an electrical equivalent of this fluid dynamic system and formula (22), the lumped model in Figure 6b can be drawn. The lumped resistance per unit length R_1 and R_2 depend on the channel widths L and *h(z)*. L is constant, while *h(z)* decreases as the mold sinks into the resist:

$$R_1 = \frac{3\eta}{Wh(z)^3}$$
$$R_2 = \frac{3\eta}{WL^3}$$

Using the electric equivalent, lumped resistance formulas, and equation (22), the following model for the capillary rise can be derived:

$$\frac{dV}{dt} = \frac{1}{0.5R_1 + R_2}\frac{\partial P}{\partial z} = \frac{1}{\frac{3\eta}{W}\left(\frac{1}{2h^3} + \frac{1}{L^3}\right)}\frac{\partial P}{\partial z} \rightarrow$$

$$\frac{dz}{dt}WL = \frac{1}{\frac{3\eta}{W}\left(\frac{1}{2h^3} + \frac{1}{L^3}\right)}\frac{\partial P}{\partial z} \rightarrow \frac{dz}{dt} = \frac{1}{3\eta\left(\frac{L}{2h^3} + \frac{1}{L^2}\right)}\frac{\partial P}{\partial z}$$

$$\frac{dz}{dt} = \frac{\Delta P}{3\eta z\left(\frac{L}{2(h_0 - \frac{L}{p}z)^3} + \frac{1}{L^2}\right)} \tag{23}$$

The contact between the mold and substrate occurs at $t = 0$, and $z(t)$ indicates the height of the capillary rise inside the trench, so $z\ 0\ = 0$ and $z\ \infty\ \rightarrow d$. ΔP is the total pressure difference, which is equal to the Laplace pressure (ΔP_c), plus the imprint pressure (P_i), minus the pressure difference in the air gap between the resist meniscus and the top of the trench (ΔP_g). This is equal to the inner pressure of the gap and the external atmospheric pressure $\Delta P_g = P_g - P_{atm}$. Thus, ΔP is equal to:

$$\Delta P(z) = \Delta P_c - \Delta P_g(z) + P_i \tag{24}$$

When the imprint is just about to start, $\Delta P_g = 0$, since $P_g = P_{atm}$. At $t = 0$, $\Delta P \gg 0$, also $h\ z\ = h_0$ which is the thicker the gap will ever be, opposing the lowest resistance to the liquid flow. So, right after the contact ($t = 0^+$) the resist is dragged upward very fast, but as this goes, the air inside the trench is compressed and ΔP_g increases. In J-FIL the resist reaches the top of the trench immediately and the air is pushed transversally[110] (along y in Fig. 6b). Instead, here the air is trapped at the top of the trench and it can only be absorbed by the resist beneath. The process of absorption is described by Henry's Law:

$$\mathrm{c}_r\ z\ = H^{cp}\Delta P_g\ z \tag{25}$$

Where H^{cp} is the Henry's constant, or solubility, and c_r is the concentration of air in the resist. Henry's law defines the concentration of gas in a fluid at regime based on the relative pressure of the gas, but does not provide information about the dynamics of the diffusion over time. Johannsen *et al* first described the transient of

a diffusion mechanism with an exponential formula[264,265], which depends on the empirical diffusion time constant β. If we apply a similar formula to our system, we get:

$$c_r = \beta H^{cp} \int_0^{\infty} e^{-\beta\tau} P_g \ t-\tau \ d\tau - H^{cp} P_{atm} \tag{26}$$

Now, consider the ideal gas law:

$$P = \mathrm{c}RT \tag{27}$$

Where R is the ideal gas constant and T is the temperature (in Kelvin). If we apply the principle of conservation of mass to our system we get:

$$c_g V_g + c_r V_r = c_0 V_0 \tag{28}$$

Where V_g and V_r are the volume of the air in the gap and resist, respectively. $V_g = (d-z)LW$, while $V_r = ph_0$. V_0 is the volume occupied by the air at the time $t = 0$, and it is equal to $V_0 = Ld$. Merging the result from equations (26-28), the time evolution of $\Delta P_g \ z \ $ can be written as:

$$\Delta P_g \ z \ = \frac{P_{atm}(zL + H^{cp}RTph_0) - \beta ph_0 H^{cp} RT \int_0^{\infty} e^{-\beta\tau} P_g \ t-\tau \ d\tau}{d-z \ L} \tag{29}$$

Putting together equations (1), (23) and (29), we obtain a model for the kinetic filling of the infinitely long grating shown in Fig. 6:

$$\frac{dz}{dt} = \\ = \frac{P_i + \frac{2\gamma\cos\theta}{L} - \frac{P_{atm} \ zL + H^{cp}RTph_0 \ - \beta ph_0 H^{cp} RT \int_0^{\infty} e^{-\beta\tau} P_g \ t-\tau \ d\tau}{d-z \ L}}{3\eta\left(\frac{Lp}{2\left(h_0 - \frac{L}{p}z\right)^3} + \frac{z}{L^2}\right)} \tag{30}$$

The analytical model of the filling process is an integro-differential equation whose explicit solution is very complicated to attain. Equation (30) is solved with numerical, iterative, methods in MATLAB. Results are plotted in Figure 7.

Appendix **B** – Model of a Distributed Bragg Reflector based on Matrix Optics

The calculation of the DBR reflectance is performed here in case of perpendicular propagation of light across the DBR. The notation in the formulas below recall Figure 11 from paragraph III.2.1. Based on matrix optics, an optical system can be modeled as a matrix having two inputs and two outputs waves, which represent backward and forward propagations:

$$\begin{bmatrix} U_{i+1}^{+} \\ U_{i+1}^{-} \end{bmatrix} = \mathbf{M}_i \begin{bmatrix} U_{i}^{+} \\ U_{i}^{-} \end{bmatrix}$$

The wave-transfer matrix of the elementary cell $\mathbf{M}_i$ is:

$$\mathbf{M}_i = \begin{bmatrix} \dfrac{1}{t_i^*} & \dfrac{r_i}{t_i} \\ \dfrac{r_i^*}{t_i^*} & \dfrac{1}{t_i} \end{bmatrix} \tag{31}$$

where t_i and r_i in (31) are complex transmittance and reflectance coefficients, such that $\mathcal{T}_i = |t_i|^2$ and $\mathcal{R}_i = |r_i|^2$ are the intensity transmittance and reflectance of the i-th pair. The DBR can be seen as a repetition of an elementary cell formed by a pair of layers with different refractive indexes, with wave-transfer matrix $\mathbf{M}$ (Fig. 11). We assume two matched media at the extremes of the grating and N equal pairs, so the overall wave-matrix $\boldsymbol{\mathcal{M}} = \prod_{\boldsymbol{i=1}}^{N} \mathbf{M_i} = \mathbf{M}^N$. Since $\det(\mathbf{M_i}) = 1$, it is easy to demonstrate that this equation can be simplified as

$$\boldsymbol{\mathcal{M}} = \mathbf{M}^N = \Psi_{\mathrm{N}}\mathbf{M} - \Psi_{\mathrm{N-1}}\mathbf{I} \tag{32}$$

where

$$\Psi_{\mathrm{N}} = \frac{\sin\ N\phi}{\sin\ \phi} \tag{33}$$

and

$$\cos\ \phi\ = \mathfrak{Re}\left\{\frac{1}{t}\right\} \tag{34}$$

From (31) and (32) we see that

$$\boldsymbol{\mathcal{M}} = \mathbf{M}^N = \begin{bmatrix} \dfrac{1}{t_N^*} & \dfrac{r_N}{t_N} \\ \dfrac{r_N^*}{t_N^*} & \dfrac{1}{t_N} \end{bmatrix} = \begin{bmatrix} \Psi_{\mathrm{N}} \dfrac{1}{t^*} - \Psi_{\mathrm{N-1}} & \Psi_{\mathrm{N}} \dfrac{r}{t} \\ \Psi_{\mathrm{N}} \dfrac{r^*}{t^*} & \Psi_{\mathrm{N}} \dfrac{1}{t} - \Psi_{\mathrm{N-1}} \end{bmatrix} \tag{35}$$

In (35) r and t are the complex reflection and transmission coefficients respectively of an elementary pair of layers. From the above equation, t_N and r_N can be obtained as function of the elementary coefficients r and t, thus overall transmittance and reflectance of the DBR are

$$\mathcal{T}_N = \frac{\mathcal{T}}{\mathcal{T} + \Psi_{\mathrm{N}}^2 (1 - \mathcal{T})}$$

$$\mathcal{R}_N = \frac{\Psi_{\mathrm{N}}^2 \mathcal{R}}{1 - \mathcal{R} + \Psi_{\mathrm{N}}^2 \mathcal{R}} \tag{36}$$

Considering layer thicknesses of d_1 and d_2 (Fig. 11), from Fresnel equations we have that:

$$\mathcal{R} = \left(\frac{n_1 - n_2}{n_1 + n_2} \right)^2 \tag{37}$$

$$\mathfrak{Re}\left\{ \frac{1}{t} \right\} = \frac{n_1 + n_2}{4 n_1 n_2}^2 \cos(\varphi_1 + \varphi_2) - \frac{n_1 - n_2}{4 n_1 n_2}^2 \cos(\varphi_1 - \varphi_2) \tag{38}$$

where $\varphi_1 = n_1 k_0 d_1$ and $\varphi_2 = n_2 k_0 d_2$ are the phases introduced by the two layers in an elementary cell. With simple geometrical considerations, the following formulas can be demonstrated:

$$\varphi_1 + \varphi_2 = k_0 \; n_1 d_1 + n_2 d_2 \; = \pi \nu / \nu_B \tag{39}$$

$$\varphi_1 - \varphi_2 = \frac{n_1 d_1 - n_2 d_2}{n_1 d_1 + n_2 d_2} \pi \nu / \nu_B \tag{40}$$

with the Bragg frequency ν_B equal to

$$\nu_B = \frac{c_0}{2 n \Lambda} \tag{41}$$

where the effective RI $n = (n_1 d_1 + n_2 d_2)/\Lambda$ is calculated as the spatial average of the refractive indexes weighted by their thicknesses within one period Λ.[††] Combining equations (33) to (40) the frequency dependent reflectance of the DBR, $\mathcal{R}_N(\nu)$, is attained in a closed form and plotted in Figure 12a.

If we want to calculate $\mathcal{R}_N(\nu)$ in case of apodized grating, the wave-transfer matrixes of our DBR are all different and the simplification reported in (32) is not true. To calculate the response of an apodized DGR we can obtain the overall wave-transfer matrix of the DGR as:

$$\boldsymbol{\mathcal{M}} = \prod_{i=1}^{N} \mathbf{M}_{\mathrm{i}} \left(n_1 \ i \ , n_2 \ i \ \right) \tag{42}$$

where $n_1 \ i$ and $n_2 \ i$ are the refractive indices of the i-th pair of layers. To modulate the refractive index contrast we can keep one index constant and change the other. A commonly used window function in apodization processes is the raise-cosine:

$$n_1 = n_2 + \Delta n \left\{ a \left[2 + \cos\left(\pi \frac{N-1 \ -2i+2}{N-1} \right) \right] - 1 \right\} \tag{43}$$

where $a = [0,1]$ is the apodization factor. Figure 12f shows the apodization functions for five values of a, from no apodization to a fully apodized grating. The complex reflectance and transmittance coefficients for each individual wave-transfer matrix can be calculated from Fresnel equation and simple geometrical considerations. Then the combination of (31), (42), and (43) provide the overall reflectance $\mathcal{R}_N$ as function of the apodization factor (Figure 12g).

Appendix **C** – Calculation of $\sigma\big(I\ x,y\ \big)$ for the binarization formula of the DPH

From (8) and (10) and from the definition of variance, the following can be demonstrated:

$$\sigma\big(I\ x,y\ \big)=\sqrt{\frac{\iint[I\ x,y\ -\mu\big(I\ x,y\ \big)]^2dxdy}{\iint dxdy}} \tag{44}$$

$$\propto\sqrt{\frac{\iint\left[\sum_{i=1}^{N}|E_{out}\ x,y,\omega_i\ +E_{in}\ x,y,\omega_i\ |^2-2N\right]^2dxdy}{\iint dxdy}}$$

$$=\sqrt{\frac{\iint\left[\sum_{i=1}^{N}\mathrm{e}^{j(k_{ix}x+k_{iy}y)}\ +\mathrm{e}^{-j(k_{ix}x+k_{iy}y)}\ ^2-2N\right]^2dxdy}{\iint dxdy}}$$

$$=\sqrt{\frac{\iint\left[\sum_{i=1}^{N}|\mathrm{e}^{2j(k_{ix}x+k_{iy}y)}\ +2+\mathrm{e}^{-2j(k_{ix}x+k_{iy}y)}|-2N\right]^2dxdy}{\iint dxdy}}$$

$$=\sqrt{\frac{\iint[\xi^2-4N\xi+4N^2]dxdy}{\iint dxdy}}=\sqrt{\frac{\iint\xi^2dxdy}{\iint dxdy}-4N\frac{\iint\xi dxdy}{\iint dxdy}+4N^2}$$

With

$$\xi=\sum_{i=1}^{N}|\mathrm{e}^{2j(k_{ix}x+k_{iy}y)}\ +2+\mathrm{e}^{-2j(k_{ix}x+k_{iy}y)}|$$

Therefore:

$$\frac{\iint\xi dxdy}{\iint dxdy}=\frac{\sum_{i=1}^{N}\iint|\mathrm{e}^{2j(k_{ix}x+k_{iy}y)}\ +2+\mathrm{e}^{-2j(k_{ix}x+k_{iy}y)}|dxdy}{\iint dxdy}=2N \tag{45}$$

Also:

$$\frac{\iint\xi^2dxdy}{\iint dxdy}=\frac{\iint\left(\sum_{i=1}^{N}|\mathrm{e}^{2j(k_{ix}x+k_{iy}y)}\ +\mathrm{e}^{-2j(k_{ix}x+k_{iy}y)}|+2N\right)^2dxdy}{\iint dxdy}$$

$$=\frac{\iint\begin{bmatrix}\left(\sum_{i=1}^{N}|\mathrm{e}^{2j(k_{ix}x+k_{iy}y)}\ +\mathrm{e}^{-2j(k_{ix}x+k_{iy}y)}|\right)^2+\\4N\sum_{i=1}^{N}|\mathrm{e}^{2j(k_{ix}x+k_{iy}y)}\ +\mathrm{e}^{-2j(k_{ix}x+k_{iy}y)}|+4N^2\end{bmatrix}dxdy}{\iint dxdy}$$

$$=\frac{\iint\left[\left(\sum_{i=1}^{N}|\mathrm{e}^{2j(k_{ix}x+k_{iy}y)}\ +\mathrm{e}^{-2j(k_{ix}x+k_{iy}y)}|\right)^2\right]dxdy}{\iint dxdy}+4N^2$$

$$= \frac{\sum_{i,l=1}^{N} \left(\iint \left[|e^{2j[(k_{ix}+k_{lx})x+(k_{iy}+k_{ly})y]}| + |e^{-2j[(k_{ix}+k_{lx})x+(k_{iy}+k_{ly})y]}| \right] dxdy \right) + \iint \zeta dxdy}{\iint dxdy}$$

$$+ 4N^2$$

Where

$$\iint \zeta dxdy = \iint \sum_{i,l=1}^{N} |e^{2j[(k_{ix}-k_{lx})x+(k_{iy}-k_{ly})y]}| \, dxdy$$
$$= \sum_{i,l=1}^{N} \iint |e^{2j[(k_{ix}-k_{lx})x+(k_{iy}-k_{ly})y]}| dxdy = N \iint dxdy$$

Thus

$$\frac{\iint \xi^2 dxdy}{\iint dxdy} = N + 4N^2 \tag{46}$$

Substituting (AC2) and (AC3) into (AC1) we obtain:

$$\sigma(I\ x, y\ ) = \sqrt{N} \tag{47}$$

Bibliography

1 International Year of Light and light-based technologies 2015. www.light2015.org.

2 Lifante, G. *Integrated Photonics: Fundamentals*. (John Wiley & Sons, 2003).

3 Römer, H. A Short Survey of the History of Optics. *Theoretical Optics: An Introduction*, 1-13.

4 Gerry, C. & Knight, P. *Introductory quantum optics*. (Cambridge university press, 2005).

5 Gordon, J. P., Zeiger, H. J. & Townes, C. H. Maser - New type of Microwave amplfier, frequency standard, and spectrometer. *Physical Review* **99**, 1264-1274, doi:10.1103/PhysRev.99.1264 (1955).

6 Maiman, T. H. Stimulated optical radiation in ruby masers. *Nature* **187**, 493 (1960).

7 Townes, C. H. The first laser. *A Century of Nature: Twenty-One Discoveries that Changed Science and the World. Chicago: University of Chicago Press (107–112)* (2003).

8 Miller, S. E. Integrated optics: an introduction. *Bell System Technical Journal* **48**, 2059-2069 (1969).

9 Schmidt, R. & Kaminow, I. Metal-diffused optical waveguides in LiNbO3. *Applied physics letters* **25**, 458-460 (1974).

10 Powell, M. A. & Donnell, A. O. What integrated optics is really used for. *Optics and Photonics News* **8**, 23-29 (1997).

11 Ye, W. N. & Xiong, Y. Review of silicon photonics: history and recent advances. *Journal of Modern Optics* **60**, 1299-1320 (2013).

12 Soref, R. & Lorenzo, J. Single-crystal silicon: a new material for 1.3 and 1.6 μm integrated-optical components. *Electronics Letters* **21**, 953-954 (1985).

13 Soref, R. A. & Lorenzo, J. P. All-silicon active and passive guided-wave components for lambda= 1.3 and 1.6 microns. *IEEE Journal of Quantum Electronics* **22**, 873-879 (1986).

14 Qian, D. *et al.* in *Frontiers in Optics*. FW6C. 3 (Optical Society of America).

15 Sun, C. *et al.* Single-chip microprocessor that communicates directly using light. *Nature* **528**, 534-538 (2015).

16 Lin, Q. *et al.* Coherent mixing of mechanical excitations in nano-optomechanical structures. *Nature Photonics* **4**, 236-242 (2010).

17 Gil-Santos, E. *et al.* High frequency nano-optomechanical disk resonators in liquids. *arXiv preprint arXiv:1503.03472* (2015).

18 Huang, M. C., Zhou, Y. & Chang-Hasnain, C. J. A surface-emitting laser incorporating a high-index-contrast subwavelength grating. *Nature Photonics* **1**, 119-122 (2007).

19 Chang-Hasnain, C. J. & Yang, W. High-contrast gratings for integrated optoelectronics. *Advances in Optics and Photonics* **4**, 379-440 (2012).

20 Ishizaki, K., Koumura, M., Suzuki, K., Gondaira, K. & Noda, S. Realization of three-dimensional guiding of photons in photonic crystals. *Nature Photonics* **7**, 133-137 (2013).

21 Yablonovitch, E. Inhibited spontaneous emission in solid-state physics and electronics. *Physical Review Letters* **58**, 2059 (1987).

22 Norris, D. J. Photonic Crystals: A view of the future. *Nature materials* **6**, 177-178 (2007).

23 Ellis, B. *et al.* Ultralow-threshold electrically pumped quantum-dot photonic-crystal nanocavity laser. *Nature Photonics* **5**, 297-300 (2011).

24 Meng, X. *et al.* Design, fabrication and optical characterization of photonic crystal assisted thin film monocrystalline-silicon solar cells. *Optics express* **20**, A465-A475 (2012).

25 Estevez, M.-C., Alvarez, M. & Lechuga, L. M. Integrated optical devices for lab-on-a-chip biosensing applications. *Laser & Photonics Reviews* **6**, 463-487 (2012).

26 Threm, D., Nazirizadeh, Y. & Gerken, M. Photonic crystal biosensors towards on-chip integration. *Journal of biophotonics* **5**, 601-616 (2012).

27 Huang, D. *et al.* Optical coherence tomography. *Science* **254**, 1178-1181 (1991).

28 Gu, T., El-Emawy, M. A., Yang, K., Stintz, A. & Lester, L. F. Resistance to edge recombination in GaAs-based dots-in-a-well solar cells. *Applied physics letters* **95**, 261106 (2009).

29 Shirasaki, Y., Supran, G. J., Bawendi, M. G. & Bulović, V. Emergence of colloidal quantum-dot light-emitting technologies. *Nature Photonics* **7**, 13-23 (2013).

30 Liu, G., Stintz, A., Li, H., Malloy, K. & Lester, L. Extremely low room-temperature threshold current density diode lasers using InAs dots in In0. 15Ga0. 85As quantum well. *Electronics Letters* **35**, 1163-1165 (1999).

31 Kim, T.-H. *et al.* Full-colour quantum dot displays fabricated by transfer printing. *Nature Photonics* **5**, 176-182 (2011).

32 Jang, E. *et al.* White-Light-Emitting Diodes with Quantum Dot Color Converters for Display Backlights. *Advanced Materials* **22**, 3076-3080 (2010).

33 Medintz, I. L., Uyeda, H. T., Goldman, E. R. & Mattoussi, H. Quantum dot bioconjugates for imaging, labelling and sensing. *Nature materials* **4**, 435-446 (2005).

34 Santori, C., Fattal, D., Vučković, J., Solomon, G. S. & Yamamoto, Y. Indistinguishable photons from a single-photon device. *Nature* **419**, 594-597 (2002).

35 Buckley, S., Rivoire, K. & Vučković, J. Engineered quantum dot single-photon sources. *Reports on Progress in Physics* **75**, 126503 (2012).

36 Gowen, A., O'Donnell, C., Cullen, P., Downey, G. & Frias, J. Hyperspectral imaging–an emerging process analytical tool for food quality and safety control. *Trends in Food Science & Technology* **18**, 590-598 (2007).

37 Levenson, R. M. & Mansfield, J. R. Multispectral imaging in biology and medicine: slices of life. *Cytometry part A* **69**, 748-758 (2006).

38 Chang, C.-I. *Hyperspectral imaging: techniques for spectral detection and classification*. Vol. 1 (Springer Science & Business Media, 2003).

39 Hackwell, J. A. *et al.* in *SPIE's 1996 International Symposium on Optical Science, Engineering, and Instrumentation.* 102-107 (International Society for Optics and Photonics).

40 Boyd, R. W. *Nonlinear optics*. (Academic press, 2003).

41 Weiner, A. *Ultrafast optics*. Vol. 72 (John Wiley & Sons, 2011).

42 Ye, Q. *et al.* Investigation of diode-pumped, self-frequency doubled RGB lasers from Nd: YCOB crystals. *Optics communications* **164**, 33-37 (1999).

43 Gattass, R. R. & Mazur, E. Femtosecond laser micromachining in transparent materials. *Nature Photonics* **2**, 219-225 (2008).

44 Koenig, K., Krauss, O. & Riemann, I. Intratissue surgery with 80 MHz nanojoule femtosecond laser pulses in the near infrared. *Optics express* **10**, 171-176 (2002).

45 Glezer, E. *et al.* Three-dimensional optical storage inside transparent materials. *Optics letters* **21**, 2023-2025 (1996).

46 Velten, A. *et al.* Recovering three-dimensional shape around a corner using ultrafast time-of-flight imaging. *Nature communications* **3**, 745 (2012).

47 Bimber, O. & Raskar, R. *Spatial augmented reality: merging real and virtual worlds*. (CRC Press, 2005).

48 Furht, B. *Handbook of augmented reality*. (Springer Science & Business Media, 2011).

49 Fattal, D. *et al.* A multi-directional backlight for a wide-angle, glasses-free three-dimensional display. *Nature* **495**, 348-351 (2013).

50 Akeley, K., Watt, S. J., Girshick, A. R. & Banks, M. S. in *ACM transactions on graphics (TOG)*. 804-813 (ACM).

51 Ni, X., Kildishev, A. V. & Shalaev, V. M. Metasurface holograms for visible light. *Nature communications* **4** (2013).

52 Chen, W. T. *et al.* High-efficiency broadband meta-hologram with polarization-controlled dual images. *Nano letters* **14**, 225-230 (2013).

53 Yaraş, F., Kang, H. & Onural, L. Circular holographic video display system. *Optics express* **19**, 9147-9156 (2011).

54 Sun, J., Timurdogan, E., Yaacobi, A., Hosseini, E. S. & Watts, M. R. Large-scale nanophotonic phased array. *Nature* **493**, 195-199 (2013).

55 Schowengerdt, B. T. & Seibel, E. J. True 3-D scanned voxel displays using single or multiple light sources. *Journal of the Society for Information Display* **14**, 135-143 (2006).

56 Azuma, R. *et al.* Recent advances in augmented reality. *Computer Graphics and Applications, IEEE* **21**, 34-47 (2001).

57 Photonics21. Industry Report Photonics 2013. (2013).

58 Goodwin, M. Towards 2020 - Photonics driving economic growth in Europe. *European Technology Platform Photonics21, Brussels* (2013).

59 National Photonics Initiative. www.lightourfuture.org.

60 Office of the Press Secretary, White House Fact Sheet. *https://www.whitehouse.gov/the-press-office/2014/10/03/fact-sheet-president-obama-announces-new-manufacturing-innovation-instit*.

61 Chou, S. Y., Krauss, P. R. & Renstrom, P. J. Imprint of sub-25 nm vias and trenches in polymers. *Applied physics letters* **67**, 3114-3116 (1995).

62 Guo, L. J. Recent progress in nanoimprint technology and its applications. *Journal of Physics D: Applied Physics* **37**, R123 (2004).

63 MIT Technology Review. *10 Emerging Technologies that will change the World* (2003).

64 EV Group Inc. *www.evgroup.com*.

65 Obducat AB. *www.obducat.com*.

66 Nanonex. *www.nanonex.com*.

67 Suss MicroTec. *www.suss.com/en*.

68 Smart Equipment Technology. *www.set-sas.fr*.

69 NIL Technology ApS. *www.nilt.com*.

70 Molecular Imprints Inc. *www.molecularimprints.com*.

71 Nyfeler, A. & Greenaway, D. L. Process for embossing a relief pattern into a thermoplastic information carrier. (1980).

72 Haisma, J., Verheijen, M., Van Den Heuvel, K. & Van Den Berg, J. Mold-assisted nanolithography: A process for reliable pattern replication. *Journal of Vacuum Science & Technology B* **14**, 4124-4128 (1996).

73 Fujimori, S. Fine pattern fabrication by the molded mask method (nanoimprint lithography) in the 1970s. *Japanese Journal of Applied Physics* **48**, 06FH01 (2009).

74 Cedeno, C. C. *et al.* Nanoimprint lithography for organic electronics. *Microelectronic engineering* **61**, 25-31 (2002).

75 Zhang, W. & Chou, S. Y. Fabrication of 60-nm transistors on 4-in. wafer using nanoimprint at all lithography levels. *Applied physics letters* **83**, 1632-1634 (2003).

76 Macintyre, D. *et al.* Nanoimprint lithography process optimization for the fabrication of high electron mobility transistors. *Journal of Vacuum Science & Technology B* **21**, 2783-2787 (2003).

77 Kao, P.-C. *et al.* Fabrication of large-scaled organic light emitting devices on the flexible substrates using low-pressure imprinting lithography. *Electron Devices, IEEE Transactions on* **52**, 1722-1726 (2005).

78 Xia, Q., Yang, J. J., Wu, W., Li, X. & Williams, R. S. Self-aligned memristor cross-point arrays fabricated with one nanoimprint lithography step. *Nano letters* **10**, 2909-2914 (2010).

79 Lee, K. *et al.* in *Magnetics Conference (INTERMAG), 2015 IEEE.* 1-1 (IEEE).

80 Falconnet, D. *et al.* A novel approach to produce protein nanopatterns by combining nanoimprint lithography and molecular self-assembly. *Nano letters* **4**, 1909-1914 (2004).

81 Jeoung, E. *et al.* Fabrication of Robust Protein Films Using Nanoimprint Lithography. *Advanced Materials* **27**, 6251-6255 (2015).

82 Nishikawa, T. & Fujita, S. *Nanoimprint Biosensors: The Fusion of Nanofabrication, Nanophotonics and Nanobiology.* (CRC Press, 2015).

83 Yamanaka, K. & Saito, M. in *Nanobiosensors and Nanobioanalyses* 71-80 (Springer, 2015).

84 Fernandez-Cuesta, I. *et al.* Fabrication of fluidic devices with 30 nm nanochannels by direct imprinting. *Journal of Vacuum Science & Technology B* **29**, 06F801 (2011).

85 Tormen, M. *et al.* Fabrication of three-dimensional stamps for embossing techniques by lithographically controlled isotropic wet etching. *Journal of Vacuum Science & Technology B* **23**, 2920-2924 (2005).

86 Saison, T. *et al.* Replication of butterfly wing and natural lotus leaf structures by nanoimprint on silica sol–gel films. *Bioinspiration & biomimetics* **3**, 046004 (2008).

87 Colburn, M. *et al.* Step and flash imprint lithography: a new approach to high-resolution patterning. *Microlithography'99*, 379-389 (1999).

88 Peroz, C. *et al.* Step and repeat UV nanoimprint lithography on pre-spin coated resist film: a promising route for fabricating nanodevices. *Nanotechnology* **21**, 445301 (2010).

89 Taylor, H. & Boning, D. in *SPIE Advanced Lithography.* 76410U-76410U-76412 (International Society for Optics and Photonics).

90 Huang, X. *et al.* Reversal imprinting by transferring polymer from mold to substrate. *Journal of Vacuum Science & Technology B* **20**, 2872-2876 (2002).

91 Bao, L.-R. *et al.* Nanoimprinting over topography and multilayer three-dimensional printing. *Journal of Vacuum Science & Technology B* **20**, 2881-2886 (2002).

92 Kehagias, N. *et al.* Submicron three-dimensional structures fabricated by reverse contact UV nanoimprint lithographya). *Journal of Vacuum Science & Technology B* **24**, 3002-3005 (2006).

93 Viheriälä, J., Kontio, J., Pessa, M. & Niemi, T. *Nanoimprint lithography-next generation nanopatterning methods for nanophotonics fabrication.* (INTECH Open Access Publisher, 2010).

94 Pina-Hernandez, C. *et al.* A route for fabricating printable photonic devices with sub-10 nm resolution. *Nanotechnology* **24**, 065301 (2013).

95 Ok, J. G. *et al.* Continuous and scalable fabrication of flexible metamaterial films via roll-to-roll nanoimprint process for broadband plasmonic infrared filters. *Applied physics letters* **101**, 223102 (2012).

96 Ge, H., Wu, W. & Li, W.-D. in *Lab-on-Fiber Technology* 91-109 (Springer, 2015).

97 micro resist technology GmbH. *www.microresist.de*.

98 Li, W.-D., Wu, W. & Williams, R. S. Combined helium ion beam and nanoimprint lithography attains 4 nm half-pitch dense patterns. *Journal of Vacuum Science & Technology B* **30**, 06F304 (2012).

99 Peroz, C. *et al.* Single digit nanofabrication by step-and-repeat nanoimprint lithography. *Nanotechnology* **23**, 015305 (2012).

100 Mitsubishi Rayon America Inc. *www.mrany.com*.

101 Dhuey, S., Peroz, C., Olynick, D., Calafiore, G. & Cabrini, S. Obtaining nanoimprint template gratings with 10 nm half-pitch by atomic layer deposition enabled spacer double patterning. *Nanotechnology* **24**, 105303-105303 (2013).

102 Guo, L. J. Nanoimprint lithography: methods and material requirements. *Advanced Materials* **19**, 495-513 (2007).

103 Zhang, L. *et al.* Direct-write three-dimensional nanofabrication of nanopyramids and nanocones on Si by nanotumefaction using a helium ion microscope. *Nanotechnology* **26**, 255303 (2015).

104 Watanabe, K. *et al.* Nanoimprint using three-dimensional microlens mold made by focused-ion-beam chemical vapor deposition. *Journal of Vacuum Science & Technology B* **22**, 22-26 (2004).

105 Albrecht, T. *et al.* Bit Patterned Magnetic Recording: Theory, Media Fabrication, and Recording Performance. (2015).

106 Sun, Z. *et al.* Directed Self-Assembly of Poly (2-vinylpyridine)-b-polystyrene-b-poly (2-vinylpyridine) Triblock Copolymer with Sub-15 nm Spacing Line Patterns Using a Nanoimprinted Photoresist Template. *Advanced Materials* **27**, 4364-4370 (2015).

107 Beck, M. *et al.* Improving stamps for 10 nm level wafer scale nanoimprint lithography. *Microelectronic engineering* **61**, 441-448 (2002).

108 Vogler, M. *et al.* Development of a novel, low-viscosity UV-curable polymer system for UV-nanoimprint lithography. *Microelectronic engineering* **84**, 984-988 (2007).

109 Liang, X., Tan, H., Fu, Z. & Chou, S. Y. Air bubble formation and dissolution in dispensing nanoimprint lithography. *Nanotechnology* **18**, 025303 (2007).

110 Kim, K.-D., Kwon, H.-J., Choi, D.-g., Jeong, J.-H. & Lee, E.-s. Resist flow behavior in ultraviolet nanoimprint lithography as a function of contact angle with stamp and substrate. *Japanese Journal of Applied Physics* **47**, 8648 (2008).

111 Teisseire, J., Revaux, A., Foresti, M. & Barthel, E. Confinement and flow dynamics in thin polymer films for nanoimprint lithography. *Applied physics letters* **98**, 013106 (2011).

112 Hocheng, H. & Nien, C. Numerical analysis of effects of mold features and contact friction on cavity filling in the nanoimprinting process. *Journal of Micro/Nanolithography, MEMS, and MOEMS* **5**, 011004-011007 (2006).

113 Hirai, Y., Konishi, T., Yoshikawa, T. & Yoshida, S. Simulation and experimental study of polymer deformation in nanoimprint lithography. *Journal of Vacuum Science & Technology B* **22**, 3288-3293 (2004).

114 Jeong, J.-H. *et al.* Flow behavior at the embossing stage of nanoimprint lithography. *Fibers and Polymers* **3**, 113-119 (2002).

115 Taylor, H., Lam, Y. C. & Boning, D. A computationally simple method for simulating the micro-embossing of thermoplastic layers. *Journal of Micromechanics and Microengineering* **19**, 075007 (2009).

116 Suh, K. Y., Kim, P. & Lee, H. H. Capillary kinetics of thin polymer films in permeable microcavities. *Applied physics letters* **85**, 4019-4021 (2004).

117 Yoon, H. *et al.* Capillary force lithography with impermeable molds. *Applied physics letters* **88**, 254104 (2006).

118 International Technology Roadmap for Semiconductor, (ITRS). www.itrs2.net.

119 Moore, G. E. in *SPIE's 1995 Symposium on Microlithography.* 2-17 (International Society for Optics and Photonics).

120 Schaller, R. R. Moore's law: past, present and future. *Spectrum, IEEE* **34**, 52-59 (1997).

121 Hua, F. *et al.* Polymer imprint lithography with molecular-scale resolution. *Nano letters* **4**, 2467-2471 (2004).

122 Austin, M. D. *et al.* 6 nm half-pitch lines and 0.04 μm2 static random access memory patterns by nanoimprint lithography. *Nanotechnology* **16**, 1058 (2005).

123 Calafiore, G. *et al.* Multilayer lift-off process for sub-15-nm patterning by step-and-repeat ultraviolet nanoimprint lithography. *Journal of Micro/Nanolithography, MEMS, and MOEMS* **13**, 033013-033013 (2014).

124 Takeishi, H. & Sreenivasan, S. Nanoimprint system development and status for high volume semiconductor manufacturing. *SPIE Advanced Lithography*, 94230C-94239 (2015).

125 Malloy, M. & Litt, L. C. Technology review and assessment of nanoimprint lithography for semiconductor and patterned media manufacturing. *Journal of Micro/Nanolithography, MEMS, and MOEMS* **10**, 032001-032001-032013 (2011).

126 Khusnatdinov, N. *et al.* High-throughput jet and flash imprint lithography for advanced semiconductor memory. *SPIE Advanced Lithography*, 904910-904917 (2014).

127 Iwaga, T. Oral Presentation: Nanoimprint System Development and Status for High Volume Semiconductor Manufacturing. *Nanoimprint & Nanoprint Technology Conference (www.nntconf.org)* (2015).

128 Ye, Z. *et al.* Defect reduction for semiconductor memory applications using jet and flash imprint lithography. *SPIE Advanced Lithography*, 86800C-86807 (2013).

129 Ye, Z. *et al.* Imprint process performance for patterned media at densities greater than 1Tb/in2. *SPIE Advanced Lithography*, 83230V-83236 (2012).

130 Higashiki, T., Nakasugi, T. & Yoneda, I. Nanoimprint lithography for semiconductor devices and future patterning innovation. *SPIE Advanced Lithography*, 797003-797006 (2011).

131 Yang, X. *et al.* Fabrication of servo-integrated template for 1.5 Teradot/inch2 bit patterned media with block copolymer directed assembly. *Journal of Micro/Nanolithography, MEMS, and MOEMS* **13**, 031307 (2014).

132 Singh, L. *et al.* Defect reduction of high-density full-field patterns in jet and flash imprint lithography. *Journal of Micro/Nanolithography, MEMS, and MOEMS* **10**, 033018-033016 (2011).

133 Xia, Q. & Pease, R. F. Nanoimprint lithography 20 years on. *Nanotechnology* **26**, 182501 (2015).

134 Suh, K. Y. & Lee, H. H. Capillary force lithography: large-area patterning, self-organization, and anisotropic dewetting. *Advanced Functional Materials* **12**, 405-413 (2002).

135 Hermes Microvision Inc. Ebeam inspection tools, eXplore Series. *www.hermes-microvision.com/Products/eX.php*.

136 Baets, R., Vanholme, L. & Smit, M. in *International symposium OPTRO 2005*. 33-34.

137 Paniccia, M., Morse, M. & Salib, M. in *Silicon Photonics* 51-88 (Springer, 2004).

138 Song, J., Wang, L., He, S. & He, J.-J. Effect of volume defects on the performance of planar waveguide devices. *Photonics Technology Letters, IEEE* **17**, 2322-2324 (2005).

139 Yao, Y. *et al.* Nanoimprint lithography: an enabling technology for nanophotonics. *Applied Physics A* **121**, 327-333 (2015).

140 Lova, P. & Soci, C. in *Organic and Hybrid Photonic Crystals* 187-212 (Springer, 2015).

141 Yao, Y., Liu, H. & Wu, W. Spectrum splitting using multi-layer dielectric meta-surfaces for efficient solar energy harvesting. *Applied Physics A* **115**, 713-719 (2014).

142 Yao, Y., Liu, H. & Wu, W. Fabrication of high-contrast gratings for a parallel spectrum splitting dispersive element in a concentrated photovoltaic system. *Journal of Vacuum Science & Technology B* **32**, 06FG04 (2014).

143 Kim, J. S. *et al.* Poly (3-hexylthiophene) nanorods with aligned chain orientation for organic photovoltaics. *Advanced Functional Materials* **20**, 540-545 (2010).

144 Tan, H., Gilbertson, A. & Chou, S. Y. Roller nanoimprint lithography. *Journal of Vacuum Science & Technology B* **16**, 3926-3928 (1998).

145 Facility for Advanced Roll-to-Roll Manufactoring for the Life and Nano Sciences. *www.umass.edu/cphm/facilities/advanced-print-and-roll-roll-manufacturing-facility*.

146 Zhou, L. *et al.* Light manipulation for organic optoelectronics using bio-inspired moth's eye nanostructures. *Scientific reports* **4** (2014).

147 Rogers, J. A., Meier, M. & Dodabalapur, A. Using printing and molding techniques to produce distributed feedback and Bragg reflector resonators for plastic lasers. *Applied physics letters* **73**, 1766-1768 (1998).

148 Reboud, V. *et al.* Two-dimensional polymer photonic crystal band-edge lasers fabricated by nanoimprint lithography. *Applied physics letters* **91**, 151101 (2007).

149 Plachetka, U. *et al.* Fabrication of photonic components by nanoimprint technology within ePIXnet. *Microelectronic engineering* **85**, 886-889 (2008).

150 Peroz, C. *et al.* Digital spectrometer-on-chip fabricated by step and repeat nanoimprint lithography on pre-spin coated films. *Microelectronic engineering* **88**, 2092-2095 (2011).

151 Chao, C.-y. & Guo, L. J. Polymer microring resonators fabricated by nanoimprint technique. *Journal of Vacuum Science & Technology B* **20**, 2862-2866 (2002).

152 Han, T., Madden, S., Bulla, D. & Luther-Davies, B. Low loss Chalcogenide glass waveguides by thermal nano-imprint lithography. *Optics express* **18**, 19286-19291 (2010).

153 Ahn, S.-W., Lee, K.-D., Kim, D.-H. & Lee, S.-S. Polymeric wavelength filter based on a Bragg grating using nanoimprint technique. *Photonics Technology Letters, IEEE* **17**, 2122-2124 (2005).

154 Wu, W. *et al.* Optical metamaterials at near and mid-IR range fabricated by nanoimprint lithography. *Applied Physics A* **87**, 143-150 (2007).

155 Kontio, J. M., Simonen, J., Tommila, J. & Pessa, M. Arrays of metallic nanocones fabricated by UV-nanoimprint lithography. *Microelectronic engineering* **87**, 1711-1715 (2010).

156 Malyarchuk, V. *et al.* High performance plasmonic crystal sensor formed by soft nanoimprint lithography. *Optics express* **13**, 5669-5675 (2005).

157 Krishnamoorthy, S., Krishnan, S., Thoniyot, P. & Low, H. Y. Inherently reproducible fabrication of plasmonic nanoparticle arrays for SERS by combining nanoimprint and copolymer lithography. *ACS applied materials & interfaces* **3**, 1033-1040 (2011).

158 Fernandez-Cuesta, I. *et al.* V-groove plasmonic waveguides fabricated by nanoimprint lithography. *Journal of Vacuum Science & Technology B* **25**, 2649-2653 (2007).

159 Zhang, W. *et al.* Giant and uniform fluorescence enhancement over large areas using plasmonic nanodots in 3D resonant cavity nanoantenna by nanoimprinting. *Nanotechnology* **23**, 225301 (2012).

160 Verschuuren, M. A. Substrate conformal imprint lithography for nanophotonics. (2010).

161 Boltasseva, A. Plasmonic components fabrication via nanoimprint. *Journal of Optics A: Pure and Applied Optics* **11**, 114001 (2009).

162 Lucas, B. D., Kim, J.-S., Chin, C. & Guo, L. J. Nanoimprint lithography based approach for the fabrication of large-area, uniformly-oriented plasmonic arrays. (2008).

163 Cattoni, A. *et al.* λ3/1000 plasmonic nanocavities for biosensing fabricated by soft UV nanoimprint lithography. *Nano letters* **11**, 3557-3563 (2011).

164 Lee, S.-W. *et al.* Highly sensitive biosensing using arrays of plasmonic Au nanodisks realized by nanoimprint lithography. *ACS nano* **5**, 897-904 (2011).

165 Stewart, M. E. *et al.* Quantitative multispectral biosensing and 1D imaging using quasi-3D plasmonic crystals. *Proceedings of the National Academy of Sciences* **103**, 17143-17148 (2006).

166 Scheerlinck, S., Taillaert, D., Van Thourhout, D. & Baets, R. Flexible metal grating based optical fiber probe for photonic integrated circuits. *Applied physics letters* **92**, 031104 (2008).

167 Kostovski, G., Chinnasamy, U., Jayawardhana, S., Stoddart, P. R. & Mitchell, A. Sub-15nm Optical Fiber Nanoimprint Lithography: A Parallel, Self-aligned and Portable Approach. *Advanced Materials* **23**, 531-535 (2011).

168 SPIE Optics.org, Press Release, EV Group targets photonics with nanoimprint tool. *www.optics.org/news/6/7/6*.

169 Eibelhuber, M., Glinsner, T., Uhrmann, T. & Lindner, P. Nanoimprint Lithography Enables Cost-Effective Photonics Production. *PHOTONICS SPECTRA* **49**, 34-37 (2015).

170 SBIR-STTR, America's Seed Fund, Precise fabrication of integrated photonic and optoelectronic systems using low-cost nanoimprint process. *www.sbir.gov/sbirsearch/detail/664663*.

171 Savage, N. Spectrometers. *Nature Photonics* **3**, 601-602 (2009).

172 Hu, Z. *et al.* Integrated microspectrometer for fluorescence based analysis in a microfluidic format. *Lab on a Chip* **12**, 2850-2857 (2012).

173 Schmidt, O., Bassler, M., Kiesel, P., Knollenberg, C. & Johnson, N. Fluorescence spectrometer-on-a-fluidic-chip. *Lab on a Chip* **7**, 626-629 (2007).

174 Gallegos, D. *et al.* Label-free biodetection using a smartphone. *Lab on a Chip* **13**, 2124-2132 (2013).

175 Song, W., Liu, A., Lim, C. & Yap, P. in *Optical MEMS and Nanophotonics, 2007 IEEE/LEOS International Conference on.* 161-162 (IEEE).

176 Wolffenbuttel, R. F. State-of-the-art in integrated optical microspectrometers. *Instrumentation and Measurement, IEEE Transactions on* **53**, 197-202 (2004).

177 Redding, B., Liew, S. F., Sarma, R. & Cao, H. Compact spectrometer based on a disordered photonic chip. *Nature Photonics* **7**, 746-751 (2013).

178 Jovanov, V., Ivanchev, J. & Knipp, D. Standing wave spectrometer. *Optics express* **18**, 426-438 (2010).

179 Avrutsky, I., Chaganti, K., Salakhutdinov, I. & Auner, G. Concept of a miniature optical spectrometer using integrated optical and micro-optical components. *Applied optics* **45**, 7811-7817 (2006).

180 Nitkowski, A., Chen, L. & Lipson, M. Cavity-enhanced on-chip absorption spectroscopy using microring resonators. *Optics express* **16**, 11930-11936 (2008).

181 Sweeney, S. J., Zhang, Y. & Goodyer, I. D. in *SPIE OPTO.* 82640O-82640O-82613 (International Society for Optics and Photonics).

182 Xia, Z. *et al.* High resolution on-chip spectroscopy based on miniaturized microdonut resonators. *Optics express* **19**, 12356-12364 (2011).

183 Velasco, A. V. *et al.* High-resolution Fourier-transform spectrometer chip with microphotonic silicon spiral waveguides. *Optics letters* **38**, 706-708 (2013).

184 Florjanczyk, M. *et al.* Multiaperture planar waveguide spectrometer formed by arrayed Mach-Zehnder interferometers. *Optics express* **15**, 18176-18189 (2007).

185 Cheben, P. *et al.* A high-resolution silicon-on-insulator arrayed waveguide grating microspectrometer with sub-micrometer aperture waveguides. *Optics express* **15**, 2299-2306 (2007).

186 Barbarin, Y. *et al.* in *Integrated Photonics Research.* IThG4 (Optical Society of America).

187 Kyotoku, B. B., Chen, L. & Lipson, M. Sub-nm resolution cavity enhanced microspectrometer. *Optics express* **18**, 102-107 (2010).

188 Keliher, P. N. & Wohlers, C. C. Echelle grating spectrometers in analytical spectrometry. *Analytical Chemistry* **48**, 333A-340a (1976).

189 Ma, X., Li, M. & He, J.-J. CMOS-Compatible Integrated Spectrometer Based on Echelle Diffraction Grating and MSM Photodetector Array. *Photonics Journal, IEEE* **5**, 6600807-6600807 (2013).

190 Xu, Z. *et al.* Multimodal multiplex spectroscopy using photonic crystals. *Optics express* **11**, 2126-2133 (2003).

191 Pervez, N. K. *et al.* Photonic crystal spectrometer. *Optics express* **18**, 8277-8285 (2010).

192 Khalil, D., Omran, H., Medhat, M. & Saadany, B. in *MOEMS-MEMS.* 75940T-75940T-75913 (International Society for Optics and Photonics).

193 Correia, J., Bartek, M. & Wolffenbuttel, R. Bulk-micromachined tunable Fabry–Perot microinterferometer for the visible spectral range. *Sensors and Actuators A: Physical* **76**, 191-196 (1999).

194 Hariharan, P. *Optical Holography: Principles, techniques and applications*. (Cambridge University Press, 1996).

195 Peroz, C. *et al.* High-resolution spectrometer-on-chip based on digital planar holography. *Photonics Journal, IEEE* **3**, 888-896 (2011).

196 Yankov, V. *et al.* Multiwavelength Bragg gratings and their application to optical MUX/DEMUX devices. *Photonics Technology Letters, IEEE* **15**, 410-412 (2003).

197 Peroz, C. *et al.* Multiband wavelength demultiplexer based on digital planar holography for on-chip spectroscopy applications. *Optics letters* **37**, 695-697 (2012).

198 Calò, C. *et al.* Fabrication of digital planar holograms into high refractive index waveguide core for spectroscopy-on-chip applications. *Journal of Vacuum Science & Technology B: Microelectronics and Nanometer Structures* **30**, 06FE01-06FE01-04 (2012).

199 Babin, S. *et al.* Fabrication of novel digital optical spectrometer on chip. *Journal of Vacuum Science & Technology B: Microelectronics and Nanometer Structures* **27**, 3187-3191 (2009).

200 Babin, S. *et al.* Digital optical spectrometer-on-chip. *Applied physics letters* **95**, 041105 (2009).

201 Sheppard, C. Approximate calculation of the reflection coefficient from a stratified medium. *Pure and Applied Optics: Journal of the European Optical Society Part A* **4**, 665 (1995).

202 Born, M. (Pergamon Press, London).

203 Saleh, B. E., Teich, M. C. & Saleh, B. E. *Fundamentals of photonics*. Vol. 22 (Wiley New York, 1991).

204 Gabor, D. A new microscopic principle. *Nature* **161**, 777-778 (1948).

205 Leith, E. N. & Upatnieks, J. Wavefront reconstruction with diffused illumination and three-dimensional objects. *Josa* **54**, 1295-1301 (1964).

206 Nano-optic Devices. *www.nanoopticdevices.com*.

207 MATLAB. *www.mathworks.com/products/matlab*.

208 Lumerical Solutions, Inc. *www.lumerical.com*.

209 Marcatili, E. A. Dielectric rectangular waveguide and directional coupler for integrated optics. *Bell System Technical Journal* **48**, 2071-2102 (1969).

210 Calafiore, G. *et al.* Holographic planar lightwave circuit for on-chip spectroscopy. *Light: Science & Applications* **3**, e203 (2014).

211 LionixBV. *www.lionixbv.com*.

212 Somekh, S., Garmire, E., Yariv, A., Garvin, H. & Hunsperger, R. Channel optical waveguide directional couplers. *Applied physics letters* **22**, 46-47 (1973).

213 Calafiore, G. *et al.* Step-and-repeat nanoimprint on pre-spin coated film for the fabrication of integrated optical devices. *Journal of Micro/Nanolithography, MEMS, and MOEMS* **14**, 033506-033506 (2015).

214 Chen, L., Deng, X., Wang, J., Takahashi, K. & Liu, F. Defect control in nanoimprint lithography. *Journal of Vacuum Science & Technology B* **23**, 2933-2938 (2005).

215 Ryu, J., Lee, S.-H., Lim, H., Park, H.-H. & Lee, J. Study of air bubble generation and its minimization during dispensing based ultraviolet nanoimprint lithography (UV-NIL). *Microelectronic engineering* **123**, 131-135 (2014).

216 Chandross, M. & Grest, G. S. Molecular scale modeling of polymer imprint nanolithography. *Langmuir* **28**, 1049-1055 (2011).

217 Pina-Hernandez, C., Guo, L. J. & Fu, P.-F. High-resolution functional epoxysilsesquioxane-based patterning layers for large-area nanoimprinting. *ACS nano* **4**, 4776-4784 (2010).

218 Arkles, B. Hydrophobicity, Hydrophilicity and Silanes. *Paint & Coatings Industry,* *Available:* http://www.gelest.com/goods/pdf/Library/advances/HydrophobicityHydrophilicityandSilanes.pdf (2006).

219 Avantes. www.avantes.com/products/spectrometers.

220 Brinker, C. J. & Scherer, G. W. *Sol-gel science: the physics and chemistry of sol-gel processing.* (Academic press, 2013).

221 Hampton, M. J. *et al.* The patterning of sub-500 nm inorganic oxide structures. *Advanced Materials* **20**, 2667-2673 (2008).

222 Richmond, D. A., Zhang, Q., Cao, G. & Weiss, D. N. Pressureless nanoimprinting of anatase TiO2 precursor films. *Journal of Vacuum Science & Technology B* **29**, 021603 (2011).

223 Yoon, K.-m., Yang, K.-Y., Lee, H. & Kim, H.-S. Formation of TiO2 nanopattern using reverse imprinting and sol-gel method. *Journal of Vacuum Science & Technology B* **27**, 2810-2813 (2009).

224 Yoon, K.-m., Yang, K.-y. & Lee, H. Fabrication of polycrystalline TiO 2 nanopatterns by TiO 2 sol base imprint lithography. *Thin Solid Films* **518**, 126-129 (2009).

225 Li, M., Tan, H., Chen, L., Wang, J. & Chou, S. Y. Large area direct nanoimprinting of SiO2–TiO2 gel gratings for optical applications. *Journal of Vacuum Science & Technology B* **21**, 660-663 (2003).

226 Williams, S. S. *et al.* Nanostructured titania– polymer photovoltaic devices made using PFPE-based nanomolding techniques. *Chemistry of Materials* **20**, 5229-5234 (2008).

227 Luo, X., Zha, C. & Luther-Davies, B. Anhydrous sol-gel synthesis of titania-doped siloxane polymer for integrated optics. *Journal of sol-gel science and technology* **32**, 297-301 (2004).

228 Del Monte, F., Cheben, P., Grover, C. & Mackenzie, J. Preparation and optical characterization of thick-film zirconia and titania ormosils. *Journal of sol-gel science and technology* **15**, 73-85 (1999).

229 Matsuura, Y., Miura, S., Naito, H., Inoue, H. & Matsukawa, K. Nanostructured polysilane–titania hybrids and their application to porous titania thin films. *Journal of organometallic chemistry* **685**, 230-234 (2003).

230 Park, H.-H. *et al.* Photo-induced hybrid nanopatterning of titanium dioxide via direct imprint lithography. *Journal of Materials Chemistry* **20**, 1921-1926 (2010).

231 Park, H.-H. *et al.* Facile nanopatterning of zirconium dioxide films via direct ultraviolet-assisted nanoimprint lithography. *Journal of Materials Chemistry* **21**, 657-662 (2011).

232 Cabrini, S., Peroz, C. & Pina-Hernandez, C. A. Polymerized metal-organic material for printable photonic devices. (2014).

233 Ganesan, R. *et al.* Direct patterning of TiO2 using step-and-flash imprint lithography. *ACS nano* **6**, 1494-1502 (2012).

234 Pina-Hernandez, C. *et al.* Printable planar lightwave circuits with a high refractive index. *Nanotechnology* **25**, 325302 (2014).

235 Lee, C. W., Darmawan, S., Lee, S. Y. & Chin, M. K. in *Integrated Photonics Research and Applications.* IMG2 (Optical Society of America).

236 Bradley, J. D. *et al.* Submicrometer-wide amorphous and polycrystalline anatase TiO 2 waveguides for microphotonic devices. *Optics express* **20**, 23821-23831 (2012).

237 Vukusic, P. & Sambles, J. R. Photonic structures in biology. *Nature* **424**, 852-855 (2003).

238 Joannopoulos, J. D., Johnson, S. G., Winn, J. N. & Meade, R. D. *Photonic crystals: molding the flow of light.* (Princeton university press, 2011).

239 Inoue, K. & Ohtaka, K. *Photonic crystals: physics, fabrication and applications*. Vol. 94 (Springer, 2013).

240 Yasumoto, K. *Electromagnetic theory and applications for photonic crystals*. (CRC press, 2005).

241 Reboud, V. *et al.* Lasing in nanoimprinted two-dimensional photonic crystal band-edge lasers. *Applied physics letters* **102**, 073101 (2013).

242 McGroddy, K. *et al.* Directional emission control and increased light extraction in GaN photonic crystal light emitting diodes. *Applied physics letters* **93**, 103502 (2008).

243 Tokushima, M., Kosaka, H., Tomita, A. & Yamada, H. Lightwave propagation through a 120 sharply bent single-line-defect photonic crystal waveguide. *Applied physics letters* **76**, 952-954 (2000).

244 Russell, P. Photonic crystal fibers. *science* **299**, 358-362 (2003).

245 Petrov, A. Y. & Eich, M. Zero dispersion at small group velocities in photonic crystal waveguides. *Applied physics letters* **85**, 4866-4868 (2004).

246 Nozaki, K. *et al.* Sub-femtojoule all-optical switching using a photonic-crystal nanocavity. *Nature Photonics* **4**, 477-483 (2010).

247 Lin, S., Chow, E., Bur, J., Johnson, S. & Joannopoulos, J. Low-loss, wide-angle Y splitter at~ 1.6-µm wavelengths built with a two-dimensional photonic crystal. *Optics letters* **27**, 1400-1402 (2002).

248 Martinez, A., Cuesta, F. & Marti, J. Ultrashort 2-D photonic crystal directional couplers. *Photonics Technology Letters, IEEE* **15**, 694-696 (2003).

249 Koshiba, M. Wavelength division multiplexing and demultiplexing with photonic crystal waveguide couplers. *Journal of Lightwave Technology* **19**, 1970 (2001).

250 Alivisatos, P. The use of nanocrystals in biological detection. *Nature biotechnology* **22**, 47-52 (2004).

251 Fan, X. & White, I. M. Optofluidic microsystems for chemical and biological analysis. *Nature Photonics* **5**, 591-597 (2011).

252 Lee, K. & Asher, S. A. Photonic crystal chemical sensors: pH and ionic strength. *Journal of the American Chemical Society* **122**, 9534-9537 (2000).

253 Asher, S. A. *et al.* Photonic crystal carbohydrate sensors: low ionic strength sugar sensing. *Journal of the American Chemical Society* **125**, 3322-3329 (2003).

254 Cunin, F. *et al.* Biomolecular screening with encoded porous-silicon photonic crystals. *Nature materials* **1**, 39-41 (2002).

255 Campbell, M., Sharp, D., Harrison, M., Denning, R. & Turberfield, A. Fabrication of photonic crystals for the visible spectrum by holographic lithography. *Nature* **404**, 53-56 (2000).

256 Calafiore, G. *et al.* Printable photonic crystals with high refractive index for applications in visible light. *Nanotechnology* **27**, 115303 (2016).

257 Wijnhoven, J. E., Bechger, L. & Vos, W. L. Fabrication and characterization of large macroporous photonic crystals in titania. *Chemistry of Materials* **13**, 4486-4499 (2001).

258 Kuai, S., Hu, X. & Truong, V.-V. Synthesis of thin film titania photonic crystals through a dip-infiltrating sol–gel process. *Journal of crystal growth* **259**, 404-410 (2003).

259 *aBeam Technologies, Inc.* (www.abeamtech.com).

260 Polyakov, A. *et al.* Coupling model for an extended-range plasmonic optical transformer scanning probe. *Light: Science & Applications* **3**, e195 (2014).

261 Bao, W. *et al.* Mapping local charge recombination heterogeneity by multidimensional nanospectroscopic imaging. *science* **338**, 1317-1321 (2012).

262 Bao, W. *et al.* Visualizing nanoscale excitonic relaxation properties of disordered edges and grain boundaries in monolayer molybdenum disulfide. *Nature communications* **6** (2015).

263 Pina-Hernandez, C. *et al.* in *MNE 2015.*

264 Johannsen, E., Chung, J., Chang, C. & Franses, E. Lipid transport to air/water interfaces. *Colloids and surfaces* **53**, 117-134 (1991).

265 Chang, C.-H. & Franses, E. I. Adsorption dynamics of surfactants at the air/water interface: a critical review of mathematical models, data, and mechanisms. *Colloids and Surfaces A: Physicochemical and Engineering Aspects* **100**, 1-45 (1995).